DEVELOPMENT AND APPLICATION OF
PHTOACOUSTIC/ULTRASOUND MICROSCOPY SYSTEMS

A Dissertation
Presented to
The Academic Faculty

by

Ning Wu

In Partial Fulfillment
of the Requirements for the Degree
Doctor of Philosophy in the
Wallance H. Coulter
Department of Biomedical Engineering

Georgia Institute of Technology
Emory University
Peking University
August, 2017

DEVELOPMENT AND APPLICATION OF
PHTOACOUSTIC/ULTRASOUND MICROSCOPY SYSTEMS

Approved by:

Dr. Changhui Li, Advisor
Department of Biomedical Engineering
Peking University

Dr. Antony K. Chen
Department of Biomedical Engineering
Peking University

Dr. Cheng Zhu, Co-advisor
Department of Biomedical Engineering
Georgia Institute of Technology

Dr. Kun Yang
College of Quality and Technical
Supervision
Hebei University

Dr. Peng Xi
Department of Biomedical Engineering
Peking University

Date Approved: June 7, 2017

ACKNOWLEDGEMENTS

Five years of PhD. study means a lot to me, which combines the excitement, pleasure, surprise and tears. Without the company and help of teachers and friends, I couldn't travel down this road to the point I stand now.

First and foremost, I would like to thank my advisor Dr. Changhui Li in Peking University. I still remember the first E-mail he wrote to me, which is full of encouragement. He is really a nice advisor, with the properties of profound knowledge, patience, responsibility and kindness. I'm lucky and grateful to be one of his students.

I would like to thank my co-advisor Dr. Cheng Zhu in Georgia Institute of Technology. Letting me to choose the project by self-will and giving enough support and guidance to get through the bottleneck, his student-cultured style is what I like and admire most. Also I would like to thank Dr. Robert M. Dickson, who gives me a lot of trust and guidance on the experiments.

Parents are the reason I strive for. I want to thank them for always providing biggest support and getting on my back for every decision I made. I love my parents and will always love them in the future.

Besides, I wish to thank the lab mates in PKU and GT. Thank Shouqi Ye, Guohe Wang, Yicheng Ding, Zijian Deng, Honghong Zhao, Chenghao Ge, Kaitao Li, Aida Demissie, Cheng-Yen Cheng and others, who teach me a lot and lead me into a new research field.

Last but not least, I want to thank my boyfriend Mingze Xu and my friends, Suying Li, Yueying Kao, Bin Zhao, Lei Zhou, Kun Zhou, Zhaoheng Xie and others. They bring me happy and teach me how to enjoy life. We are and always be a family.

TABLE OF CONTENTS

LIST OF TABLES

LIST OF FIGURES

part. ND, neutral-density. L1, collimated lens. L2, focusing lens. GS, glass slide. P, plastic membrane. WT, water tank.

xi

LIST OF SYMBOLS AND ABBREVIATIONS

PA	photoacoustic
PAM	photoacoustic microscopy
US	ultrasound
MEMS	water-immersible microelectromechanical systems
SO_2	oxygen saturation
FCS	fluorescence correlation spectroscopy
OCT	optical coherence tomography
CLSM	confocal laser scanning microscopy
FOV	field of view
STED	stimulated emission depletion microscopy
STORM	stochastic optical reconstruction microscopy
PALM	photoactivated localization microscopy
EM	electromagnetic
AR-PAM	acoustic-resolution PAM
OR-PAM	optical-resolution PAM
NA	numeric aperture
SCO	carboxyhemoglobin saturation
ICG	indocyanine green
GNRs	gold nanorods
MRI	magnetic resonance imaging
TP	two-photon
TPM	TP fluorescence microscopy

SHG	second harmonic generation
SHGM	SHG microscopy
SMF	signal mode fiber
GCF	gold coated film
GL	GRIN lens
PR	parabolic reflector
PM	parabolic mirror
SNR	signal to noise ratio
FWHM	full width at half maximum
MEMS-PR	MEMS with a transparent parabolic reflector
MEMS-PM	MEMS with a parabolic mirror
PMMA	polymethyl methacrylate
MC	motion controller
AC	acquisition card

SUMMARY

Development of biomedical microscopy largely promotes the research of life science and medicine. Emerging as a hybrid imaging technique, Photoacoustic (PA) microscopy (PAM) transfers the absorbed light energy by intrinsic chromophores into heat, and induces ultrasonic signal. PAM combines the merits of optical high contrast and ultrasonic low scattering, which has been a new important modality of biomedical optics microscopy, as well as shows significance for clinical research. Using transducer to detect the ultrasound, PAM has the potential to do ultrasound (US) imaging. Integrated the PA/US dual-modality microscopy can provide complementary information of pure optics imaging and US imaging.

Focusing on high resolution PA/US dual-modality imaging technique, this thesis has done a lot of work including theoretical analysis, simulation, system setup, phantom and small animal experiments. The major work and innovation include:

1. Developing a novel high resolution PA/US dual-modality microscopy, and realizing noninvasively *in vivo* small animal whole eye dual-modality imaging at the first time. The system developed in this thesis is capable to image microcirculatory system of living tissue, as well as provide US structure information.

2. Proposing a new design to use parabolic mirror in PA/US dual-modality microscopy, achieving the confocal effect of collimated light and parallel US. With parabolic mirror, the focusing length of laser and US is decreased largely, which improves the system resolution by the simple design. Combined with water-immersible

microelectromechanical systems (MEMS) scanning mirror, this system can achieve a fast scanning speed.

3. Investigating the effect of transducer deflection angle on functional PAM accuracy, in off-axial PAM systems. With multiple wavelengths, PAM has the advantage to provide functional information, such as oxygen saturation (SO_2). This thesis demonstrates that the oblique detection will lead to the inaccuracy of SO_2 measurement severely, providing valuable guidance for the design of functional PAM.

4. Besides, this thesis introduces other two parts of work. One is continuing the PAM study. We explore the feasibility of a new PA contrast agent- DNA-templated silver nanocluster, and compare its PA signal with other organic dyes. In another work, we investigate the 2D kinetics by fluorescence correlation spectroscopy (FCS), demonstrating FCS is a potential method to study molecular mechanism of immunology pathway.

This thesis mainly contains five parts: Introduction part gives a brief idea about PAM background; The second and third chapter introduce the development and application of PA/US dual-modality microscopies; The forth chapter investigates the effect of oblique detection angle on functional PAM quantitative measurement; The fifth chapter introduces the study on new PA imaging contrast agent and molecular 2D kinetics by FCS; The last chapter gives the conclusion of whole thesis.

CHAPTER 1.   INTRODUCTION

Owing to its superior sensitivity, specificity, and non-ionizing characteristics, optical microscopy plays an essential role in biomedicine. In addition, integrating optical contrast with other complementary information can form valuable multi-modality imaging. This chapter first introduces biomedical pure optical microscopy in Section 1.1, and photoacoustic (PA) microscopy (PAM) in Section 1.2, Section 1.3 and 1.4 introduce the multimodality PAM systems and the motivation for developing high-resolution PAM/US systems. It demonstrates that development of multimodality PA system can provide promising contributions to clinical research. Section 1.5 is the chapter conclusion.

1.1   Biomedical Optical Microscopy

"Seeing is believing." The invention of optical microscopy opens the possibility to investigate the microcosms beyond the limitation of human eyes. The past decades have witnessed application of optical microscopy in wide variety of fields, like cell biology, neurobiology, toxicology, physiology, genetics, and pathology[1]. Confocal laser scanning microscopy (CLSM), super-resolution microscopy, and optical coherence tomography (OCT) have been emerged as some of the representative techniques among biomedical optical microscopies.
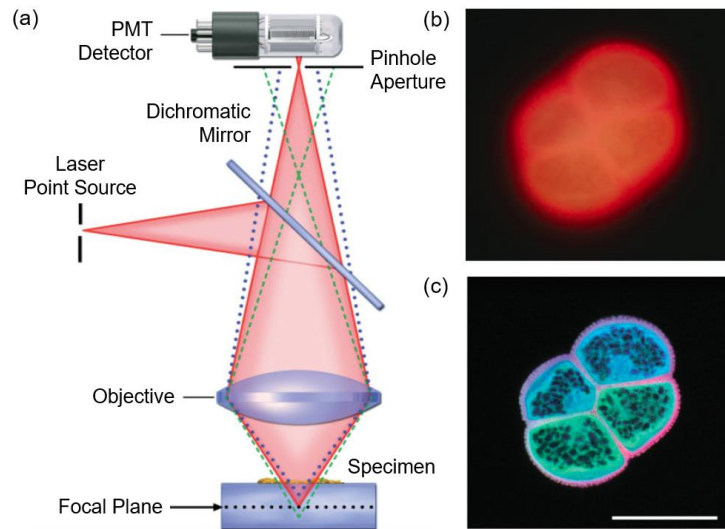
Figure 1-1 – (a) Schema of CLSM. (b) and (c) are wield field and CLSM images of autofluorescence in a pollen grain, respectively. Scale bar, 50 μm.[2]

For imaging the thick specimens like cells and tissue sections, the signal coming out of the focal plane will blur the image in traditional wield-field microscopy. CLSM can overcome this problem, by illuminating the sample with a "point" source, and putting a "conjugated" spatial pinhole in front of the electronic photon detector[2, 3]. This configuration can substantially eliminate out of the focal signal, increasing both lateral and axial resolution. In order to achieve large field of view (FOV) and fast scanning image, CLSM uses high speed scanning mirror to achieve point or line scanning.
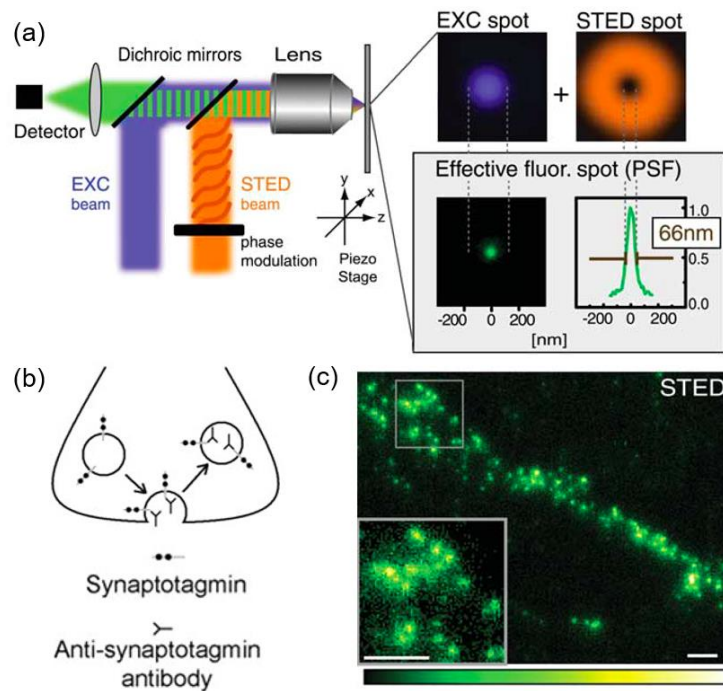
Figure 1-2 – (a) Schema of STED. (b) Mechanism of synaptic labeling. (c) The STED image of labelled synaptic nerve terminals. Scale bar, 500 nm.[4]

Super-resolution microscopy can break out the optical diffraction limit, reaching a higher resolution than CLSM[5]. Over the past ten years, there are many methods have been studied. For instance, the stimulated emission depletion microscopy (STED) employs the reversible saturable optically linear fluorescence transitions, exploits nonlinear response to sharpen the point spread function[6], and the stochastic optical reconstruction microscopy (STORM) and photoactivated localization microscopy (PALM)[7] are to localize the center of single molecule point spread function by excite close-by molecules at different time. These super-resolution microscopies can obtain tens of nanometers resolution.

OCT has gained a lot of interest in clinical application, especially ophthalmology[8-11]. Light output from the low coherence source is transmitted into a 2×2 beam splitter, one of which is sample beam that is directed onto the sample to be imaged, and the other one is the

reference beam with a variable path length. The light being scattered from sample interferences with reference beam, and is detected by a photodetector or spectrometer. With interference, OCT can reach a high axial resolution in much deeper region than CLSM. Besides providing structural information, Doppler OCT can detect the vessel velocity.
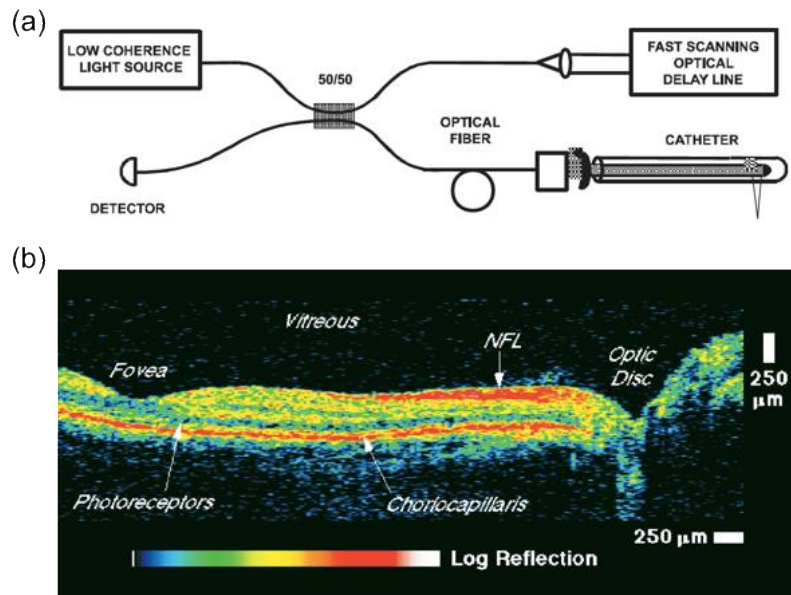
Figure 1-3 – (a) Schema of OCT. (b) Pseudo-color OCT image of human retina[12]. NFL, nerve fiber layer.

However, tissue strong light scattering significantly limits the imaging depth of pure optical microscopy. In addition, pure optical microscopy highly relied on scattering and fluorescence labeling; and the sensitivity of optical absorption is relatively low.

1.2 Photoacoustic Microscopy

Emerging as a new technique, photoacoustic microscopy (PAM) shows advantages to cover the shortage of pure optical microscopy. This section will give an introduction to mechanism and modalities of PAM.

1.2.1 Principle of Photoacoustic Tomography

PAM is based on the PA effect. This effect refers to the phenomenon that being illuminated by pulsed or modulated electromagnetic (EM) radiation, an object will transfer the absorbed light energy into heat, emitting acoustic waves as the consequence of thermos-expansion effect. PA effect was first reported by Alexander Graham Bell in 1880, and was first applied in biomedical field in 1970s[13, 14]. Until the last decade of the 20th century, the blooming period of PA study in biomedicine arrived[15-17].
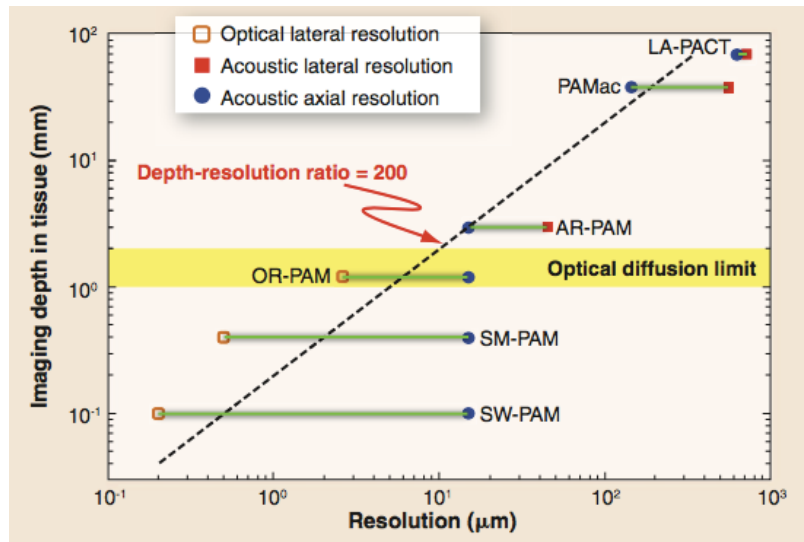
Figure 1-4 – Imaging depth versus resolution. SW, Subwavelength; SM, submicrometer; LA, linear array.[18]

Generation of PA signal in tissue goes through three steps: absorption of EM by optical absorber, increase of local temperature, and propagation of acoustic wave in tissue.
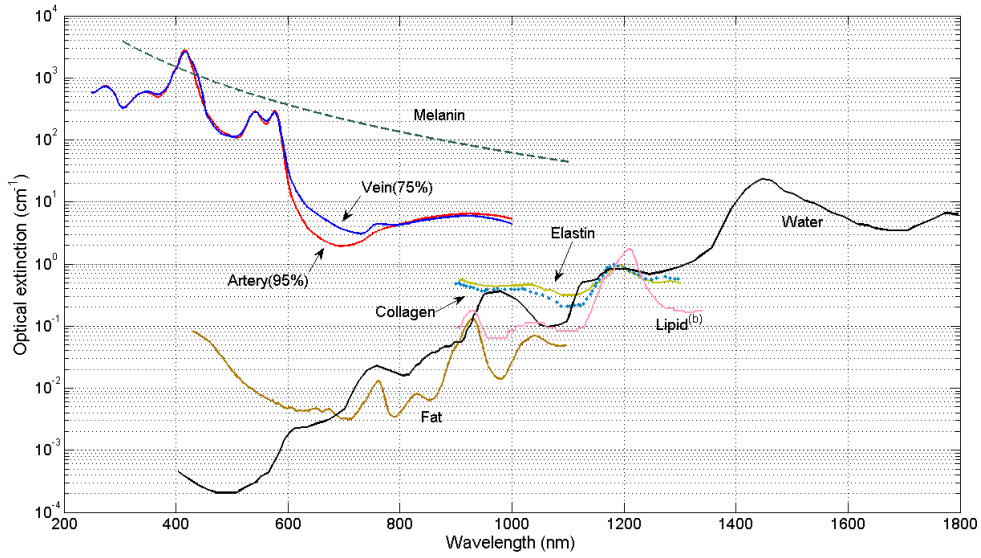
Figure 1-5 – Absorption coefficient of common absorbers in living tissues.

For living tissue, there are many typical intrinsic optical absorbers (chromophores), including water, blood, and melanosome. Figure 1-5 shows the optical absorption coefficient of common absorbers in living tissues, from the visible to infrared spectrum. After absorbed by the chromophores, the light energy will change into mechanical energy, and propagates into surrounding tissues as acoustic wave.

All our simulation modeling is based on the theoretical process of PA signal generation. Light energy absorbed by the chromophores can be changed into the elastic expansion. According to the thermodynamic equation, change of volume can be represented as,

$$dV = \left(\frac{\partial V}{\partial p}\right)\bigg|_T dp + \left(\frac{\partial V}{\partial T}\right)\bigg|_p dT = -\kappa V dp + \beta V dT, \qquad (1)$$

where V, p and T are volume in cm³, pressure in Pa and temperature in K respectively, κ is adiabatic compressibility, and β is the isobaric volume expansion coefficient. When the light source is short pulsed laser, the expansion of volume can be ignored. So we can acquire

$$\frac{dV}{V} = -\kappa p + \beta T = 0,$$

(2)

and

$$T = \frac{A_e}{\rho C_v} = \frac{\mu_a F}{\rho C_v},$$

(3)

where A_e is absorbed energy density in J m⁻³, C_v is isochoric specific heat in J kg⁻¹ K⁻¹, ρ is density, μ_a is absorption coefficient and F is optics fluence in J cm⁻². When the Eq. (3) is put into Eq. (2), the initial pressure generated by the pulsed laser can be derived,

$$P_0(\mathbf{r}) = \frac{\beta T}{\kappa} = \frac{\beta}{\kappa \rho C_v} A_e(\mathbf{r}) = \Gamma A_e(\mathbf{r}) = \Gamma \mu_a F,$$

(4)

where Γ is Grueneisen coefficient. For soft tissue at room temperature, $\beta \sim 4 \times 10^{-4}\ K^{-1}$, $C_v \sim 4 \times 10^3\ Jkg^{-1}K^{-1}$, $\rho \sim 10^3 kgm^{-3}$, and $\kappa \sim 5 \times 10^{-10} Pa^{-1}$, lead $\Gamma \sim 0.2$. Γ can be changed with temperature, thus the PA signal can also monitor the temperature variation in living tissue.

Under the stress confinement condition, Morse and Diebold *et al* demonstrated the PA pressure generated in an acoustically homogenous and non-viscous medium[19, 20]:

$$\nabla^2 p(\mathbf{r}, t) - \frac{1}{v_s^2}\frac{\partial^2}{\partial t^2} p(\mathbf{r}, t) = -\frac{\beta}{C_p}\frac{\partial}{\partial t} H(\mathbf{r}, t),$$

(5)

where $H(\mathbf{r}, t)$ is the heat function, representing the converted heat amount at spatial position

r and time t per unit volume per unit time, C_p is the isobaric specific heat in $JK^{-1}kg^{-1}$. Because

the duration time of laser is so short, that the heated process can be treated as a δ function,

$$H(\mathbf{r}, t) \approx A_e(\mathbf{r})\delta(t), \tag{6}$$

Eq. (5) can be solved by Green function. Thus, in an infinite homogenous and non-viscous

medium, the PA wave equation can be solved as,

$$
\begin{aligned}
p(\mathbf{r}, t) &= \int dt' \int d\mathbf{r}' G(\mathbf{r}, t; \mathbf{r}', t') \frac{\beta}{C_p} \frac{\partial H(\mathbf{r}', t')}{\partial t'} \\
&= \frac{\beta}{4\pi C_p} \int d\mathbf{r}' \frac{1}{|\mathbf{r} - \mathbf{r}'|} \frac{\partial H(\mathbf{r}', t - \frac{|\mathbf{r} - \mathbf{r}'|}{v_s})}{\partial t} \\
&= \frac{\beta}{4\pi C_p} \frac{\partial}{\partial t} \int d\mathbf{r}' \frac{1}{|\mathbf{r} - \mathbf{r}'|} H(\mathbf{r}', t - \frac{|\mathbf{r} - \mathbf{r}'|}{v_s})
\end{aligned} \tag{7}
$$

Substituting Eq. (6) into Eq. (7), yields

$$
\begin{aligned}
p(r, t) &= \frac{\beta}{4\pi C_p} \frac{\partial}{\partial t} \left[\frac{1}{v_s t} \int d\mathbf{r}' A(\mathbf{r}') \delta(t - \frac{|\mathbf{r} - \mathbf{r}'|}{v_s}) \right] \\
&= \frac{1}{4\pi v_s^2} \frac{\partial}{\partial t} \left[\frac{1}{v_s t} \int d\mathbf{r}' p_0(\mathbf{r}') \delta(t - \frac{|\mathbf{r} - \mathbf{r}'|}{v_s}) \right]'
\end{aligned} \tag{8}
$$

where p_0 is the initial pressure in Eq. (4). Apparently, Eq. (8) tells that the PA pressure at

spatial position r and time t comes from the accumulated initial pressure along the spherical

surface whose center is r and radius is $v_s t$. When a spherical absorber centered at $\mathbf{r}_s$ with radius

of a, is illuminated by a pulsed laser, its inner part will generate the initial pressure $p_0(\mathbf{r}) = A_0 U(a - |\mathbf{r} - \mathbf{r}_s|)$, where $U(x)$ is step function. When $x \geq 0$, $U(x) = 1$, and when $x < 0$,

$U(x) = 0$. Combined with Eq. (8), at position $\mathbf{r}_0$ and time t, the analytical acoustic pressure

solution is

$$p(\mathbf{r}_0, t) = A_0 U(a - |R - v_s t|)(R - v_s t)/(2R), \qquad (9)$$

where R=|$\mathbf{r}_0$ - $\mathbf{r}_s$|. The solution model and related PA signal is showed in Fig. 1-6.

(a)   (b)
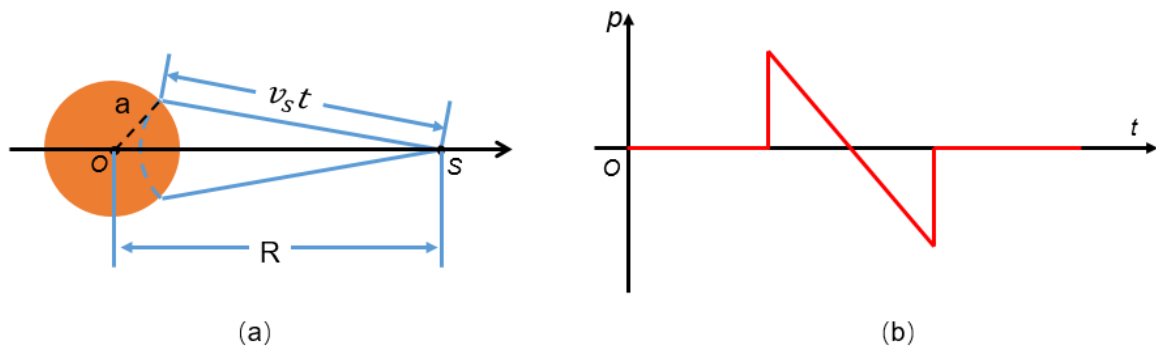
Figure 1-6 – Solution model and related PA signal of spherical source.

Apparently, Fig. 1-6 (b) is a "N"-shape curve, and stands for PA signal of spherical source

which is detected by the transducer at position r. It has to be mentioned, the pressure has both

positive and negative values. And the amplitude is *p_0R/d,* which is proportional to the volume

of absorber and reciprocal to the distance between transducer and absorber. Because in virtual

circumstance, detected distance is much larger than the volume of PA source, inducing the

detected pressure is much lower than the initial pressure. Moreover, the width of signal is

$2R/v_s t$, thus the smaller absorber, the higher frequency of detected signal.

The above solution is induced in homogenous and non-viscous medium, which is not the

real situation. Thus it is important to introduce how the tissue influences the propagation of

acoustic wave. When the acoustic wave diffuses in the tissue, two consequences will come:

scattered or attenuated. Normally, in soft tissue, the scattering effect is too low to be neglected, leading US imaging to be one of most popular diagnosis method. However, the attenuation effect cannot be ignored, especially when the acoustic wave has high frequency or passes through high absorption medium like skull. In soft medium, attenuation coefficient is about -0.3 dB (cm MHz)$^{-1}$ for low and medium frequency, and -3 dB (cm MHz)$^{-1}$ for high frequency[21]. Thus with higher frequency, the degree of attenuation will become higher, so that we can treat the tissue as a low-pass filter for acoustic wave.

Unlike the pure optical microscopy, PAM detects the generated PA signal by ultrasound transducers to determine the position of chromophores. PAM has several unique characteristics: i) Due to low acoustic scattering in tissue, PAM can overcome the barrier in the imaging depth for pure optical microscopy, with the acoustic resolution; ii) PAM has a high sensitivity of tissue optical absorption.

1.2.2   Modalities of Photoacoustic Microscopy

Depending on the method used to determine the lateral resolution, PAM can be divided into two categories: acoustic-resolution PAM (AR-PAM), and optical-resolution PAM (OR-PAM).

1.2.2.1   <u>AR-PAM</u>

Pure optical imaging depth is limited by the ballistic regime (~ 1 mm), beyond which the dominating diffusion will largely decreases the optical focusing ability, leading to a low resolution. Because the acoustic scattering is much smaller than optical scattering in the tissue,

this makes the acoustic focusing largely easier than optical focusing. AR-PAM just takes advantages of acoustic focusing property, and uses a focused transducer to detect PA signal. While, the diffused illuminating laser excites the absorber in the diffusive regime to generate PA signal. The lateral resolution $R_{l,AR}$ is related with acoustic numeric aperture (NA), and central frequency f_0 of transducer,

$$R_{l,AR} = 0.61 \frac{v_s}{NA \cdot f_0}. \tag{10}$$

The axial resolution $R_{a,AR}$ is related with transducer's bandwidth Δf, and can be derived from the time-resolved signal,

$$R_{a,AR} = 0.88 \cdot \frac{v_s}{\Delta f}. \tag{11}$$

In the reflection mode of AR-PAM, if laser is perpendicularly illuminated in bright field way, absorbers in skin (like melanin) will generate strong PA signal and could reverberate inside imaging system, overlapping the signal that is from deeper tissue. Thus, in 2005, Maslov et al. developed a dark-field illumination method to overcome this problem[22]. Fig. 1-7 (a) is the common used method, in which laser was reflected by a conical lens, making the laser pattern changed into a ring, and after another reflection by condenser, light will be condensed into the tissue as 40-50 degree with skin surface, like Fig. 1-7 (b) showed[23]. Transducer was coaxially aligned with the center of light focus. Finally, there was a donut-shape pattern light illuminating on the skin under the transducer. By this way, the detected skin signal was substantially decreased, and the image quality of deeper tissue was improved.
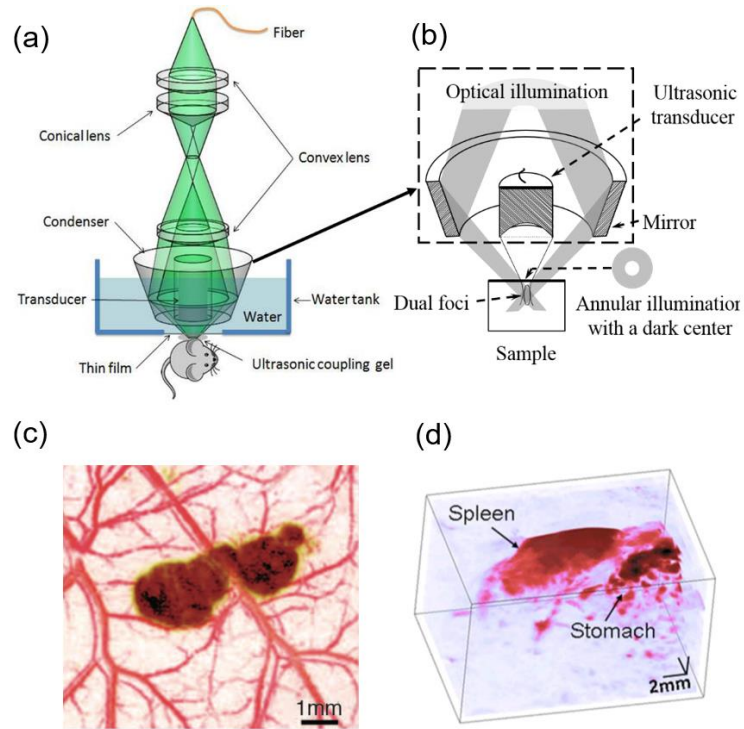
Figure 1-7 – Experimental setup and result of Reflection mode AR-PAM. (a) Setup schema. (b) Zoom in of illumination and detection method. (c) Melanoma and surrounding circular system[24]. (d) Spleen and stomach image[25].

AR-PAM can be used to image from tissue to organ, depending on the used transducer and light wavelength. Lateral resolution of AR-PAM is decided by the central frequency and NA. of transducer, as mentioned in Eq. (10). High frequency can achieve a higher resolution, but the severe acoustic attenuation will decrease the imaging depth. So the NA. and central frequency of transducer should be chosen carefully to match the requirement of imaging depth or resolution. Maslov *et al.* used 50 MHz transducer to image melanoma and surrounding circular system with 45 μm lateral resolution and 3 mm imaging depth (Fig. 1-7 (c))[24], and *Song et al.* used lower frequency (5 MHz) transducer to image deeper organ (Fig. 1-7 (d))[25].

1.2.2.2 <u>OR-PAM</u>

In order to achieve a very high resolution, like 5 μm lateral resolution, the central frequency of AR-PAM should be 300 MHz. However, at this frequency, the acoustic attenuation coefficient of tissue is up to -80 dB mm^{-1}. Therefore, light focusing is used instead, that is OR-PAM.

Relying on the optical focusing, lateral resolution of OR-PAM, $R_{l,OR}$, is related with optical wavelength λ and NA. of optical focusing lens,

$$R_{l,OR} = 0.51 \frac{\lambda}{NA.},$$

(12)

and the axial resolution is also derived from the time-resolved acoustic detection like AR-PAM. To achieve the high sensitivity for OR-PAM, focused transducer is coaxially and confocally positioned with laser focusing. There are three ways to achieve: i) Laser is perpendicularly illuminated on the sample and acoustic wave is reflected. Song $et\ al.$ (2011) used interface of silicon oil and prism to reflect the generated acoustic wave and separate its pathway from the laser[26]. Lateral resolution of this setup can reach 2.14 μm at 570 nm, and they have imaged single capillary vessel. The imaging head of setup and experimental result is shown in Figure 5 (a) (b); ii) Laser is reflected while transducer is vertical to the sample. In this setup, a very thin metal membrane can be used as the coupling medium between two right angle prism to transmit the US and reflect the light. Wang $et\ al.$ (2011) developed a fast voice-coil scanning OR-PAM, in which US transmitted through 2 right triangle prisms, and light was reflected by the aluminum coating between the prisms[27]. Lateral resolution of this system

is 3.4 μm, and it can be used to image the hydrodynamics of blood cells in microvascular system of mouse ear.
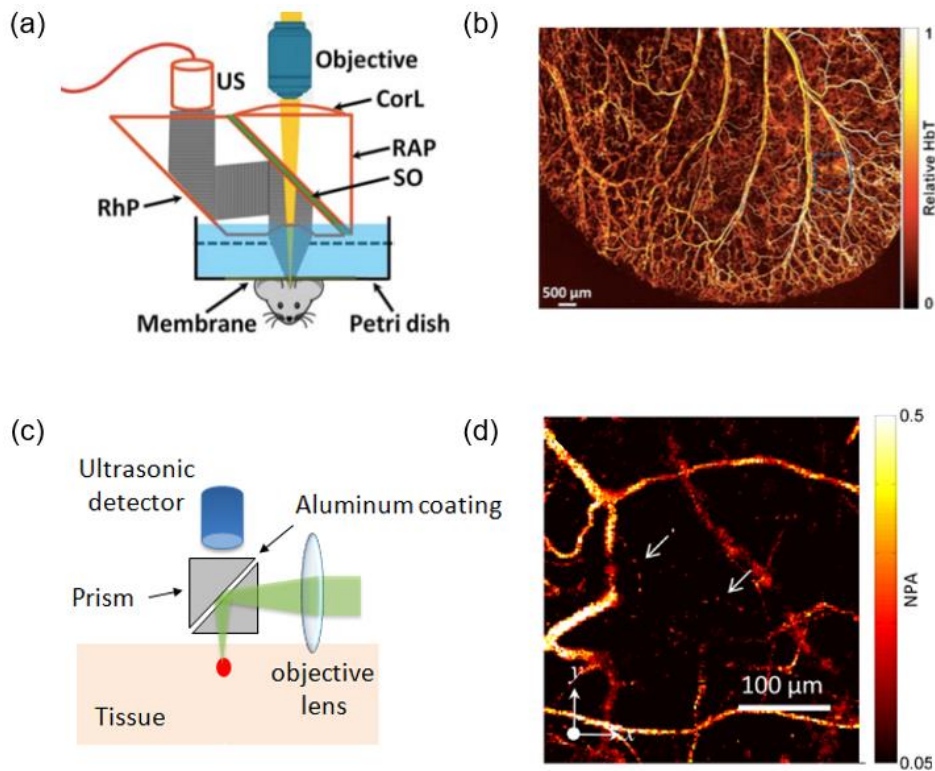
Figure 1-8 – Two typical types of OR-PAM.(a) and (b) are schema and mouse ear image of US reflection OR-PAM[26]. (c) and (d) are schema and single blood cell image of light reflection OR-PAM[27]. Arrows present signal blood cells. CorL, correction lens. RAP, RAP, right-angle prism; SO, silicone oil; RhP, rhomboid prism.

1.2.3 Photoacoustic Functional and Molecular Imaging

Optical absorption of blood highly depends on hemoglobin oxygen saturation (SO_2), which is a very important functional physiological parameter closely related with the local metabolic rate. For instance, tumor has a high cost of oxygen to support its fast mitosis, so SO_2 value in the tumor region is lower than normal tissue. Owing to its superior sensitivity to optical absorption, spectroscopic PAM has been used to detect local SO_2 value.

The primary absorber in blood is hemoglobin, which is composed of oxygenated hemoglobin (HbO2) and deoxygenated hemoglobin (Hb). SO2 is defined by

$$SO_2 = \frac{[HbO_2]}{[Hb] + [HbO_2]}, \tag{13}$$

where, [*HbO2*] and [*Hb*] are concentration of HbO2 and Hb, respectively. These two kinds of hemoglobin molecules have different absorption characteristics, whose molar extinction coefficient curves varying with wavelengths, as shown in Fig. 1-9. If $\varepsilon_{HbO2}(\lambda)$ $\varepsilon_{Hb}(\lambda)$ are the molar extinction coefficient of HbO2 and Hb, respectively, the absorption coefficient of blood can be calculated as,

$$\mu_a(\lambda, r) = 2.303 \times \left[\varepsilon_{Hb}(\lambda)[Hb](r) + \varepsilon_{HbO_2}(\lambda)[HbO_2](r)\right]. \tag{14}$$
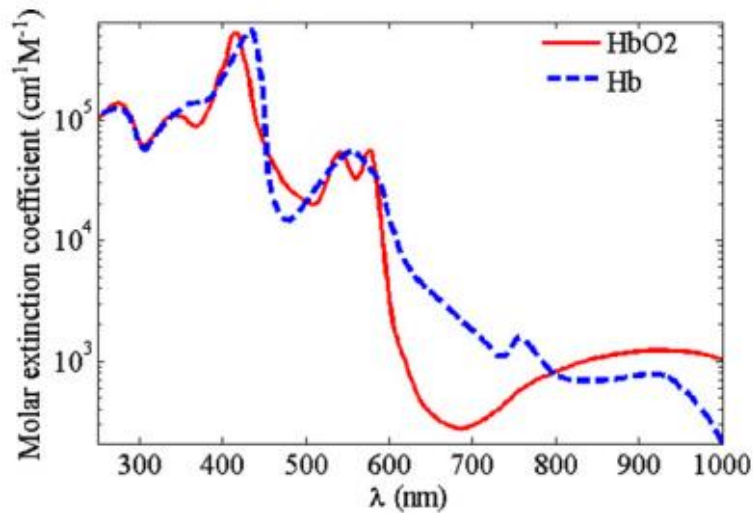
Figure 1-9 – Molar extinction coefficient of HbO$_2$ and Hb.

Eq. (4) tells that when the Grueneisen parameter is constant, and light penetration depth is larger than the vessel's diameter, amplitude of PA signal is proportional to the absorption of blood vessel and local optical fluence. Multiple wavelengths (λ_1，λ_2，…，λ_n) are used as

15

illuminating laser in spectroscopic PAT, to form a series $A_e(\lambda,r)$ distribution images. If local

fluence is known, $[HbO_2]$ and $[Hb]$ can be derived by least-square fitting as follows,

$$\begin{bmatrix} [Hb] \\ [HbO_2] \end{bmatrix}_{(r)} = (M^T M)^{-1} M^T K(r), \tag{15}$$

where,

$$M = \begin{bmatrix} \varepsilon_{Hb}(\lambda_1) & \varepsilon_{HbO_2}(\lambda_1) \\ \vdots & \vdots \\ \varepsilon_{Hb}(\lambda_n) & \varepsilon_{HbO_2}(\lambda_n) \end{bmatrix}, \tag{16}$$

$$K(r) = \begin{bmatrix} A_e(\lambda_1,r)/F(\lambda_1,r) \\ \vdots \\ A_e(\lambda_n,r)/F(\lambda_n,r) \end{bmatrix}. \tag{17}$$

Then, by substituting $[HbO_2]$ and $[Hb]$ into Eq. (13), SO_2 can be calculated. Though in

actual cases, local fluence at position r under certain wavelength is not the same, we can still

suppose they are equal for estimation when imaging the upper part of the tissue. However, in

order to acquire the accurate SO_2 value, local fluence should be calibrated.

As a method to detect SO_2 noninvasively, PAM reaches an accurate level to single blood

vessels, making it a powerful tool to study local circulation metabolism *in vivo*. Several studies

have revealed the potential of functional PAM in clinical applications. Chen *et al.* (2012)

obtained the SO_2 and carboxyhemoglobin saturation (SCO) in the mouse ear and monitored

the changes from normoxia to carbon monoxide hypoxia *in vivo*[28]. Ning *et al.* (2015)

developed a multi-parametric PAM platform and analyzed both the SO_2-encoded spectral

dependence and the flow-induced temporal decorrelation of photoacoustic signals generated

by the raster-scanned mouse ear vasculature[29]. Rowland *et al.* (2012) used PAM to image the

intestine microvascular system and measure blood flow and SO_2 in seven C57BL6 mice before and immediately after massive small bowel resection. Results showed the venous SO_2 decreased with an increase in the oxygen extraction fraction[30].

Apart from the endogenous absorbers, exogenous contrast agents extended application range of PAM to weak absorbers or even non-absorbers, like lymphatic system. These contrast agents have the property of high light absorption, improving the image sensitivity at a large scale. Excellent PA exogenous contrast agents include organic dyes and nanoparticles.

Indocyanine green (ICG) is a commonly used organic dye because it has strong optical absorption at infrared range, where blood intrinsic absorption is 20 times lower than at 532nm. Wang *et al.* (2004) obtained high contrast image of deep circular system by using ICG[31]. In addition, methylene blue was successfully applied on the sentinel lymph node imaging[32]. Besides organic dyes, various nanoparticles have been synthesized for PA imaging, such as gold nanoparticle[33], carbon nanoparticles[34], and organic nanoparticles[35]. One of the advantages of nanoparticles is that their absorption peak can be tuned, by changing the shape and size of particles.

Both organic dyes and nanoparticles can be bio-conjugated to molecular probe, forming PA molecular imaging contrast agents. Fig. 1-10 explains the principle of PA molecular imaging[36]. After being injected into the living tissue, the agents assemble around the tumor with high specificity. When the pulsed laser illuminates on the tumor region, surface PA contrast agents will generate strong signal, leading the PA signal of tumor is much higher than background.

Recent studies have indicated the potential of the combination of PAM and agent targeted at cancer as a clinical tool that can provide improved specificity and sensitivity for cancer detection. Jokerst *et al.* (2012) proposed a combined PA/Raman approach using gold nanorods (GNRs) as a passively targeted molecular imaging agent for cancer screening. They found a linear relationship between the PA signal and the concentration of injected molecular imaging agent in the 2008 cancer cell line[37]. Kircher *et al.* (2012) developed a triple-modality nanoparticle combining magnetic resonance imaging (MRI), PA and Raman imaging for brain tumor detection. This nanoparticle is accumulated and reserved by brain tumors to delineate the margins of them[38].
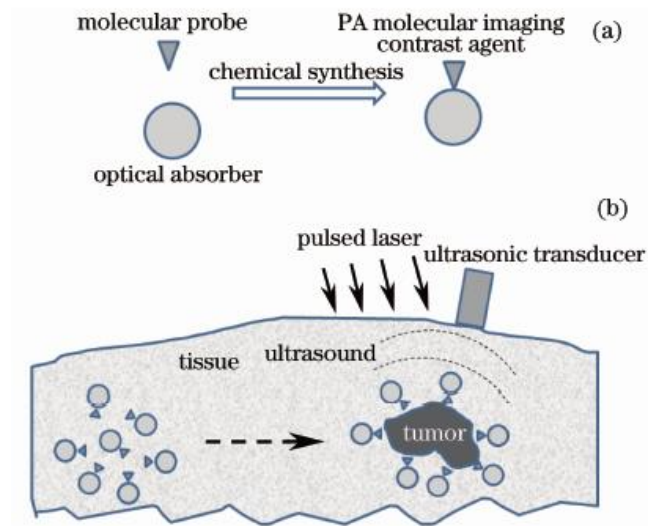
Figure 1-10 – PA molecular imaging principle.

1.3 Multi-modality PAM systems

As a large field, the biomedical optical imaging owns a lot of imaging modalities, each of which has special advantages. Combined with optics and US microscopy, some multimodality PA systems have been invented.

1.3.1 *PA/Optics Microscopy*

Some representative optics microscopies have been integrated into the PAM. Song *et al.* (2016) combined PAM with two-photon (TP) fluorescence microscopy (TPM), and second harmonic generation (SHG) microscopy (SHGM), to reveal deep complementary tissue microstructures at around 290 μm lateral resolution, which is shown in Fig. 1-11 (a) and (b)[39]. Sensitive chromophores of these three modalities are different, leading to different contrast, such as for PAM is hemoglobin, for TPM is cellular reduced nicotinamide adenine dinucleotide, and for SHGM is noncentrosymmetric structures like collagen and microtubules. This setup is promising to study tumor microvascular. Zhang *et al.* (2012) developed a PAM multi-modality system integrated with fluorescence laser scanning microscopy (LSM) and OCT for ocular imaging, which is shown in Fig. 1-11 (c) and (d)[40]. With fine axial resolution, OCT guides the position for the other two modalities. PAM are capable of imaging hemoglobin and melanin, and with specially labeled cell types, LSM cam provide complementary information about ocular diseases, like retinitis pigmentosa. Thus, this system provides a promising method in ophthalmology.
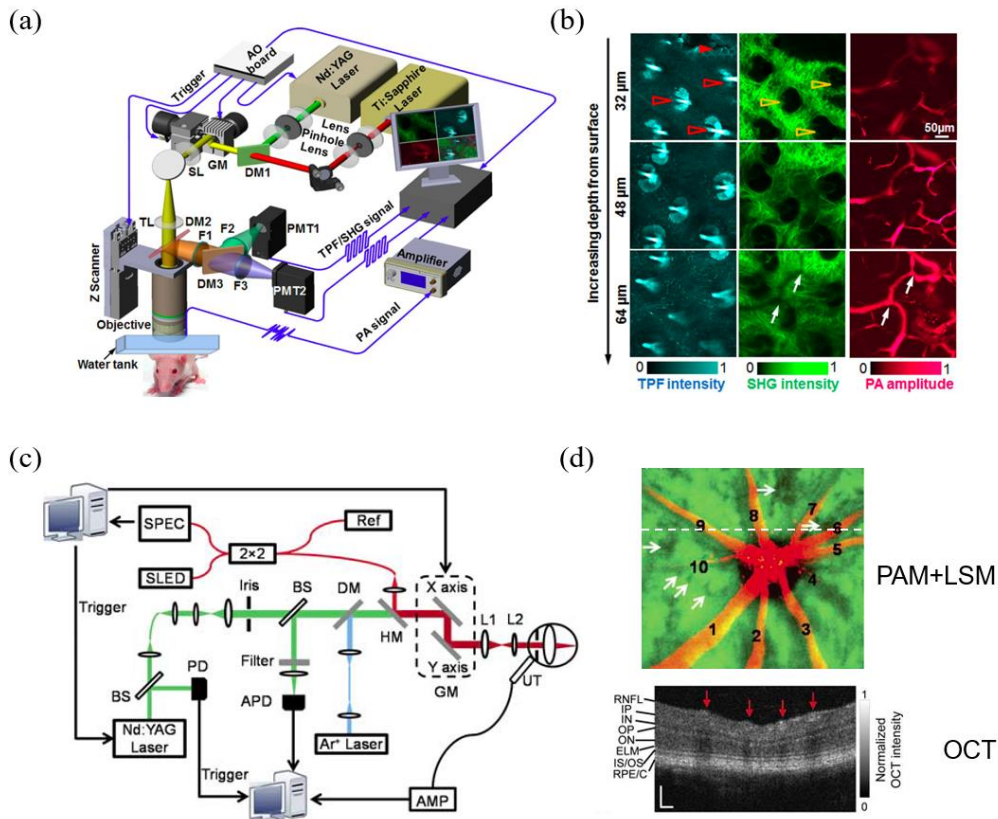
Figure 1-11 – Schema (a) and mouse ear image (b) of PA/TP/SHG microscopy [39]. Schema (c) and mouse retinal image (d) of PAM/LSM/OCT [40].

1.3.2   PA/US Microscopy

Due to the low attenuation of acoustic wave in tissue, US is used as a common, noninvasive method to image deep tissue structures, which can provide position guidance for PA. Unlike optics microscopy, US microscopy can broaden the image depth above millimeter scale. Roger *et al.* (2009) developed an AR-PAM/US system by using custom-build light deliver probe, which is shown in Fig. 1-12 (a)[41]. Fig. 1-12 (b) is the fusion image, in which PAM can obviously image the finger vessel that is not presented in US image. With the voice coil, the setup can achieve a high scanning speed. Another AR-PAM/US was developed by Adam *et al.* (2010) to do ocular imaging[42]. The 15 MHz or 25 MHz focused transducer is focused on the retina surface, to acquire whole eye image at one frame for PA or US mode.

However, for both PA/US microscopies, which are based on the acoustic focusing, the resolution of PA image is limited.
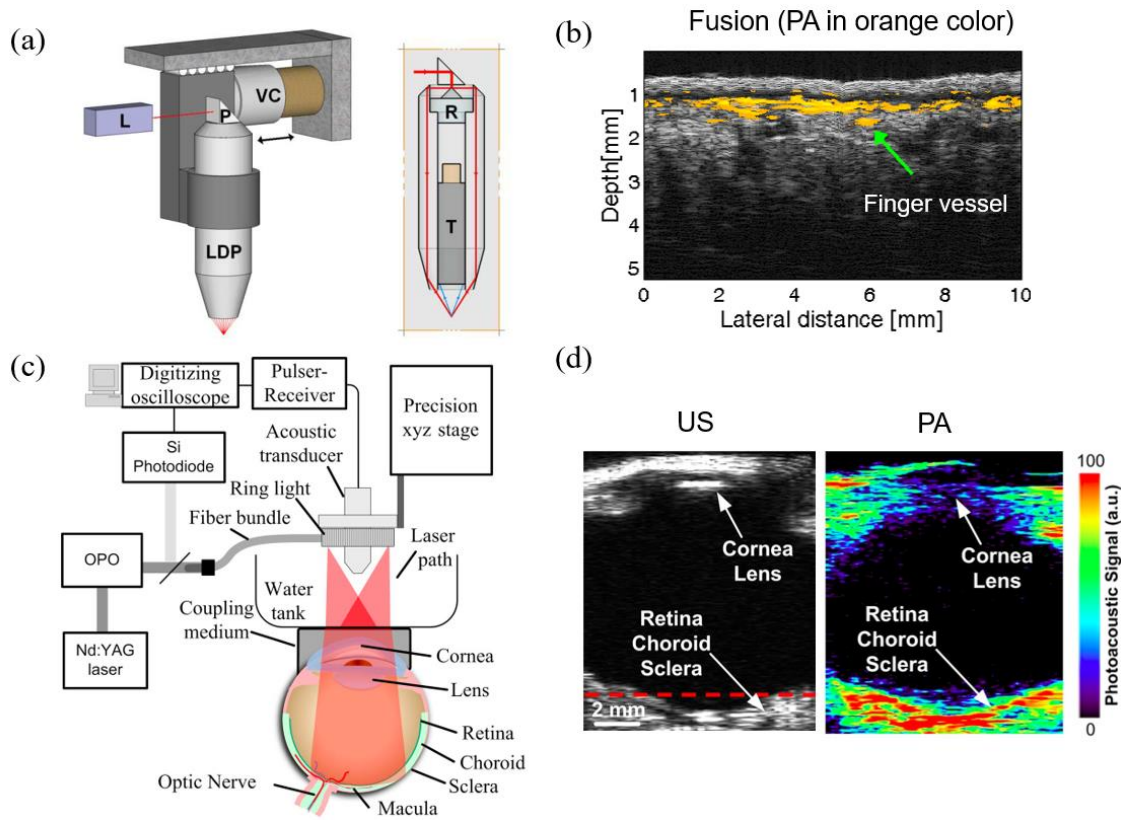
Figure 1-12 – PA/US microscopy. (a) and (c) are two schemas, and (b) and (d) are their corresponding image[41, 42].

1.3.3   PA/US/Optics Microscopy

Jiang *et al.* (2015) developed a miniature probe which integrated PAM, OCT and US imaging, as shown in Fig. 1-13[43]. In this system, light was transmitted by a signal mode fiber (SMF), then focused by a custom-designed GRIN lens (GL), during which was reflected by a gold coated film (GCF). Generated US transmitted the gold coated film and received by the transducer. OR-PAM and OCT contribute the high lateral and axial resolution to this system,

which are 13.6 µm and 14.3 µm, respectively. With endoscopic design, this system is suitable for imaging internal organs.
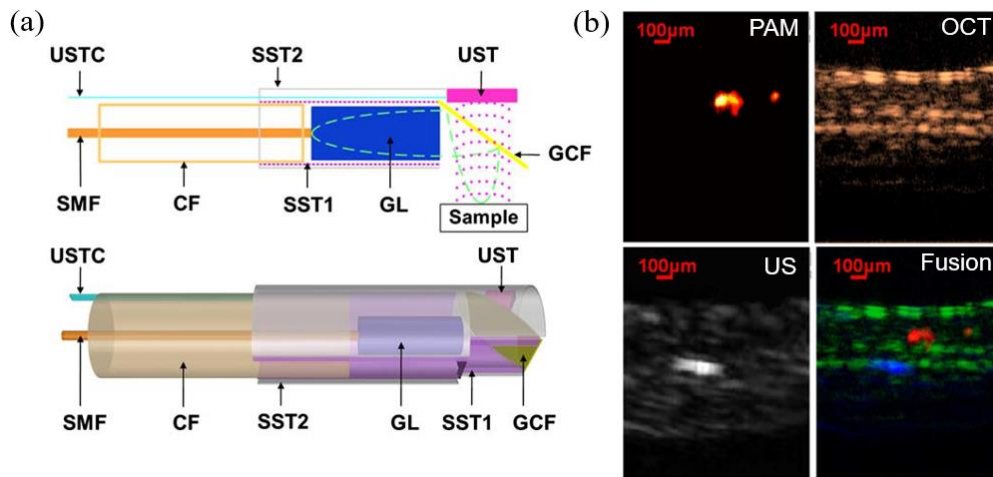
Figure 1-13 – Schema (a) and rat ear vessel image (b) of PA/US/Optics microscopy [43].

1.4 Motivation for High-resolution PA/US Microscopy

PA/US dual modality system has some advantages. Firstly, combing PA and US, we can not only see distribution of different tissues, but also the strong absorbers which are mostly interested in. Because PA is based on the chromophore's intrinsic optical absorption, achieving 100% sensitivity. The non-absorbing tissue components don't generate any signal, making PA a background-free and high contrast imaging method. Meanwhile, US imaging is based on the mismatching of acoustic impedance between different tissues. Due to the low scattering of US, it can provide a deep penetration imaging, making US a very good way to locate the position inside the tissue.

Secondly, PA/US system can provide both functional and structural information of the tissue, making it a promising method to be applied in the clinical. Because US is a

conventional way to do structural image. With multiple wavelengths, spectroscopic PA can provide functional information, especially SO_2, which is an important parameter to understand hemodynamics, investigate neural activity, pre-diagnose the tumor, and also it is a precious way to evaluate the effects of chemotherapy and radiotherapy on tumors, monitoring the healing of wounds, and studying gene expression[44-49].

In section 1.3.2, we have introduced two PA/US microscopy designs. Based on the AR-PAM modality, two systems have a deep imaging depth, while the lateral resolution is limited. A high resolution PA system is capable to clearly shape tiny interested tissues, providing a significant method to investigate microvascular system and separate closely adjacent tissues, which is a potential imaging method for anatomy and pathology. However, the current developed representative OR-PAM systems have the limitations to integrate the US mode. System developed by Zhang *et al.* (described in Fig. 1-11 (c)), uses unfocused transducer to cover the scanning area of focused light, leading the sensitivity is decreased. Meanwhile this system isn't able to do US imaging due to unfocused transducer. Another system is developed by *Wang et al.* (described in Fig. 1-8 (a)), in which generated acoustic wave have to go through multiple reflection before being detected by transducer. Thus, the background pulse-echo signal will be added onto the interested target by time resolving, leading a confusing US result. Avoiding these problems, our systems described in this thesis can achieve a high resolution PA/US image, showing potential for clinical diagnosis.

1.5   Conclusion

As the introduction part, this chapter firstly gave an introduction of PA effect and major modalities of PAM. PA effect is defined as the process that photon absorbed chromophores transfer the light energy into heat, and induces acoustic waves propagating in surrounding tissues. Based on the intrinsic absorption, PAM can provide high contrast information of chromophores, like hemoglobin and melanin with high resolution. Combined with other biomedical imaging modalities, PAM will provide complementary information of tissues. Some multi-modality PAM systems have been developed, integrated with pure optics microscopy and US imaging technique, which are described in this chapter. Combined with US modality, complementary structure information will be provided by PA/US, offering a position guidance for PAM. The main purpose of this thesis is to develop novel high resolution PA/US microscopies, the motivation of which is also described.

All in all, this chapter clarifies the importance and strengths of the PA/US system, and provides the basic idea and theoretical analysis foundation for the next chapters.

CHAPTER 2.   DEVEOPMENT OF PA/US MICROSCOPY SYSTEMS

We have developed three PA/US systems, which will be introduced in this chapter. Section 2.1 describes a mechanical scanning based PA/US microscopy. To improve the acquisition speed and flexibility, section 2.2 introduces two fast scanning PA/US microscopies accomplished by water-immersible microelectromechanical systems (MEMS) scanning mirror with parabolic reflector (PR) and with parabolic mirror (PM).

2.1   Mechanical Scanning Based PA/US Microscopy

This section gives a complementary introduction to the design of mechanical scanning PA/US microscopy which includes hardware design, control and acquisition program by LabVIEW, and image reconstruction. At last, the PA test by carbon fiber demonstrates the high resolution of our setup.

2.1.1   Hardware

Fig. 2-1 is the schematic diagram of the mechanical scanning based PA/US dual-modal microscopy. Fig. 2-1(a) clearly shows the main components of this system, which includes:

1) Laser source:

The laser source of this imaging system was semiconductor pulsed laser (Elforlight SPOT-10-100-532; pulse width< 1.8 ns), whose wavelength was 532 nm, single pulse energy was 10 μJ, and the repetition rate could reach up to 50 kHz. This laser needed extra synchronized triggers.

2) Motion controller:

A 3D translational stage (Zolix) was used to make the detection probe move on a plane. The resolution of the X and Y axis was 1 μm. This stage could output a trigger signal to synchronize the laser pulse and data acquisition.
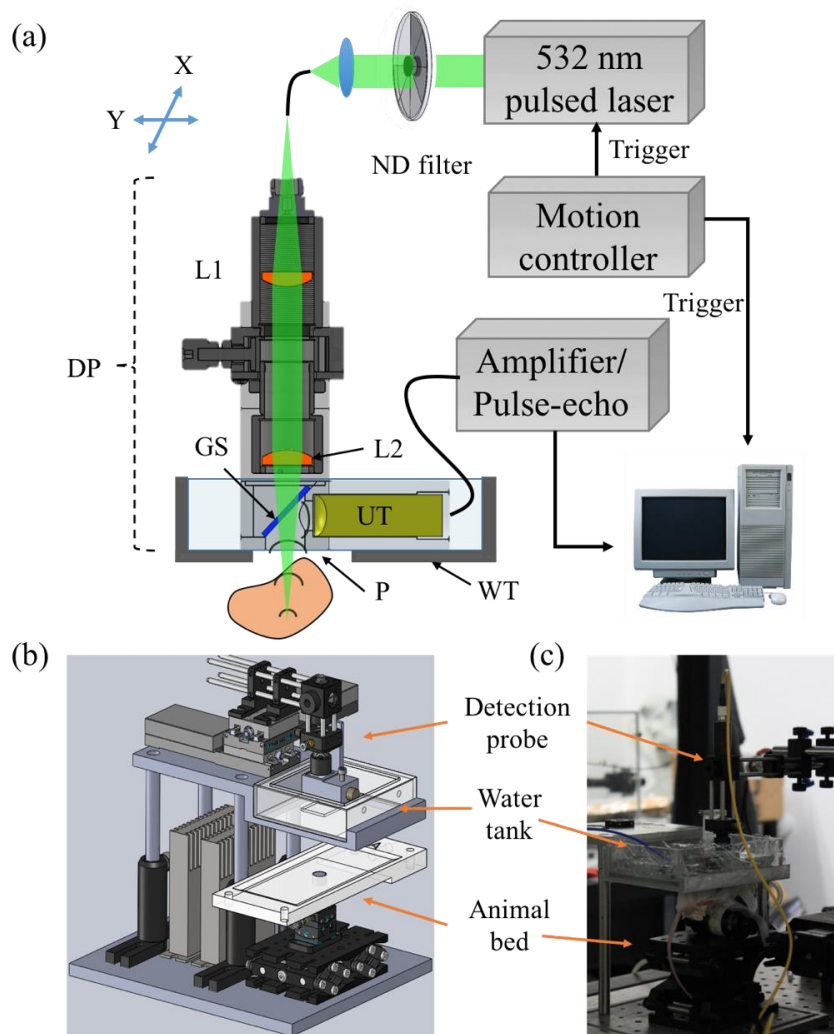
Figure 2-1 – Mechanical scanning based PA/US microscopy. (a) schematic diagram [50]. (b) and (c) are prototype design and photo of imaging part. ND, neutral-density. L1, collimated lens. L2, focusing lens. GS, glass slide. P, plastic membrane. WT, water tank.

3) Light path:

The irradiation laser pulses (532 nm) generated by the laser was coupled into a single-mode fiber, after going through a neutral-density filter, whose function was to adjust the energy of laser to satisfy laser safety standard. The laser output from fiber (Connect Fiber Optics., single mode, 460 HP, FC/PC) was focused by collimated and focusing lenses (China Daheng Group, Inc., NA: 0.25).

4) Imaging probe:

This was the most important part of the system, which was amounted on the translational stage, accomplishing 2D scanning. This part was responsible to make laser and ultrasound path coaxially and confocally aligned. It contained two lenses, a glass slide, a transducer and the holder part. The focusing lens was amounted on an adjustable lens tube, to make sure the same focusing plane of light and transducer. The glass slide which permitted the light transmission but reflected ultrasound was obliquely placed in a water cube at 45 degrees. Thus the light and ultrasound waves could share the same route within the sample. A spherically focused transducer (Olympus V324-SM; active diameter 6.35 mm, focal length 25.4 mm, center frequency 25 MHz) was horizontally fixed on the probe, to detect the PA signal and to perform pulse-echo US imaging.

5) Water tank

Because high frequency ultrasound is decreased largely on the air, it is necessary to use a water tank to immerse acoustic pathway. Water tank was custom-built with a window on the bottom. When doing the experiment, there was a very thin plastic membrane covering and sticking on the inner surface of the tank, through which light and US passed with little attenuation.

6) Amplifier/ pulse-echo

    Olympus pre-amplifier 5072PR (Gain, 0-59 dB; frequency, 1 kHz – 35 MHz) was used in this part, which has two functions, pre-amplifier in PA mode, and ultrasound pulse-echo system in the US mode. As a pre-amplifier, the noise of it is 70 µV peak-to-peak, which is suitable for our experiment. In order to get a higher magnification, another low noise amplifier Mini-Circuits ZFL-500 (Gain, 20-25 dB; noise, 4.2 dB; frequency 0.05-500 MHz) was put in front of the 5072PR. However, only Olympus 5072PR was used in pulse-echo mode, which emitted certain frequency ultrasonic pulse, and received the ultrasound signal at the interval.

7) Acquisition card

    After amplified by the amplifier, the PA/US signal was transferred into the electrical signal, and received by the acquisition card (GAGE CompuCcope 14200; sampling rate, 200 MHz). Then signal was saved as txt documents, by each B-scan.

8) Animal bed

    The animal was put on the custom-built bed, after being anaesthetized, the height of which can be adjusted. Between the animal and water tank, ultrasonic gel was used to couple the imaging region of animal and plastic membrane of water tank. During the experiment, the animal kept still.

2.1.2   Control and Acquisition Program
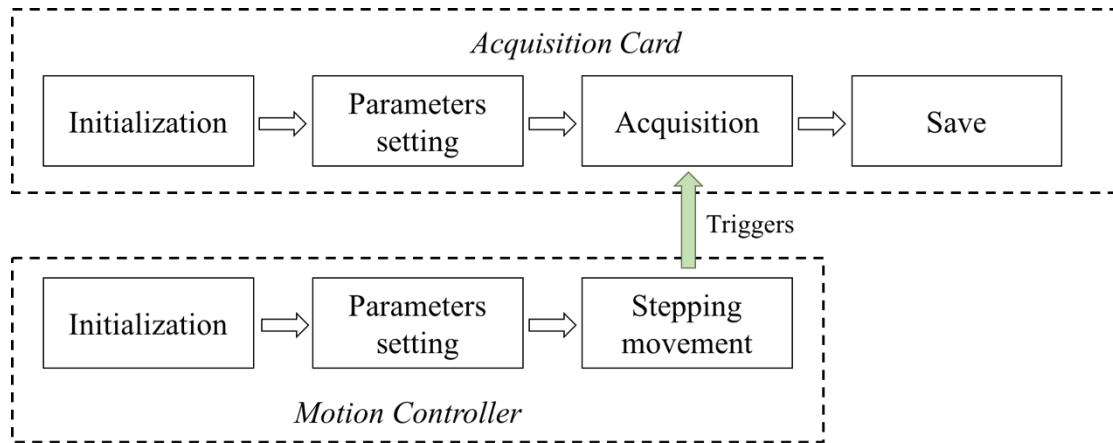
Figure 2-2 – Flow chart of LabVIEW program. Green arrow is hardware connection.

LabVIEW software was used to write the controlling program, in order to synchronize the laser, motion controller (MC) and acquisition card (AC), and save the data. Fig. 2-2 is the flow chart of the LabVIEW program, who contains two parts: one is the acquisition card and another is motion controller. Laser was also controlled by the trigger generated from motion controller, which wasn't included in this figure. Fig. 2-2 clearly shows that initialization and parameters setting of MC and AC, were about at the same time. The whole imaging process lasted from start to end of MC movement. Each step of MC gave a trigger signal to AC, to get A-line information. The movement of MC was line by line, to achieve a 2D plane scanning. Data acquisition and laser shot occurred in X positive direction. After each line scanning, 2D data was saved as a txt profile.
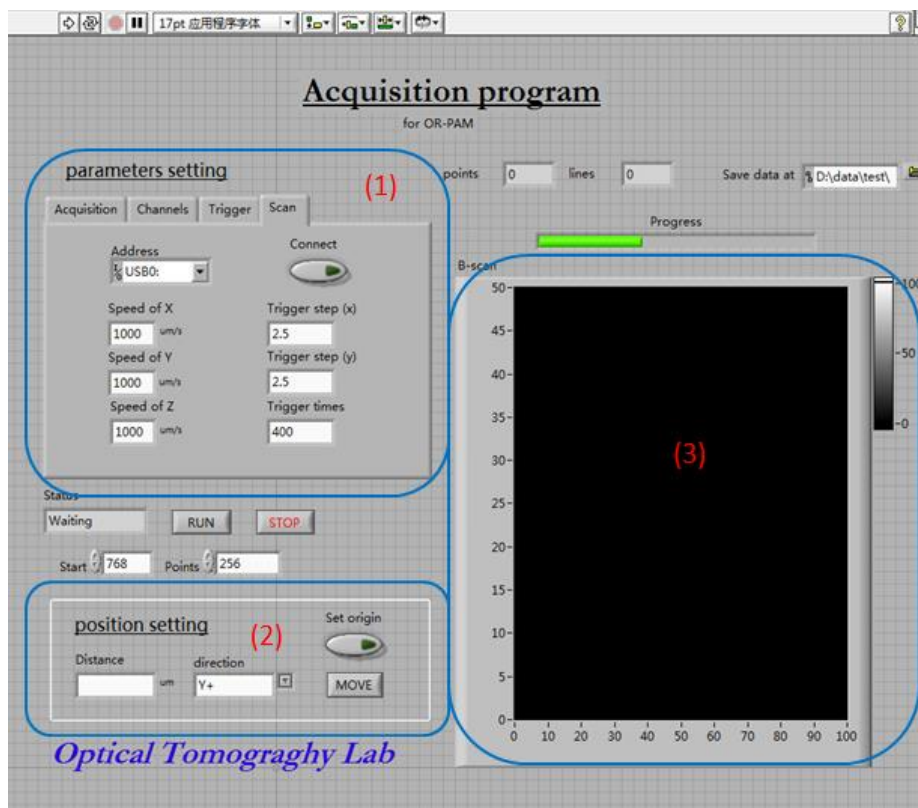
Figure 2-3 – LabVIEW window of mechanical scanning based PA/US microscopy.

Fig. 2-3 is the program control window of mechanical scanning based PA/US microscopy. In the parameters setting part, the trigger delay time and acquisition length of the AC, speed and step size of MC could be set. The position setting part was used to adjust the position of the translational stage, making sure the satisfied field of view. By pushing the set origin button, current position was set as the start. During scanning, each B-scan image would be shown on the part 3.

2.1.3   Image Reconstruction and Processing

Software   **Procedure**

Matlab — Data format conversion

- Replacing abnormal A-line

Matlab — Denoising

- Bandpass filtering

- Replacing abnormal isolated values

Matlab — B-scan image output

- Extracting the envelope

VolView — 3D image formation
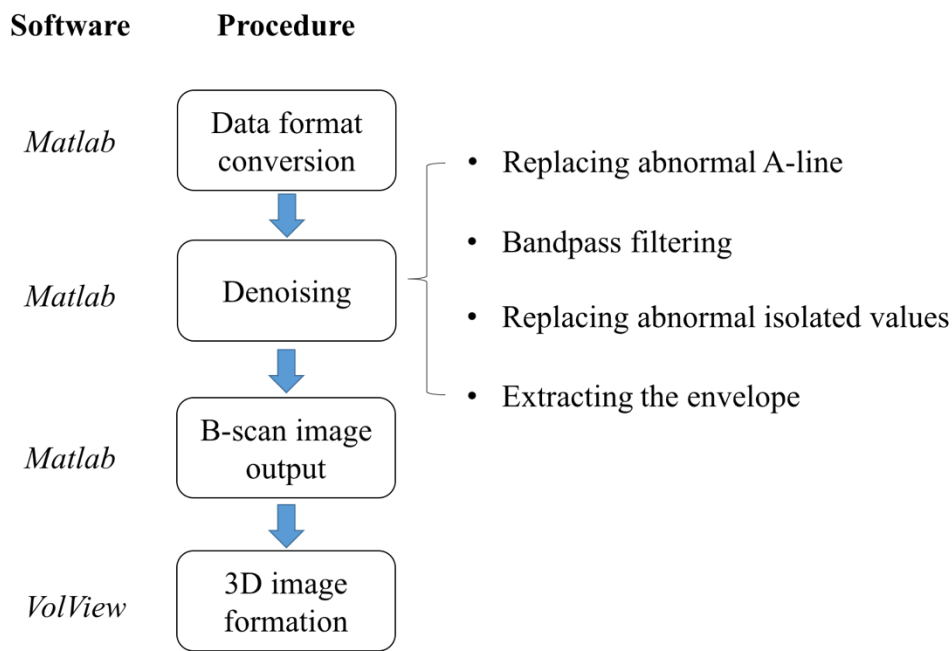
Figure 2-4 – Image reconstruction and processing flow of PA/US data.

After the acquisition finishes, we can get a serial alphabetical txt documents, one of each represents a B-scan information. Fig. 2-4 gives the image reconstruction and processing flow of PA/US data, which includes four steps: (i) To make preparation for next process, the data format is changed from txt to mat; (ii) This step is the most important one, which will improve the image quality. Though high signal to noise ratio (SNR) is one parameter for a good imaging system, the after-processing is also important. In this procedure, in order to clear background noise and increase the contrast of the image, there are four sub-steps: replacing abnormal A-line with nearby A-line, bandpass filtering matching the frequency of transducer, replacing abnormal isolated values with standard deviation, and extracting the envelope by getting absolute value after Hilbert transformation; (iii) Each B-scan profile should be changed into image type for presentation and 3D image formation; (iv) By arranging the B-scan images

31

along special distribution, 3D image is formed. The first three steps are all used MATLAB, and the last step uses VolView software.

2.1.4   Resolution test

In the PA mode, the developed system is a reflection OR-PAM, whose lateral resolution is decided by laser and objective lens. If actual NA. of objective is 0.13, according to Eq. (12), the theoretical lateral resolution of system is 2.087 µm. In US mode, due to the NA. of transducer is 0.25, leading the lateral resolution is 146 µm according to Eq. (10). No matter in PA or US mode, the axial resolutions are both decided by the transducer. Considering transducer's bandwidth is 80%, axial resolution under both modes is 66 µm, which is referred to Eq. (11). However, when being focused, laser passes through the air-water and water-glass interface and the surface tissue, all of which will blur the light focusing effect, leading the lateral resolution in PA mode becomes worse. So, it is necessary to use phantom to test the actual lateral resolution. Here, a single carbon fiber was used.
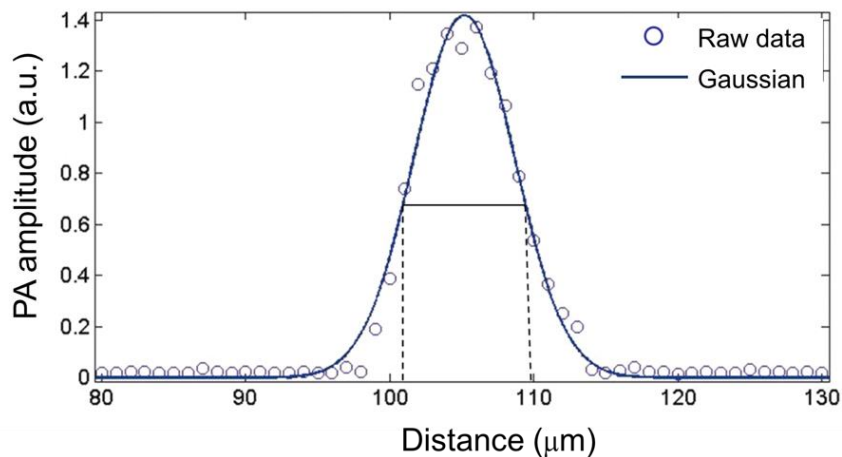
Figure 2-5 – Lateral resolution test by carbon fiber in PA mode.

Size of the carbon fiber is about 5~6 μm. Fig. 2-5 is A-line PA signal which is vertical to the carbon fiber. After doing Gaussian fitting of raw data (circles), full width at half maximum (FWHM) of fitted curve (line) is about 9 μm. Thus it is reasonable to estimate the lateral resolution of the system is under 5 μm in low scattering medium.

2.2 Fast Scanning PA/US Microscopy

2D mechanical scanning makes the acquisition speed is too low to do clinical study. This problem can be overcome by using a water-immersible MEMS scanning mirror (MEMS), which is placed on the confocal pathway of light and US, after the glass slide. However, this design will prolong the focusing length of both light and US, decreasing the lateral resolution of both PA and US mode. In order to shorten the focusing length, a two types of parabolic reflector are used in our new designs. One is transparent parabolic reflector (PR) to transmit the light and focus the US, and another one is aluminum coated parabolic mirror (PM) to focus the light and US simultaneously. The comparison of these two imaging heads is presented in section 2.2.1, in which the complementary hardware design is also described. Section 2.2.2 introduces control and acquisition program. At last, phantom test in section 2.2.3 is used to demonstrate PA imaging capability of the advanced system.

2.2.1 Hardware

With MEMS and a different translational stage, system components and trigger scheme of fast scanning PA/US microscopy are different from the mechanical scanning based PA/US microscopy.

2.2.1.1 <u>System Components</u>
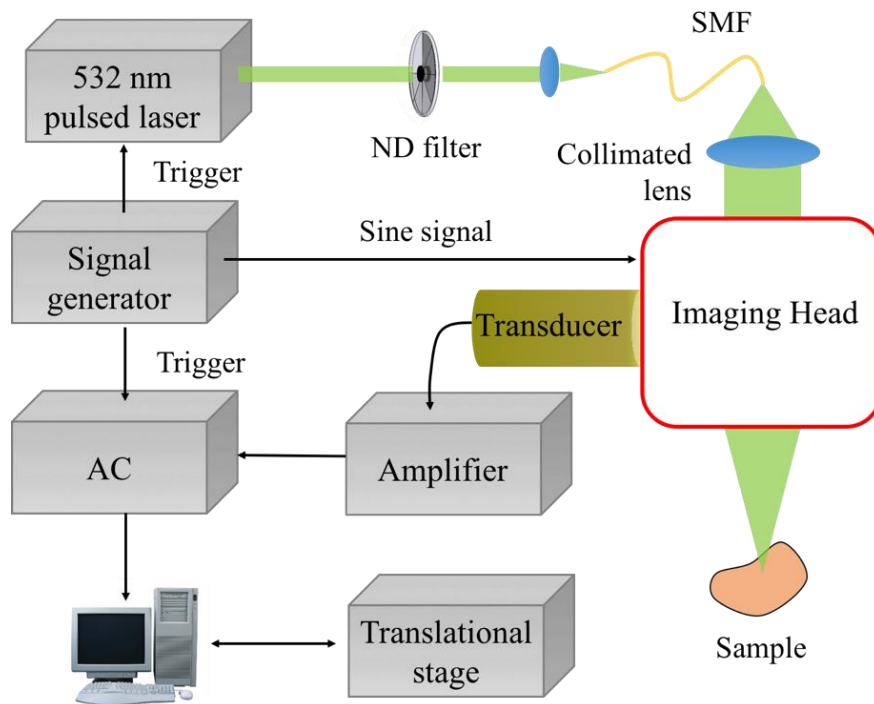
Figure 2-6 – Schema of fast scanning PA/US microscopy.

Fig. 2-6 shows the whole components of the fast scanning PA/US microscopy. Laser, acquisition card and amplifier are the same as those in the mechanical scanning based PA/US microscopy. Here we will talk about the other different parts:

1) Translational stage:

To achieve the real-time acquisition, translational stage used in this system can speed up to 10 mm s^{-1} at a high resolution 0.05 µm (CHUO SEIKI KX1040C-L). Only one axis of this stage was used to realize Y axis scanning. Meanwhile the X axis scanning was accomplished by MEMS.

2) Signal generator:

The signal generator (Tektronix AFG3102, sampling rate 1 GS/s) was used to generator a sinusoidal wave to drive the MEMS and serial square waves as the trigger of AC. The triggers only appear on the certain half period of sine wave, making the acquisition only along X axis positive direction of MEMS. The number of triggers in one period decide the number of A-lines on one B-scan. Time sequences of two signal are showed in Fig. 2-7.
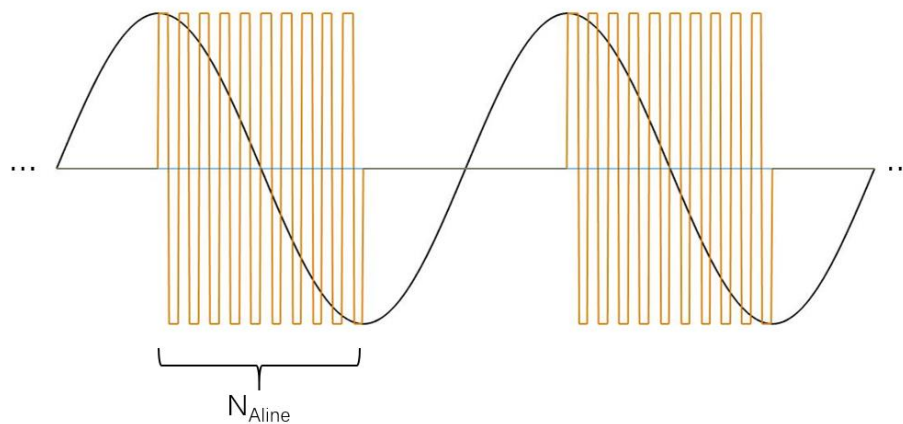
Figure 2-7 – Time sequence of signals generated by signal generator.

3) Imaging head:

The function of imaging head is to coaxially and confocally combine the illuminated light path and generated acoustic path. Two improvements are made to achieve a high imaging speed, usage of MEMS provided by Junjie Yao [51], and correspondingly new setup design. Previously, we have already know that in PA, every single pulse will give A-line signal. In order to acquire a 3D image, 2D scanning equipment is required. In the mechanical scanning based PA/US microscopy, a 2D translational stage is used. However, limited by trigger pulses' repetition rate (10 Hz), the stage moves very slow, costing long time to finish the acquisition. To overcome this drawback, a high speed translational stage and galvanometer are used in the

second PA/US system. Both of them are 1D scanning, and translational stage is in charge of Y axis, galvanometer is X axis.

Based on the MEMS, two imaging heads have been developed, both of which are collimated light passing in. One is MEMS with a transparent parabolic reflector (PR, MEMS-PR) and another is MEMS with a parabolic mirror (PM, MEMS-PM). Their designs are described in the following parts.

1.1.1.2 MEMS-PR Imaging Head
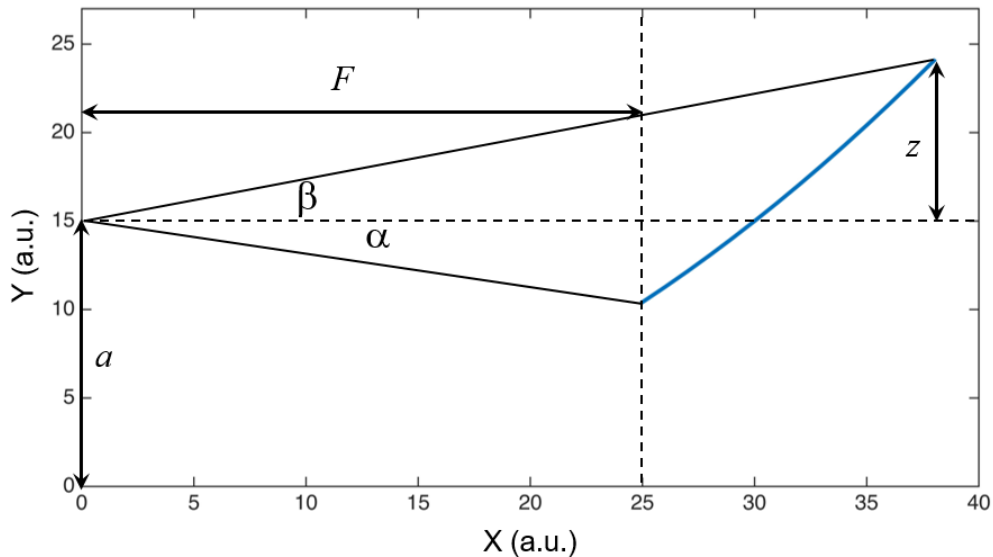
Figure 2-8 – Parabola model.

PR is used to transmit the light as well as reflect the US. Function of parabola is defined as

$$y(x, a) = \frac{x^2}{4a},$$

(18)

where a is the distance between parabola vertex and focal point. Parabola model is illustrated in Fig. 2-8. Given a set of parameters a, F, and z, where F is the working distance and z is elevation relative to the focus, NA. of this parabola can be calculated by

$$NA(a, z, F) = \sin\left(\frac{\alpha + \beta}{2}\right),$$

(19)
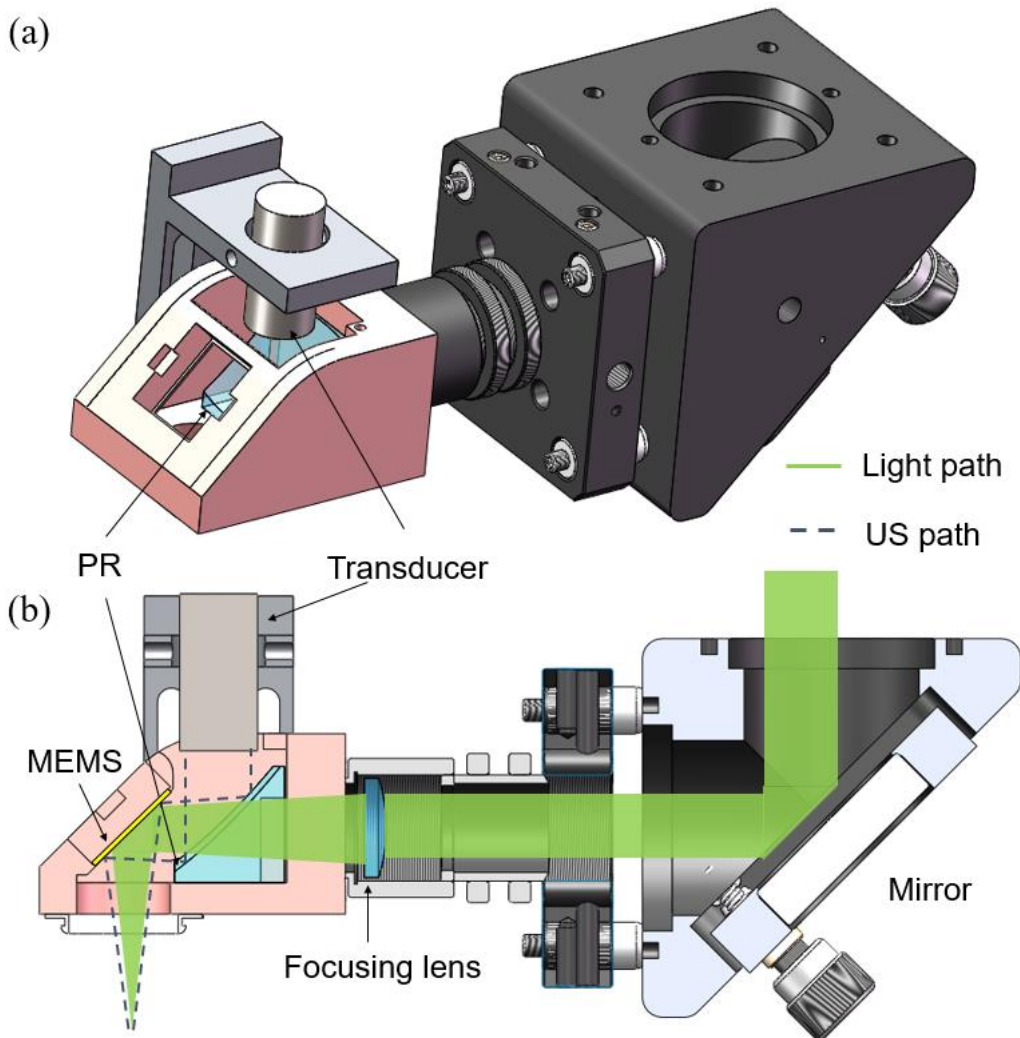
Figure 2-9 – Schema (a) and sectional view (b) of MEMS-PR imaging head.

where

$$\sin\alpha = \frac{a - F^2/4a}{a + F^2/4a}, \qquad (20)$$

and

$$\sin\beta = \frac{z}{z + 2a}. \qquad (21)$$

PR used in this imaging head was custom-built with polymethyl methacrylate (PMMA), in which a = 15 mm, F = 25 mm and z = 9mm. Thus, the NA. of PR is 0.2. To couple with the back surface with holder, the back surface and two side surfaces of PR are plane.

Fig. 2-9 shows the schematic diagram and sectional view of MEMS-PR imaging head. Collimated light going into the imaging head, was reflected by a silver coated mirror (Thorlabs, Inc.; diameter 25.4 mm), focused by a plano-convex lens (China Daheng Group, Inc.; focal length 50 mm, diameter 12.5 mm) on the sample. During the focusing path, the light passed through the PR and then was reflected by MEMS. Before being detected by a water immersed flat transducer (Olympus V317-SM; active diameter 6mm, central frequency 20 MHz), the generated acoustic signal went through two reflections, first of which was by MEMS and second was by PR.
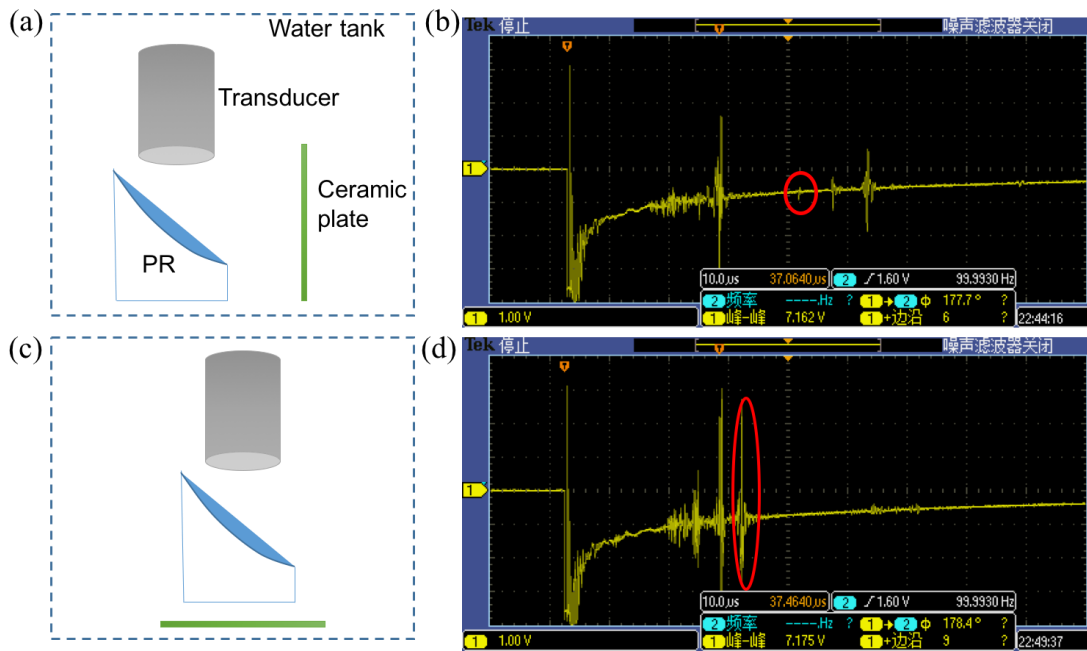
Figure 2-10 – Reflectance of PR test. (a) and (c) are schema of experiment design to test reflected and transmission US signal, respectively. (b) and (d) are their corresponding pulse-echo results.

However, some problems exist in this system. Firstly, even though the refractive index of PMMA is 1.4934 at 532 nm which is close to the refractive index of water at 532 nm 1.3337, curved surface of PR will deflect the focusing effect, leading a worse resolution. This effect can be corrected by adding the correction lens in front of the focusing lens. Secondly, in PA/US mode, the generated acoustic wave is reflected by PR according to the acoustic impedance mismatch between PR and surrounding water. However, the acoustic impedance of PR is around 3.2×10^5 Ω and water is 1.5×10^5 Ω, which have not large difference. If the acoustic wave hits the surface of PR at 45°, the intensity reflectance is around 28.9%. At such a low reflectance, large amount of acoustic energy is lost by passing through the PR. An experiment has been done to verify this theory. A flat 5 MHz water immersed transducer (Olympus V309-SU; active diameter 13 mm) was used to implement US pulse-echo. The transducer was put

perpendicularly to the PR. A hard ceramic plate was used as sample which can reflect the acoustic wave largely. Fig. 2-10 (a) and (c) illustrates the schema of the reflection and transmission test, in which the ceramic plate was put vertically on the focal plane of PR or parallel to bottom surface of PR. (b) and (d) are the results of reflection and transmission test, respectively. Compared with reflection test, the transmission signal is much larger, which is accordance with our theoretical analysis. Thus, in order to achieve a high sensitivity signal, the material of PR should be changed. Thirdly, focusing path of light is too long, leading the NA. of light in this system is 0.1 which is small. In order to conquer all of these problems, an advanced imaging head is developed.

2.2.1.2   Advanced MEMS-PM Imaging Head
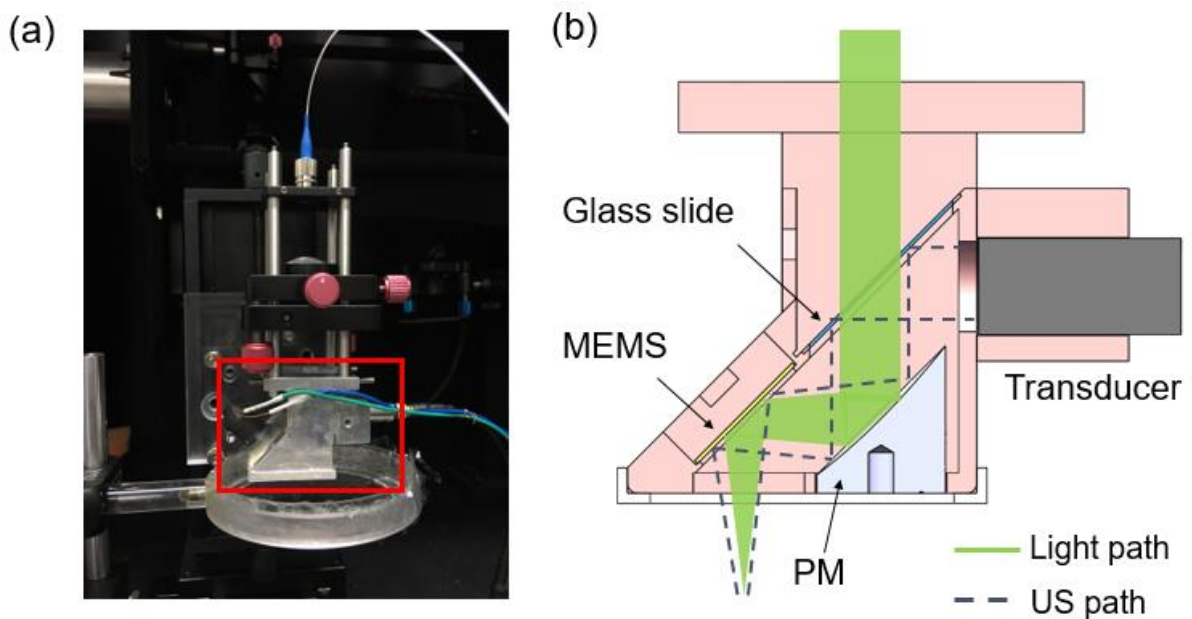
Figure 2-11 – Photo (a) and sectional view (b) of MEMS-PM imaging head.

Different with the previous design, a 90° off-axis PM (Thorlabs, Inc. MPD019-G01; reflected focal length 25.4 mm) was used to reflect and focus the light/US simultaneously. Fig.

40

2-11 shows the structure of advanced MEMS with PM (MEMS-PM) imaging head. Because the collimated light shooting into the imaging probe, there is no necessary to put any correction lens in front of the mirror. With aluminum coating, the reflectance of this PM is beyond 90%. The NA. of this PM is 0.25 with a=12.7 mm, F=19 mm, and z=7.1 mm.

Inside the imaging head, light went through two reflections, one by PM and another one by MEMS. Also the PM focused the laser onto sample. Then generated US signal went back the same way as laser, until it was reflected by glass slide after PM, and detected by transducer. MEMS rotated along X axis. So with MEMS's rotating, focusing point of laser and transducer also scanned along X axis. During the whole scanning process, light and acoustic wave were always confocal.
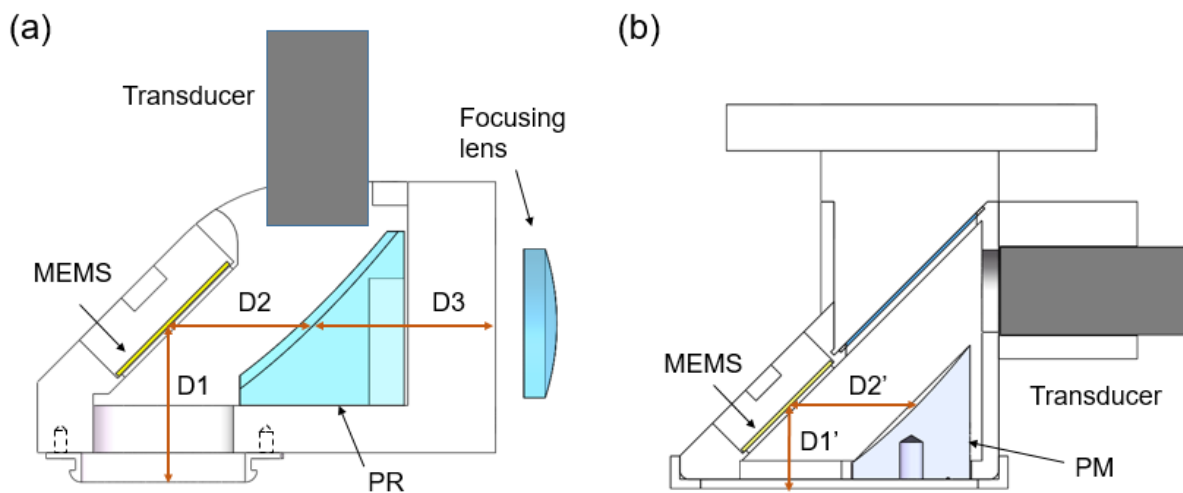
Figure 2-12 – Dimensional comparison of MEMS-PR imaging head (a) and MEMS-PM imaging head (b).

In order to look into the improved NA. of light by MEMS-PM system, Fig. 2-12 shows the dimension of two imaging heads. (a) is the sectional view of MEMS-PR, in which focused light has to go through D1 = 13.5mm, D2 = 10.8 mm and D3 = 16 mm before illuminating on

41

the sample. Due to the mechanical conjunction, all the dimensions are designed as short as possible. Thus, the light focusing length of MEMS-PR is at least 40.3 mm. While in design of MEMS-PM imaging head, because the light is focused by PM, the focusing length can be calculated start from the surface of PM, which includes D1' = 7.4 mm, and D2' = 12.2 mm. Thus the minimum focusing length of MEMS-PR is 19.6 mm, which is half of MEMS-PM system. If the radius of collimated light is the same, the NA. of MEMS-PM double increases.

2.2.2 Control and Acquisition Program
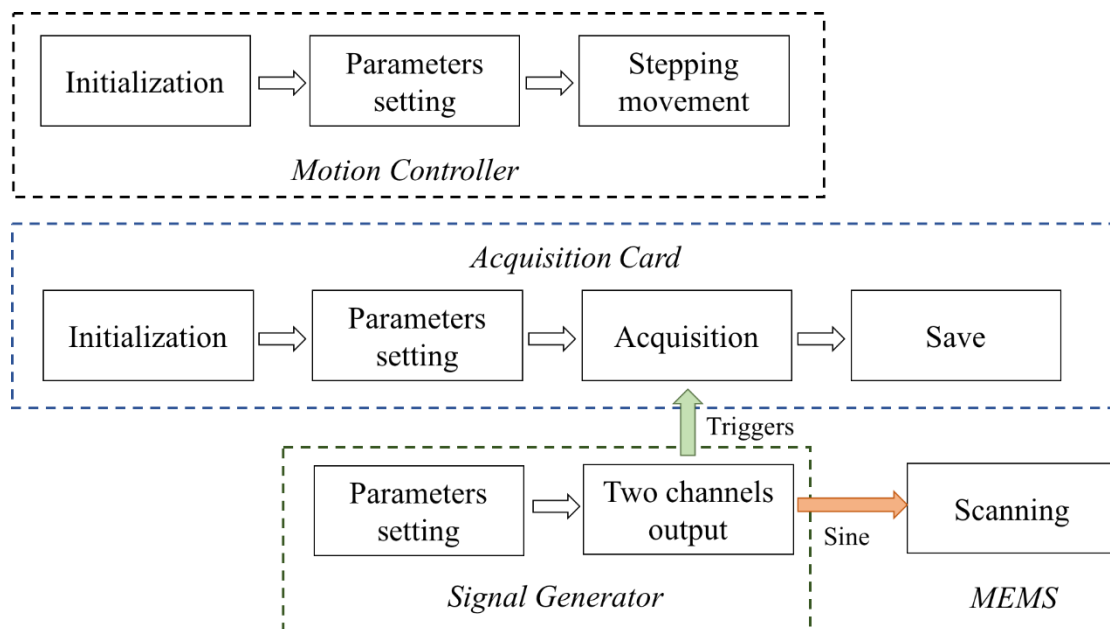
Figure 2-13 – Flow chart of control and acquisition program.

Fig. 2-13 is the flow chart of control and acquisition program. In order to fulfil a complete acquisition, motion controller, acquisition card, signal generator and MEMS are needed. Firstly, MC and AC is initialized barely at the same time. Secondly, the parameters are set, which are speed and length of movement for MC; acquisition delay, depth, line numbers and points per line for AC; frequency of sinusoidal wave and square wave, period time and

numbers per period of square wave, and their relative position for signal generator. During the acquisition, AC only be triggered during half period of sinusoidal wave, leading one direction acquisition. Then the data is save line by line, one of which is created a txt profile. Fig. 2-14 is the front window of acquisition program, which includes three parts: parameters setting, A-line window and B-scan window, by which 2D image of one-line scanning can be presented.
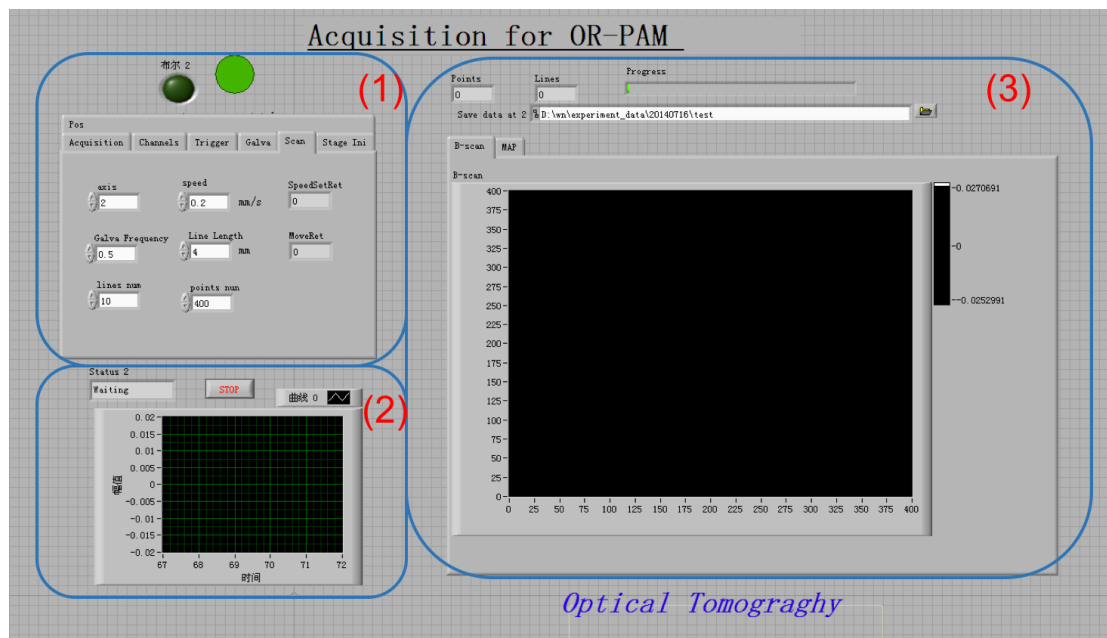
Figure 2-14 – Front window of control and acquisition program.

2.2.3   Phantom Test

To verify the imaging capability of advanced MEMS-PM microscopy, human hair was used as phantom to do PA imaging. Fig. 2-15 (b) is the phantom prototype. Both ends of human hair are stuck on a gasket, which separates the hair from bottom of water tank to avoid the signals' overlay. Due to the space blow hair is transparent, it is convenient for us to adjust

the signal, by seeing the transmission laser pattern from the bottom. Energy of light pulse is 150 nJ. X axis of the image was scanned by the MEMS, whose length was 1.2 mm. Meanwhile Y axis was scanned by the translational stage, with length = 3.4 mm, speed = 40 μm/s, leading the acquisition time was 85s. One thing needs to be mentioned is that technically acquisition time is decided by the imaging length and speed of translational stage. However, in our program, the acquisition data is saved every B-scan, which costs some time. Thus acquisition time is mainly limited by B-scan data saving time ~1s. That means if the image contains 100 B-scans, the acquisition time should be 100s. Most data reconstruction procedures were the same as that mentioned in chapter 2.1.3. Here, due to the background noise is very high, we used Gaussian filtering to denoise the PA image, with a mask of 3 x 3 pixels.
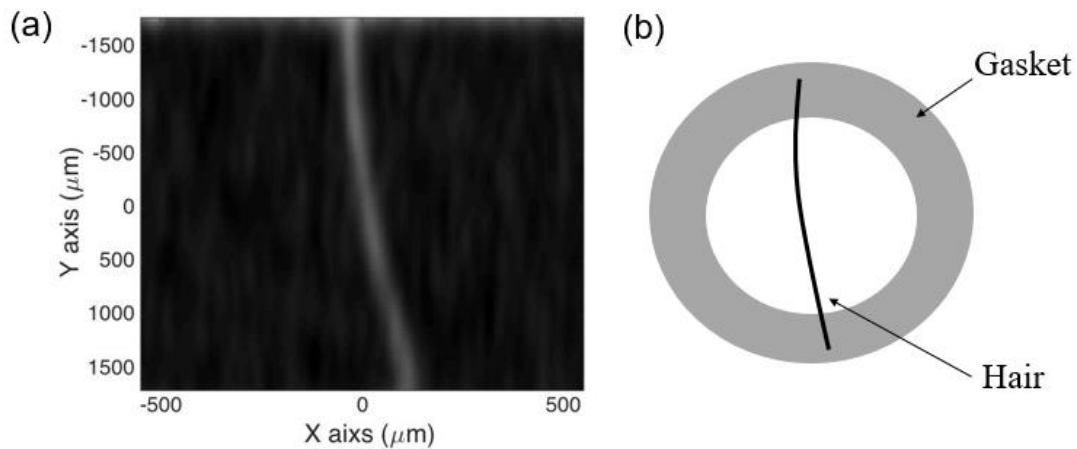
Figure 2-15 – (a) Hair PA image. (b) Phantom prototype.

2.3   Conclusion

In this chapter, we have introduced three high resolution PA/US microscopies, and each one makes some improvements based on the previous design. Although the first generation

dual-modality microscopy can reach a high lateral resolution, its scanning speed is limited by the mechanical stage and the focusing length of US is not flexible by using a focused transducer.

With a MEMS mirror, the scanning speed of our second and third generation microscopies are largely improved. Compared with variation of light pathway, changing the focusing length of US is hard to accomplished in the PAM setup. A common method is to add an acoustic lens in front of the flat transducer, inducing the loss of transducer sensitivity. This problem can be solved by our design, in which MEMS-PR PA/US microscopy can focus the US by a transparent parabolic reflector while the light is focused by a focusing lens. By this way, a flat transducer can be used to detect the US, which makes the acoustic focusing length is flexible to be changed by the design of parabolic reflector. However, during light focusing pathway, the irregular surface of PR will deflect the light which is not easy to be corrected and will increase the light focusing length.

In order to achieve a high quality and small diameter of light and US focusing spot, a parabolic mirror is used in our third generation setup MEMS-PM PA/US microscopy to focus the light and US simultaneously. Hair phantom experiment has been done to demonstrate the imaging capability of our third system.

CHAPTER 3.   APPLICATION OF PA/US MICROSCOPY SYSTEM

This chapter introduces the two applications of our developed mechanical scanning based PA/US microscopy. By imaging the microvascular system of mouse ear in section 3.1, we have demonstrated the PA imaging capability of our system. Further into the clinical application, the system has also been used to do small animal whole eye PA/US dual-modality imaging, the results of which are shown in section 3.2.

3.1   PA Mouse Ear Imaging

Due to the plane surface and distributed microcirculatory system, mouse ear is an excellent organ to test the capability of PAM imaging. Wang *et al.* (2014) used combined optical and mechanical scanning OR-PAM to image the single red blood cells in a mouse ear[52]. Zhang *et al.* (2011) used combined PAM and OCT to measure the metabolic rate of oxygen on mouse ear[53]. In this section, we also used mouse ear to test our PA mode imaging capability of mechanical scanning based PA/US microscopy.
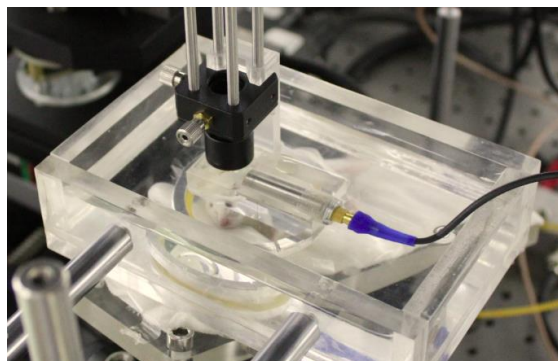
Figure 3-1 – Experimental setup of mouse ear imaging.

We used BALB/c mouse for PA imaging experiment, whose weight is about 20g. Before imaging, some procedure should be taken. First, the mouse was anesthetized by intraperitoneal injection of pentobarbital solution at 0.1 mg/g. Second, anesthetized mouse lay on the custom build mouse bed with a raised small plate beside mouse head. Third, mouse ear was stuck and tiled on the plate by ultrasonic coupling gel. Fourth, height of water tank was adjusted, making plastic membrane of its bottom slightly adhere to the mouse ear. At last, the focal plane of PA system was adjusted on the mouse ear and imaging head was scanned by 2D translational stage. After experiment was finished, mouse was exposed under infrared lamp to keep its body temperature.

Fig. 3-2 is the PA imaging result of mouse ear *in vivo*. In order to demonstrate the ultimate imaging capability of our system, FOV is the end of mouse ear. Fig. 3-2 (a) shows clearly the distribution of microcirculatory system. Zooming in the red box, detailed information of tiny blood vessel can be investigated in Fig. 3-2 (b). One of small vessel was picked in this image, and its cross-sectional PA amplitude profile is shown in Fig. 3-2 (c). The width of picked vessel is below 10 μm, which is close to the scale of blood capillary. Thus, the mouse ear image demonstrates the high resolution imaging capability of our developed microscopy.
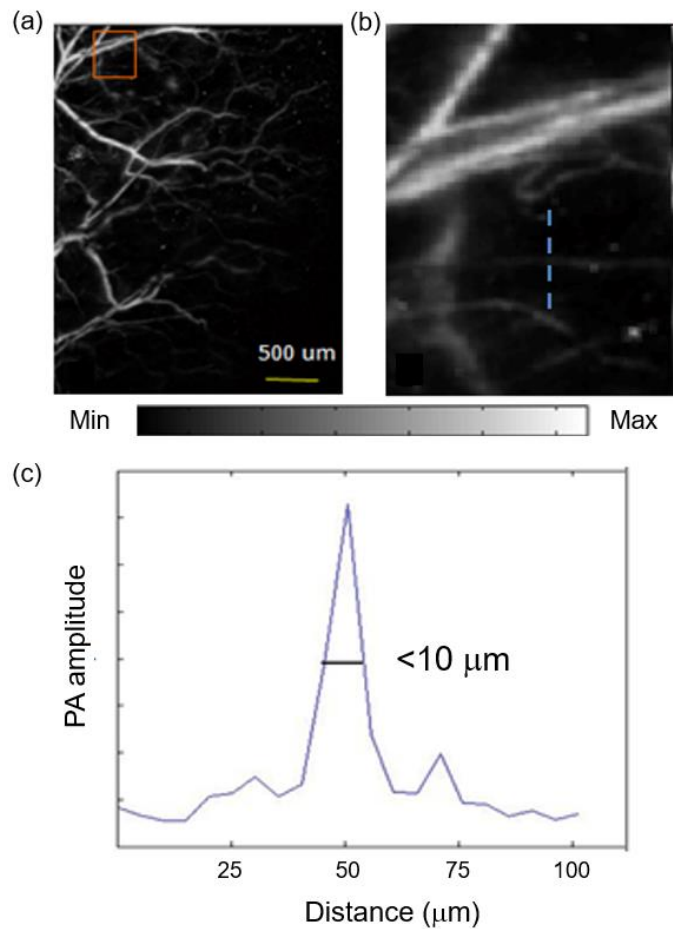
Figure 3-2 – PA mouse ear image.

3.2 Dual-modality Small Animal Whole Eye Imaging

Due to the transparency, eye is an excellent imaging organ for OR-PAM. Small animal eye provides a valuable model for studying human eye disease. In this section, structure of eye and clinical ocular disease are introduced to stress the significance of our system's application in section 3.2.1. The innovation of our system emerges by introducing other's work on PA multi-modality system in section 3.2.2. Then theoretical analysis, methods and results of dual-modality animal experiment, are described in the section 3.2.3, 3.2.4 and 3.2.5, respectively.

3.2.1   Structure of Eye and Clinical Significance

As light sensor of the human, eye plays an important role in the daily life. Fig. 3-3 shows the structure of human eye. From the surface to the bottom, light passes through the cornea, anterior chamber, pupil, crystalline lens, vitreous body, and is received by the photoreceptor cell of retina.
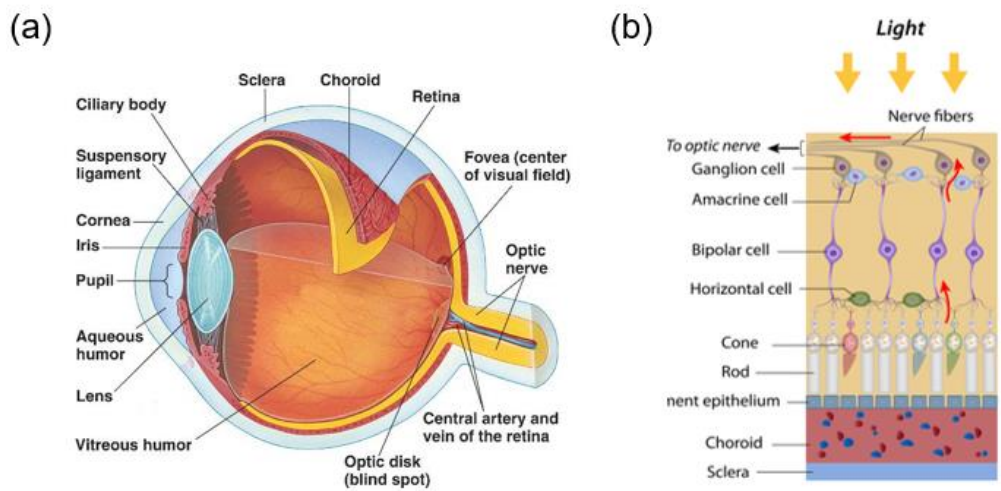
Figure 3-3 – Structure of eye. (a) whole eye structure. (b) Components of fundus and visual signal formation.

WHO Region	Total population (millions)	Blindness No. in millions (percentage)	Low vision No. in millions (percentage)	Visual Impairment No. in millions (percentage)
Afr	804.9 (11.9)	5.888 (15)	20.407 (8.3)	26.295 (9.2)
Amr	915.4 (13.6)	3.211(8)	23.401 (9.5)	26.612 (9.3)
Emr	580.2 (8.6)	4.918 (12.5)	18.581 (7.6)	23.499 (8.2)
Eur	889.2 (13.2)	2.713 (7)	25.502 (10.4)	28.215 (9.9)
Sear (India excluded)	579.1 (8.6)	3.974 (10.1)	23.938 (9.7)	27.913 (9.8)
Wpr (China excluded)	442.3 (6.6)	2.338 (6)	12.386 (5)	14.724 (5.2)
India	1181.4 (17.5)	8.075 (20.5)	54.544 (22.2)	62.619 (21.9)
China	1344.9 (20)	8.248 (20.9)	67.264 (27.3)	75.512 (26.5)
World	6737.5 (100)	39.365 (100)	246.024 (100)	285.389 (100)

Figure 3-4 – Number of people visually impaired[54].

As the fast development of industrialization, ophthalmic disease is one of the major causes which threaten our daily life. Figure 3-4 shows the data published by WHO (world health organization). Up to 2010, there was 285.3 million people suffering visual impairment over the world. Structure of eye is complicated, and dysfunction of any part will lead to ocular diseases. Major four blinding diseases all over the world are cataract, glaucoma, age-related macular degeneration (AMD), and diabetic retinopathy (DR). Apart from cataract which is induced by the structural change of lens protein, the other three diseases are closely related with the dysfunction of eye blood vessels. Glaucoma is one of incurable blinding disease, which involves optic nerve atrophy and ganglion cell death, due to the pathologic elevation of intraocular pressure. The accurate imaging of iris's metabolism and morphology of iris pigment can contribute to the diagnosis of glaucoma. AMD is the deterioration of retinal pigment epithelium (RPE), which participates in the metabolism of visual cell through providing nutrition and dissolving the dead cells, and DR is caused by the malfunction of microcirculatory system in retina. Retinal vessel SO_2 is a kind of metabolism parameter, which is direct related to the function of circulatory system. In order to achieve the early diagnosis of DR, it is a significant problem to map the structure and SO_2 of retinal vessels.

3.2.2   Research Status

Ophthalmic imaging has been playing an irreplaceable role in the treatment and diagnosis of ophthalmic disease. Current clinical ocular imaging system includes fundus photography, ultrasound, OCT, CSLO. Fundus photography, and OCT depends on the differentiation of scatter light by various tissues to form the image. OCT can reach a high axial resolution, but

it can't directly render the information of optical absorption. Based on conventional optical path of microscope, CSLO puts a pinhole in front of detector to get rid of out-focal-plane image, reaching a higher resolution than fundus photography. Due to certain ultrasonic impedance of dissimilar tissue, ocular ultrasound imaging provides the histology information of eye with deepest penetration depth among all the imaging techniques. However, ultrasound imaging can't provide the functional parameters like SO_2, and owns a low contrast. Photoacoustic tomography (PAT) is based on the optical absorption of intrinsic absorbers, signal of which is laser-induced ultrasound wave penetrating deeply in the tissue. Since the extinction coefficient of hemoglobin and melanin is much higher than the other optical absorbers under most wavelengths, the high contrast-to-noise ratio (CNR) of vessels and melanin layer can be acquired. Table 3-1 shows the comparison of current ocular imaging systems[12, 18, 55, 56].

Table 3-1 – Comparison of current ocular imaging systems

	Resolution(um)		Penetration depth	Functional information		Molecular Imaging
	lateral	Axial		Vessel velocity	Metabolism (sO_2)	
Fundus photography	10	-	-	-	-	Fluorescein sodium salt ; Indocyanine green
Ultrasound	30~300	15~150	deepest	Doppler ultrasound	-	-
OCT	3~10	2~10	<2~3mm	Doppler OCT	-	-
CSLO	5~10	20~50	<1mm	-	-	Fluorescein sodium salt ; Indocyanine green
PAOM	5 ~50	50	1~3mm	-	Multi-wavelength PAM	Gold nanoparticles; carbon nanoparticles;

In current studies of mouse eye by OR-PAM, iris and retina have been imaged separately by different setup[12, 57]. In novel ocular imaging technologies, photoacoustic ophthalmoscopy has been integrated with scanning laser ophthalmoscopy (SLO), and spectral-domain optical coherence tomography (SD-OCT)[18, 55]. Moreover, in 2010, Silverman had developed a fine resolution PAT combined with ultrasound pulse-echo, achieving to image the anterior segment and retina/choroid separately in ex vivo pig eyes[58], in which the retina/choroid image was acquired after removing the vitreous and the lens. Thus up to now, there hasn't a setup can implement the small animal whole eye high resolution PA/US imaging.

3.2.3   Theoretical Analysis of Feasibility

To image the whole eye of small animal, the complex components of eye will influence the light focusing and propagation of the generated ultrasound signal. Thus, the theoretical analysis of feasibility will be discussed from these two aspects.

3.2.3.1   Light Focusing on Retina

It is difficult for us to achieve the *in vivo* measurement and estimation the resolution of the system, which passes a series of eye structure (cornea, aqueous humor, lens, etc.). On one hand, different subject has large individual variation. On the other hand, due to the asymmetrical structural of eye, even the same subjects have different relative position of each interface in different experiments, causing the change of optical path. However, several studies about the adaptive optics theory have been performed. Our purpose is not he pursuit of high

resolution, so here we only discuss the feasibility that light focuses on the retina under the condition of our experiment device, instead of precise measurement for resolution.

The experimental animals that we used in vivo experiments are mice, which has considerable differences in internal eye structure compared with humans. Fig. 3-5 shows the eye structure of humans and mice, respectively. We find that volume ratio of lens to eye largely differs between mouse and human. In addition, the size of human eye and mice eye are also quite different. The axial length of human eye is approximately 25 mm but the axial length of mouse eye is only 3 mm. Therefore, the human eye is almost as eight times big as mouse eye. Moreover, the refractive index of human and mouse eye is also different; the human eye lens refractive index is 1.42 while the mouse eye lens refractive index is 1.5885. The internal structure of eye is a part of our whole imaging system. Therefore, it is necessary to discuss the optical properties of the mouse eye.
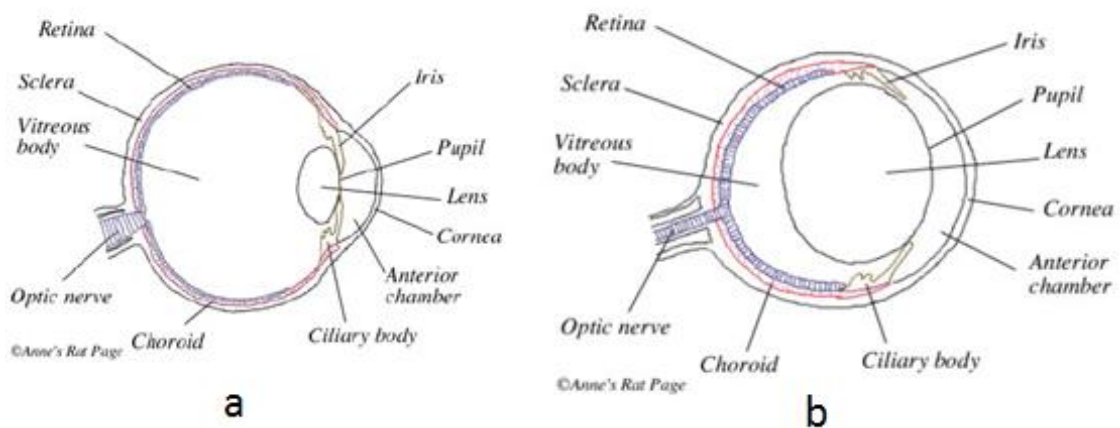
Figure 3-5 – Comparison between human eye and mouse eye. (a) Human eye; (b) Mouse eye.

Table 3-2 lists the optical properties of mouse eye, including curvature radius (mm) and refractive index. Therefore, we could build the model of mouse eye structure in the optical simulation software (OSLO). As is presented in Fig. 3-6, the structures from left to right are cornea, aqueous humor, lens, vitreous body and retina, sequentially. Parallel light from objects illuminates into the eye and finally focuses on the retina, making objects visible for the mouse.

Table 3-2 – Optical parameters of adult mouse eye components.

	Curvature radius (mm)	Thickness (mm)	Refractive index
Front cornea	1.4147	0.0074	1.4016 (cornea)
Rear cornea	1.4224	0.2467	1.3336 (aqueous humor)
Front Lens	1.1008	1.9654	1.5885 (lens)
Rear Lens	-1.1004	0.6942	1.3329 (vitreous body)
Retina	-1.5301		
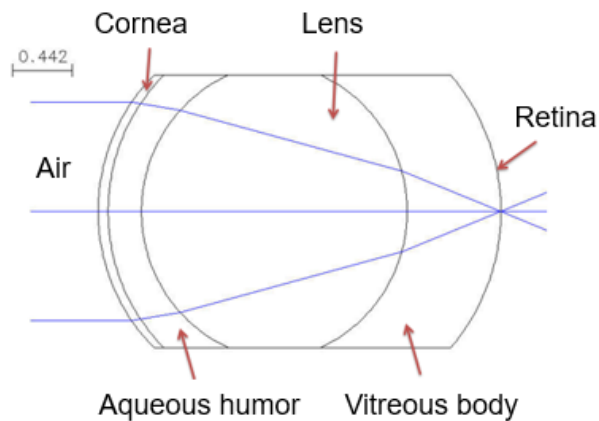
Figure 3-6 – Optical simulation of mouse eye based on OSLO (air interface).

For our imaging system, the process of light focus is different from the general ophthalmoscope and fundus OCT. When the light comes into the eye, the interface passed through is not between air and cornea, but between water and cornea, because high frequency ultrasonic detection need water as a medium. The process that parallel light goes through the

posterior of eye to the retina is shown in Fig. 3-7. As is presented, the presence of water

reduces light gathering effect in each intraocular tissues, mainly in cornea and lens, which

making the light in the retina is divergent.
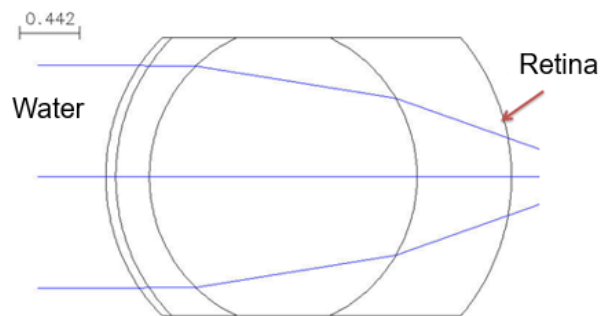
Figure 3-7 – Optical simulation of mouse eye based on OSLO (water).

In our imaging system, the function of the objective lens is to focus light on tissues that

we're observing. Fig. 3-8 showed the all of the structure that the light passes through. Light

focal plane was roughly located at the retina. The focal length of the objective lens was 25.4

mm (in air), but most of the optical path was in the water, so the actual distance was about 32

mm. Considering the thickness of the water layer was about 16 mm, the working distance of

the imaging system can reach to 16 mm, which was large enough to image the eyes of mice

and rats. But larger objective lens would be needed for imaging of human eyes.
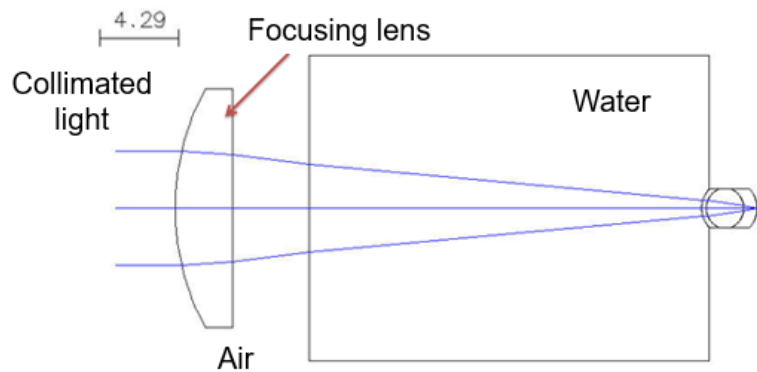
Figure 3-8 – Optical simulation of system based on OSLO.

Since the light needs to pass through the pupil firstly before entering eye, and focused beam has certain width in the pupil, the vision field is restricted by these two factors. The radius of the light passing the pupil is about 0.4 mm in theory. Therefore, we can use pharmacologically dilate the pupils to ensure the vision field to be about 2 mm x 2 mm.

3.2.3.2   Attenuation of US signal

To keep animal safety, all the experiments are taken under American National Standards Institute (ANSI)[59]. Maximum permissible exposure (MPE) for single pulse laser at 532 nm is under 5×10^{-7} J cm^{-2}. Diluted pupil of human eye is about 7 mm. Assuming SO_2 of retina vessel is 0.8, which is the normal average SO_2 level, absorption coefficient is about 231 cm^{-1} at 532 nm, leading the initial acoustic pressure generated from the retinal vessel is around 1.44×10^7 Pa. Diameter of focused light on retina is about 10 μm. From Eq. 8, the calculated maximum pressure generated from the retina vessel is 1.4 kPa. Considering the components of human and mouse eye are same, human eye parameters are used here to do the following calculation.

There are two reasons to cause attenuation effect of US signal in the eye: decay by tissues in front of retina and the reflection on the interface between different tissues. US transducer we used in the experiment is 25 MHz at central frequency. Acoustic attenuation coefficients of main absorbers on its pathway including cornea, lens and vitreous body are referred to data provided by Korte (1994)[60]. Table 3-2 provides the size of each component, thus the acoustic accumulation attenuation from retina to out surface of cornea can be calculated, which is 14.428 dB in total.

Because the acoustic impedance of eye tissue is largely different, it is necessary to discuss the reflection effect caused by the interface of different tissue. The major loss comes from the interfaces of vitreous body - lens, aqueous humor - cornea and lens - aqueous humor, former two of which obeys the principles of US propagates from liquid to solid and the last is from solid to liquid.
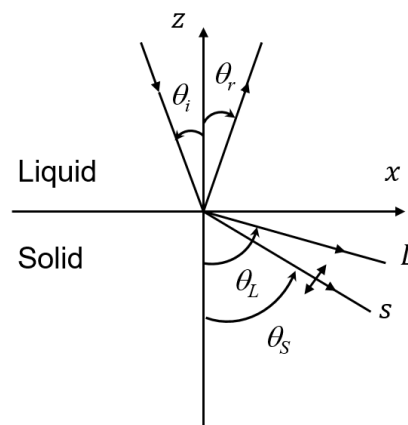
Figure 3-9 – Propagation model of US from liquid to solid.

Therefore, we only need to consider the ultrasound transmission from liquid to solid and solid back to liquid. Firstly, we discuss about the liquid to solid model. In the situation

58

of US transmitting from vitreous body to lens, the US signal generated from retina spread in

the vitreous body as the form of longitudinal wave, while the US in the lens spreads as the

form of both longitudinal and shear wave, shown in Fig. 3-9, where θ_i, θ_r, θ_l, θ_s are

incidence angle, reflection angle, longitudinal wave refraction angle and shear wave

refraction angle, respectively. Their relationship could be described by Snell's law:

$$\frac{\sin\theta_i}{V_1} = \frac{\sin\theta_r}{V_1} = \frac{\sin\theta_l}{V_L} = \frac{\sin\theta_s}{V_S}, \tag{22}$$

where, V_1, V_L, V_S are the longitudinal and share wave speed of incident and refractive medium.

T_L is defined as transmission coefficient, which can be calculated as follows:

$$T_L = \left(\frac{\rho_1}{\rho_2}\right)\frac{2Z_L cos2\theta_s}{Z_L cos^2 2\theta_s + Z_S sin^2 2\theta_s + Z_1}, \tag{23}$$

where ρ_1 and ρ_2 are the density of incident and refractive medium, respectively. Z_1, Z_L and Z_S

are the impedance of incidence, refraction longitudinal wave, and refraction shear wave, which

can be calculated as

$$Z_1 = \frac{\rho_1 V_1}{cos\theta_i}, \tag{24}$$

$$Z_L = \frac{\rho_2 V_L}{cos\theta_l}, \tag{25}$$

$$Z_S = \frac{\rho_2 V_S}{cos\theta_s}. \tag{26}$$

We hypothesize that US is vertically incident to the critical plane. Therefore, according to the

Snell's law, $\theta_i = \theta_r = \theta_l = \theta_s = 0$. Thus, Eq. 23 could be simplified as

$$T_L = \left(\frac{\rho_1}{\rho_2}\right)\frac{2Z_L}{Z_1 + Z_L}. \tag{27}$$

From the anatomic structure of lens, we could see that the ultrasound generated from micro vessel in retina pass through the lens and reached the lens capsule first. Lens capsule is a thick, transparent and elastic basilar membrane. It is surrounded by lens epithelium and lens cells. As was previously reported, the acoustic impedance of lens is $Z_L = 1.71$ x 10^6 Ω, and the density of lens is $\rho_2 = 1075.4$ kg m^{-3}. Since the density of vitreous body is $\rho_l = 1000$ kg m^{-3} and the speed of ultrasound in vitreous body is $V_l = 1500$ m s^{-1}, the acoustic impedance of vitreous body is $Z_1 = 1.5$ x 10^6 Ω. According to Eq. (27), T_L is calculated to be 0.99, which means the transmissivity of ultrasound in the critical plane between lens and vitreous body is 99%. Meanwhile, the same situation happens when US propagates from aqueous humor to cornea. The density and acoustic impedance of cornea are 1088 kg m^{-3} and 1.71 x 10^6 Ω, respectively [61]. The parameter of aqueous humor is the same as vitreous body, because major material of these two is water. Thus the acoustic amplitude transmissivity between aqueous humor and cornea is calculated to be 97%.
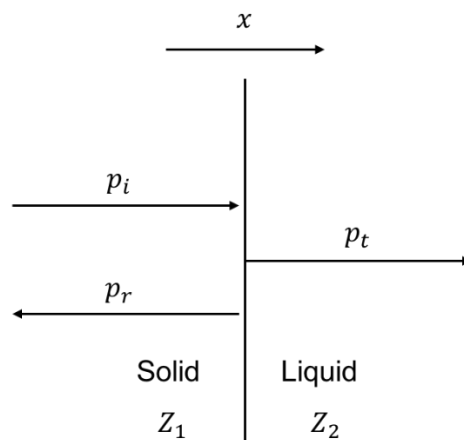
Figure 3-10 – Propagation model of US from solid to liquid.

In the next part, we discuss about the transmission of ultrasound in the critical plane between lens and aqueous humor. Since we regulate the ultrasound is vertically incident to the critical plane, the situation of reflection and transmission between lens and aqueous humor is shown in Fig. 3-10.

The transmission coefficient TP is defined as,

$$T_p = \frac{2Z_2}{Z_1 + Z_2},$$

(28)

where, Z_1 and Z_2 are acoustic impedance of incidence and transmission medium. From the above analysis, $Z_1 = 1.71 \times 10^6$ Ω and $Z_2 = 1.5 \times 10^6$ Ω. Therefore, T_p is 93%.

Thus, the total transmissivity of mouse eye is 89%. Combined with previously calculation, with pupil diluted, the maximum received pressure by transducer is 232 Pa, without considering the attenuation effect from eyelid to the surface of transducer. For commercial piezo-electric crystal transducer, the sensitivity is from several to a dozen units Pa. Thus, on theoretical consideration, the PA signal generated from retina vessel is high enough to be detected by our transducer.

3.2.4   Methods

BALB/c mouse was used for our *in vivo* experiment. We first anesthetized the animal by pentobarbital solution with the proportion of 0.1 mg/g, and then lightly covered its eye with 1 or 2 drops of saline to maintain humidity. To make sure laser pass through the iris without blocking, phenylephrine diluted in saline was used for mydriasis during eye fundus imaging.

An infrared lamp was used to keep the animal body temperature. The laser fluence was strictly controlled within the maximum permissible exposure (MPE) according to American National Standards Institute (ANSI) at 532 nm. All animal experiment obeyed protocols proved by Institutional Animal Care and Use Committee (IACUC) of Peking University. The mouse recovered to its initial living condition after experiments, and there was no observable damage due to the exposure of laser light or the methodology.

We performed the *in vivo* experiments to image anterior segment and fundus of same mouse eye through PA/US microscopy as well as ophthalmoscopy. At the beginning of each imaging session, ophthalmoscopy was used to observe the morphology of mouse iris or fundus to provide a guidance for locating the region of interest (ROI). After ROI was identified, mouse eye was firstly imaged by PAM. The A-line acquisition rate of PAM and US are 200 MHz and 100 MHz, respectively.

Laser energy is an important parameter to evaluate the safety of experiment[57, 59]. Our experiment procedures and setup configuration comply with the ANSI laser safety standards. Optical wavelength, pulse duration, exposure duration and aperture should be considered when calculating the MPE value. When imaging the anterior segment of mouse eye, light is focused on the iris, which will not do any harm to the photoreceptors or optic nerves. For retina the light is unfocused, thus skin surface exposure model should be used. Iris vessels focused by light is around 200 μm beneath the tissue surface. Considering NA. of our system is 0.13, the surface illumination diameter is 40 μm. The scanning step size is 10 μm, leading 4 repetitions. Thus the repetitive pulse limit is calculated as[62]

$$MPE_{RP} = n^{-0.25} \times MPE_{SP} = 4^{-0.25} \times 20 \text{ mJ}/cm^2 = 14.14 \text{ mJ}/cm^2. \quad (29)$$

Considering with the surface illumination area, the maximum permissible pulse energy is calculated as

$$\begin{aligned} MPE_{total} &= MPE_{RP} \times \pi \times (D/2)^2 \\ &= 14.14 \times \pi \times (20 \times 10^{-4})^2 = 178 \text{ nJ}^{\cdot} \end{aligned} \quad (30)$$

The actual energy used in our experiment is 160 nJ, which is within the safety limit. For posterior segment imaging, the laser source is treated as a small, single-pulse, whose maximum permissible values is 5 x 10^{-7} J cm^{-2}. Thus at the typical dilated human pupil of 7 mm, the maximum pulse energy is tuned to 192 nJ, according to Eq. (30). We used 500 nJ laser pulse energy for current experiment, which is 2.5 times of the MPE. Considering the SNR of image is 5.6, this means that by lowering the image quality, the PA signal above noise level can still be acquired under the laser safety.

3.2.5 Experimental Results
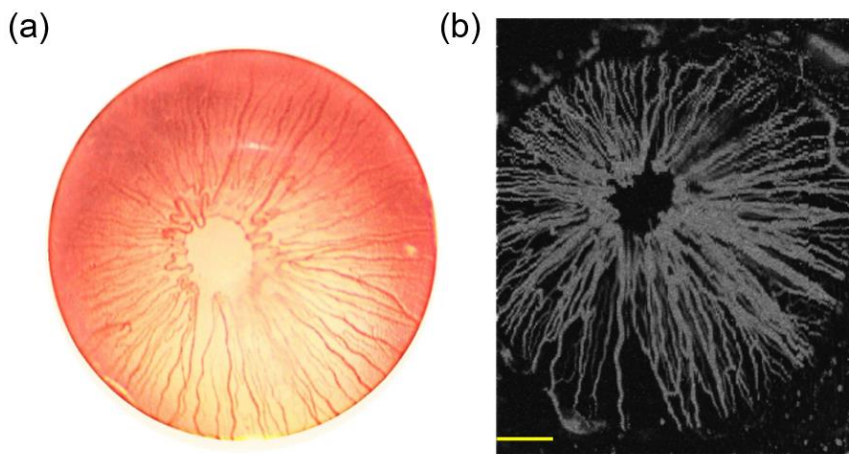
Figure 3-11 – Mouse iris images acquired by ophthalmoscopy (a) and PAM (b). Scale bar: 500 μm. [50]

Fig. 3-11 showed the mouse iris PA imaging result, as well as its counterpart by the pure optical imaging using a stereoscope (Fig. 3-11 (a)). Iris vessel is the strong chromophore in the anterior segment of eye, generating a high PA signal. Thus in PA maximal amplitude projection (MAP) image (Fig. 3-11 (b)), the distribution of iris vessels can be seen clearly. Big hole in the center of iris represents the pupil. The scanning step size was 10 μm. With 300 A-lines per B-scan and 250 B-scans of volumetric PA image, the acquisition took 10.6 minutes. The signal to noise ratio (SNR) is 18 dB without exogenous labeling or averaging.
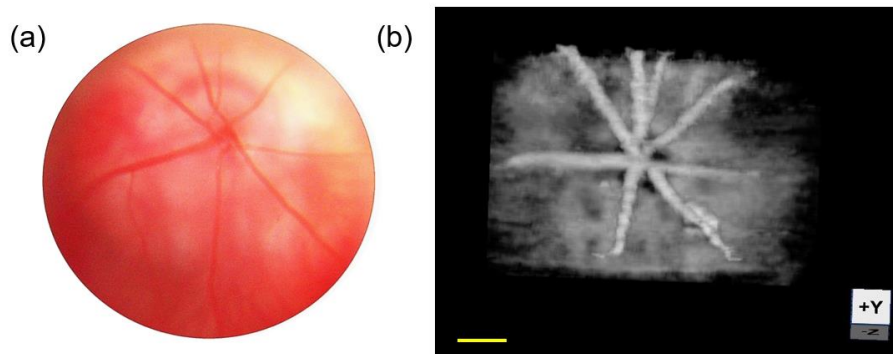
Figure 3-12 – Mouse fundus images acquired by ophthalmoscopy (a) and PAM (b). Scale bar: 500 μm. [50]

To image the ocular fundus, pupil was expanded by mydriasis, so that light could shoot on the fundus without being blocked. Fig. 3-12 (a) is the image captured by a stereoscope, showing a 2D image of retina vessels. The mouse we used in experiment is an albino type, thus main light absorbers on fundus are vessels in retina and choroid, both of which show a high PA amplitude as seen in Fig. 3-12 (b). Due to the optical deflection by lens and focal plane is on the retina layer, the blood vessels on choroid is blurred in this image. PA imaging is capable to provide volumetric image, which helps to separate different layers of fundus. All

retina vessels are merged into a hole in the center of image which indicates the optic disk. Limited by the size of dilated pupil, the FOV diameter was around 2 mm. With 10 μm step size, 300 A-lines per B-scan, and 150 B-scans, the total acquisition cost 6.5 minutes. The SNR of Fig. 3-12 (b) is 15 dB without averaging.
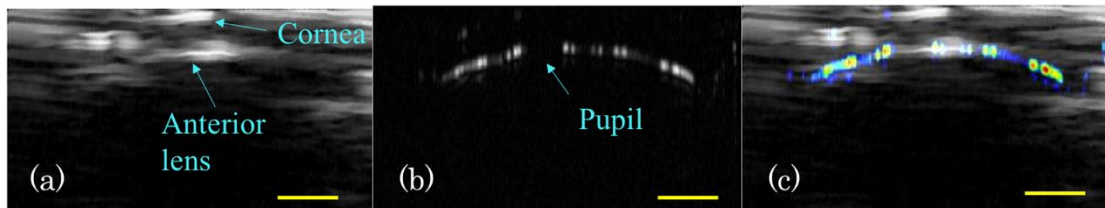
Figure 3-13 – PA/US dual-modal imaging of the anterior ocular tissue. (a) US B-scan image; (b) PA B-scan image; (c) fusion of PA and US images. Scale bar: 500μm. [50]

PA and US mode were performed sequentially to acquire co-registered PA/US image of mouse eye. Fig. 3-13 shows their individual and fusion results of anterior mouse ocular tissue. Limited by the slow scanning speed, eye movement artifact will occur during the volumetric imaging. Thus B-scans of PA/US image were performed to demonstrate the dual modality imaging capability of our developed system. Each B-scan took 2.5 s. US is based on the acoustic impedance difference of adjacent tissues to image. Thus, in US B-scan (Fig. 3-13 (a)), cornea and anterior lens surface are clearly presented. Due to the high optical absorption of hemoglobin, sectional view of single retina vessel is shown with high contrast in Fig. 3-13 (b), whose curve and position are accordance with the US image in Fig. 3-13 (c).
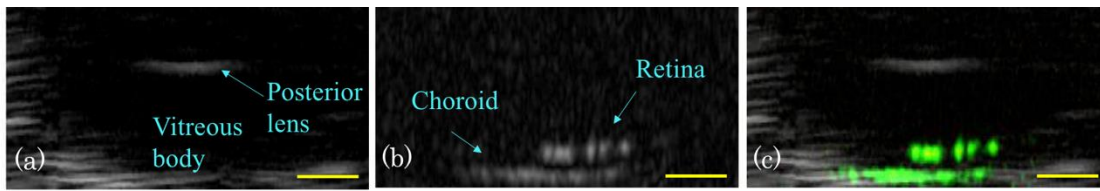
Figure 3-14 – PA/US dual-modal imaging of the fundus tissue. (a) US B-scan image; (b) PA B-scan image; (c) fusion of PA and US image. Scale bar: 500µm. [50]

Fig. 3-14 shows PA/US dual-modality imaging results of the same mouse fundus, in which (a) and (b) are B-scan images of US and PA, respectively. In US image, posterior lens surface and retina surface have strong acoustic reflection, which can be clearly seen in the Fig. 3-14 (a). Blood vessels on retina and choroid supply nutrition and exchange the matters for tissue cells, which contribute to the high absorption on PA fundus image in Fig 3-14 (b). Meanwhile, these two images have a good fusion result in Fig. 3-14(c), which provides the complementary information of the ocular tissue.

3.3 Conclusion and Discussion

In this chapter, we have demonstrated imaging ability of our developed PA/US dual-modality system by investigating the microcirculatory system on mouse ear. Concerning with the clinical ocular disease, we have successfully imaged the anterior and posterior segments of mouse eye *in vivo* with self-developed high resolution mechanical scanning based PA/US microscopy. Even though PA image of small animal retina has been reported before, it is the first time to image from iris to fundus with PA/US dual modality at optical resolution. A focused transducer was used in the experiment to focus on the same spot of light focusing. However, due to the relative small size of mouse eye, high curvature will cause the off-axial reflection loss of the acoustic wave under horizontal scanning. This is the reason why the

ultrasonic information on both sides of US image is weaker than the center part and the quality of PA imaging on the retina decreases. This effect will be improved when imaging bigger, less curvature eyes, such as eyes of human or pig.

Several improvements need to be done in the future. First, to fulfill the clinical requirement, the imaging speed should be significantly fastened to achieve the real-time acquisition. Some fast speed scanning methods have been implemented on the others' work, one of which is to use fast stage such as a voice-coil stage to substitute the slow one, and another is to use water-immersible scanning mirror to replace 2D mechanical scanning[27, 51]. With MEMS provided by Rao, the fast acquisition speed is achieved on our another self-developed MEMS-PM PA/US microscopy. Second, the SNR of this system still has some spaces to be enhanced, by using high quality low noise amplifier and putting correction lens to decrease optical aberration caused by the high tissue curvature and index mismatch along the optical pathway. Third, by adding more wavelengths, the spectroscopic PA/US system will be capable of providing the functional information, such as the oxygen saturation of blood[63]. Furthermore, this system is available to straightforwardly integrate other optical imaging modalities, like OCT and fluorescence imaging, which has already been realized by other researchers[64].

All in all, due to different mechanism, PA shows high contrast of chromophores, like blood vessel on iris, retina and choroid, while US is sensitive to the interface of different tissues, like cornea, lens, retina, and choroid, providing complementary structure information.

Our developed PA/US dual-modality system shows a great potential to investigate pathological mechanism of many ocular diseases, such as glaucoma, DR, and AMD.

CHAPTER 4.　INVESTIGATING EFFECT OF OBLIQUE DETECTION ON FUNCTIONAL PAM ACCURACY

With multi-wavelengths, spectroscopic PAM has emerged as a potential method to measure SO_2 in a quantitative, accurate and high resolution way. However, different setup designs will lead to the inaccurate result. In this chapter, we use simulation (in section 4.2 and 4.3) and phantom experiment (in section 4.4) to investigate effect of oblique detection on SO_2 measurement accuracy by functional PAM, and some guidance has been provided to achieve a high accurate SO_2 measurement.

4.1　Introduction

Based on tissue intrinsic absorption, and excluding disturbance of light scattering, spectroscopic PAM can directly measure accurate SO_2 level invasively, which has shown a strong potential in microvascular SO_2 quantitative measurement on neurology[18, 65, 66], oncology[67], ophthalmology[68, 69] and pathology[70].

Depending on relationship of pathway between incident laser and detected ultrasound, the configuration of OR-PAM can be divided into two classes: coaxial OR-PAM and off-axial OR-PAM, as shown in Fig. 4-1. In coaxial OR-PAM, illuminated laser and ultrasound wave share the same way above field of interest, and imaging speed of which is limited by the mechanical translational scanner[52, 62, 68, 71, 72]. Typical coaxial OR-PAM was developed by Song Hu *et al.*, with which they could acquire microcirculation SO_2 of mouse ear and brain and high-resolution image of mouse iris[44].

Even with the application of water-immersible scanning mirror, the scanning speed in water still cannot catch up with its galvanometer counterpart in air because of the water resistance[72]. When there is a deflection angle between illumination beam and ultrasound detection, it refers to off-axial OR-PAM[68, 69, 73, 74]. This type of system is easier to setup, and can employ the traditional fast galvanometer to scan laser beams while keeping the transducer stable. In the setup developed by Shuliang Jiao *et al.*, laser was focused on fundus vertically and transducer was coupled on eyelid, tilted from laser path[57, 64].
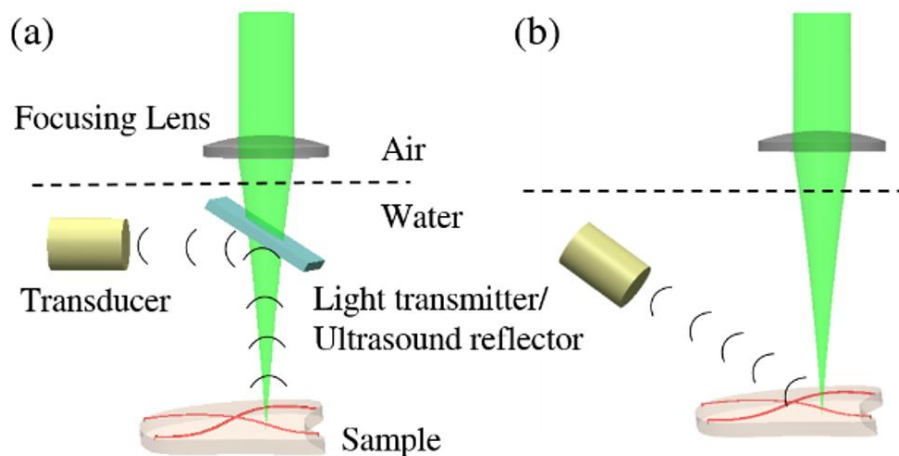
Figure 4-1 – Typical OR-PAM setups. (a) Coaxial setup. (b) Off-axial setup. Dashed line is interface of air and water. Arcs are the ultrasonic waves detected by transducer.[75]

4.2   Simulation Modeling
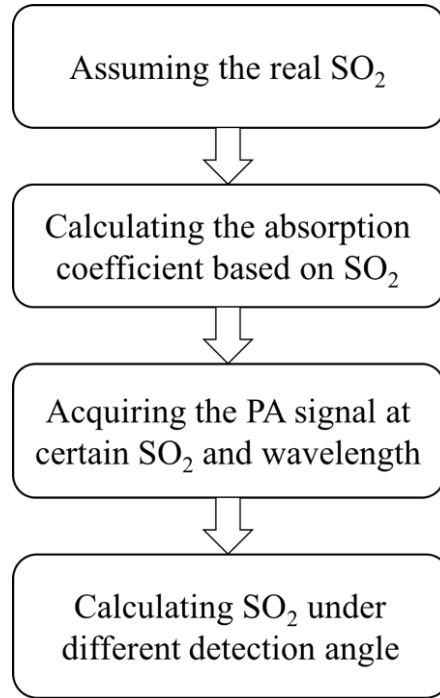
Figure 4-2 – Simulation flow of SO₂ measurement.

Fig. 4-2 gives the simulation flow, which includes four steps, which will be talked about one by one. First, actual SO₂ of blood vessel was to be settled, varying from 0.6 -0.9, considering the real SO₂ of vein and artery. Second, in single blood vessel imaging, the absorption coefficients of vessel are influenced by both wavelength (λ) and SO₂, which is defined as follows,

$$
\begin{aligned}
\mu_a(\lambda, \mathbf{r}) &= 2.303 \times \left[\varepsilon_{Hb}(\lambda)[Hb](\mathbf{r}) + \varepsilon_{HbO_2}(\lambda)[HbO_2](\mathbf{r})\right] \\
&= 2.303([Hb] + [HbO_2])(\mathbf{r}) \times \left[\varepsilon_{Hb}(\lambda)\left(1 - SO_2(\mathbf{r})\right) + \cdots \right. \\
&\quad \left. \varepsilon_{HbO_2}(\lambda)SO_2(\mathbf{r})\right],
\end{aligned}
\tag{31}
$$
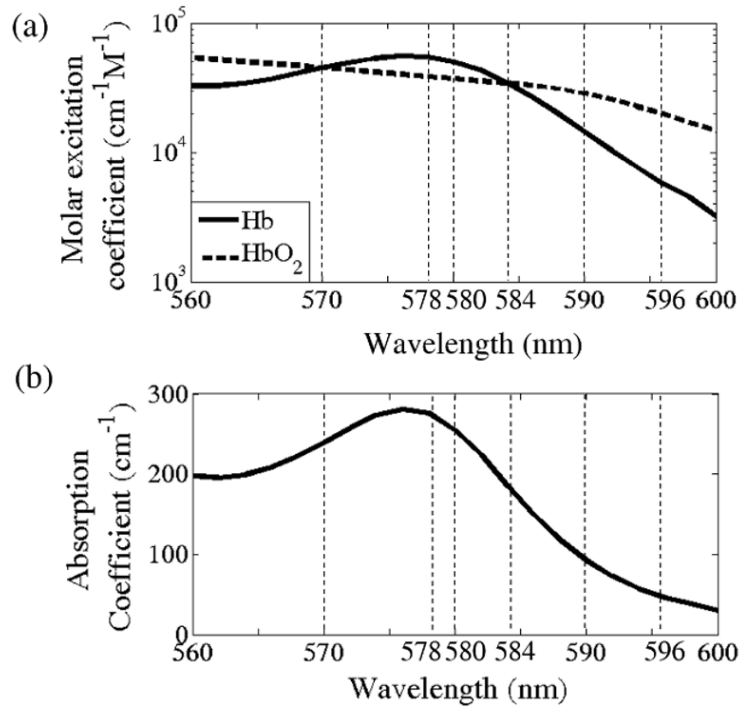
Figure 4-3 – (a) Molar excitation coefficient of HbO₂ and Hb from 560nm to 600nm; (b) Absorption coefficient of blood vessel at SO₂=0.8. Dashed lines are the wavelengths chosen in this simulation.[75]

where $\varepsilon_{Hb}(\lambda)$, $\varepsilon_{HbO_2}(\lambda)$ are their molar extinction coefficients (cm⁻¹M⁻¹) at wavelength λ, which are shown in Fig. 4-3 (a). The blood optical absorption spectra is calculated at a typical total hemoglobin concentration ([Hb] + [HbO2] = 2.33×10^{-3} mol $\cdot L^{-1}$) and SO₂ (= 80%), which is also shown in Fig. 4-3 (b).

Previously, many wavelength combinations have been used in other's work to measure SO₂, of which 8 common wavelength groups were to be investigated here. Fig. 4-3 (a) (dashed lines) shows the extinction coefficients of the chosen wavelength groups, which are (560 nm, 570 nm), (570 nm, 580 nm), (570 nm, 590 nm), (570 nm, 600 nm), (570 nm, 578 nm), (578 nm, 584 nm), (584 nm, 590 nm), and (584 nm, 596 nm).

In the numerical simulation study, light and vessel were simplified as cylinder, diameter of which were 20 μm and 100 μm, respectively. Fig. 4-4 (a) shows the schema of a light beam (green color) perpendicularly illuminating on a vessel (red color) and the oblique ultrasonic detection. Light is attenuated inside the vessel along penetration depth, according to Lambert-beer law. In the center of the vessel, the Cartesian coordinate system was set, in which θ, φ were the polar angle and the azimuthal angle, respectively. The distance from center of Cartesian coordinate system to the surface of transducer was 25.4mm.
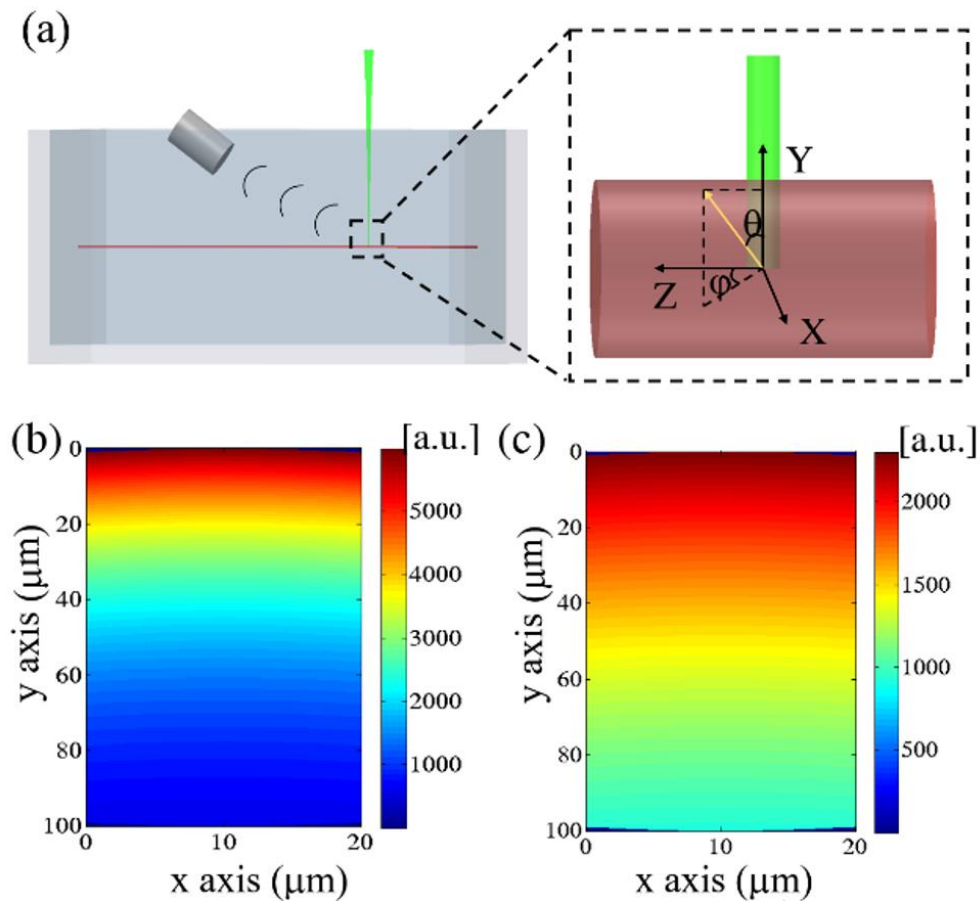
Figure 4-4 – Model schema and heat deposition distribution in the vessel. (a) left, simulation model of off-axial OR-PAM (detection angle is expressed by coordinate), right is Zoom-in of dashed black square, the yellow arrow pointing to the transducer; (b) x-y cross-section of heat deposition at 570 nm; (c) at 590 nm.[75]

For instacne, Fig. 4-4 (b) (c) gives the cross-section of heat distribution at 570 nm and 590 nm for $SO_2 = 80\%$. Due to the large difference in their absorption coefficients (μ_a (570 nm) = 238.9 cm^{-1}, μ_a (590 nm) = 92 cm^{-1}), the deposition pattern shows significant differences. The smaller absorption, the longer penetration depth. The distribution pattern of same fluence is not a straight line due to the curve of blood vessel's cylinder shape.

Then, the PA signal could be calculated according to Eq. (9), by setting mesh grids (0.1 μm x 0.1 μm, delta = 0.1 μm), and the distance between each integrated arc was 8 deltas. Fig. 4-5 shows an instance of PA signal acquired at 584 nm wavelength, certain SO_2 (= 0.95) and deflection angle ($\theta = 30^o, \phi = 0$). The calculated peak amplitude of PA signal is used to quantify SO_2 [76, 77].
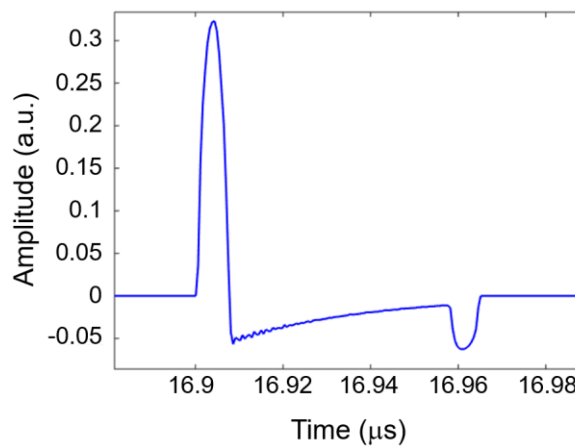
Figure 4-5 – PA signal at 584nm, $SO_2 = 0.95$, $\theta = 30^o, \phi = 0$.

Since the amplitude of PA signal is proportional to the initial pressure that is related to hemoglobin concentration, molar concentrations of [Hb] and [HbO$_2$] in blood vessel can be calculated using multi-wavelength measurements, referred Eq. (13). To

simplify, we used two wavelengths in the simulation, so Eq. (16) and Eq. (17) can be written like,

$$M = \begin{bmatrix} \varepsilon_{Hb}(\lambda_1) & \varepsilon_{HbO_2}(\lambda_1) \\ \varepsilon_{Hb}(\lambda_2) & \varepsilon_{HbO_2}(\lambda_2) \end{bmatrix}, \tag{32}$$

$$K(r) = \begin{bmatrix} A(\lambda_1, \mathbf{r})/F(\lambda_1, \mathbf{r}) \\ A(\lambda_2, \mathbf{r})/F(\lambda_2, \mathbf{r}) \end{bmatrix}. \tag{33}$$

Assuming local fluence is the same under different wavelengths, SO_2 calculation can be written as follows,

$$\begin{aligned} SO_2 &= \frac{[HbO_2]}{[Hb] + [HbO_2]} \\ &= \frac{p(\lambda_2)\varepsilon_{Hb}(\lambda_1) - p(\lambda_1)\varepsilon_{Hb}(\lambda_2)}{p(\lambda_1)\big[\varepsilon_{HbO_2}(\lambda_2) - \varepsilon_{Hb}(\lambda_2)\big] - p(\lambda_2)\big[\varepsilon_{HbO_2}(\lambda_1) - \varepsilon_{Hb}(\lambda_1)\big]}. \end{aligned} \tag{34}$$

Commonly, ratios of absorption coefficients are substituted by their corresponding ratios of maximum amplitude of PA signal at multiple wavelengths in the calculation of SO_2. Choosing one wavelength (assuming to be λ_2) as isotropic (570 nm and 584 nm), at which extinction coefficients of oxygen hemoglobin and deoxygen hemoglobin are the same, the oxygen saturation can be further simplified as,

$$SO_2 = \frac{\varepsilon_{Hb}(\lambda_2)}{\varepsilon_{HbO_2}(\lambda_1) - \varepsilon_{Hb}(\lambda_1)} \cdot \frac{p(\lambda_1)}{p(\lambda_2)} + \frac{\varepsilon_{Hb}(\lambda_1)}{\varepsilon_{HbO_2}(\lambda_1) - \varepsilon_{Hb}(\lambda_1)}, \tag{35}$$

where $p(\lambda_1)$ and $p(\lambda_2)$ represent the maximum amplitudes of PA signal at these two wavelengths, respectively. In off-axial OR-PAM, the calculated SO_2 will be inaccurate

if the ratio of two PA values deviates from the ratio of absorption coefficient (μ_a (λ_1) /μ_a (λ_2)). To investigate the accuracy of the measured SO$_2$, define the relative SO$_2$ deviation (δSO$_2$) as,

$$\delta SO_2 = \frac{SO_2 - \widetilde{SO}_2}{SO_2} \times 100\%, \qquad (36)$$

where SO$_2$ and $\widetilde{SO}_2$ represent the actual and calculated oxygen saturation, respectively.

In the realistic situation, PA signal is also restricted by ultrasound detector, which is characterized by the bandwidth-limited impulse response function h(t)[50],

$$h(t) = A t^{-3} \cos(2\pi f_0 t)\, e^{-K f_0 t}, \qquad (37)$$

where A is a constant (10^{-7} here), f_0 is the central frequency of transducer varying from 10 MHz to 130 MHz. Frequency bandwidth of detector was 80% with the definition K=3.833. When the influence of detector central frequency was investigated, PA signal was the convolution of primary PA signal and h(t).

Different wavelength induces different heat distribution pattern. Under small θ cases, this difference will not affect the ratio of maximum PA signals which is the same as the ratio of their corresponding absorption coefficients. However, when the polar angle becomes larger, large errors in calculating SO$_2$ will occur, because the difference could cause the PA ratio to deviate from the ratio of absorption coefficients. To investigate the effect of deflection angle, our numerical simulation study includes the following three cases:

i.   Influence of (θ, φ) and wavelength combinations on SO$_2$ deviation;

ii.   Influence of absolute SO$_2$ values on the δSO$_2$ at a certain titled angle;

iii. Influence of transducer central frequency on SO$_2$ deviation at certain tilted angle.

4.3   Simulation Results

4.3.1   SO$_2$ deviation varies with angles
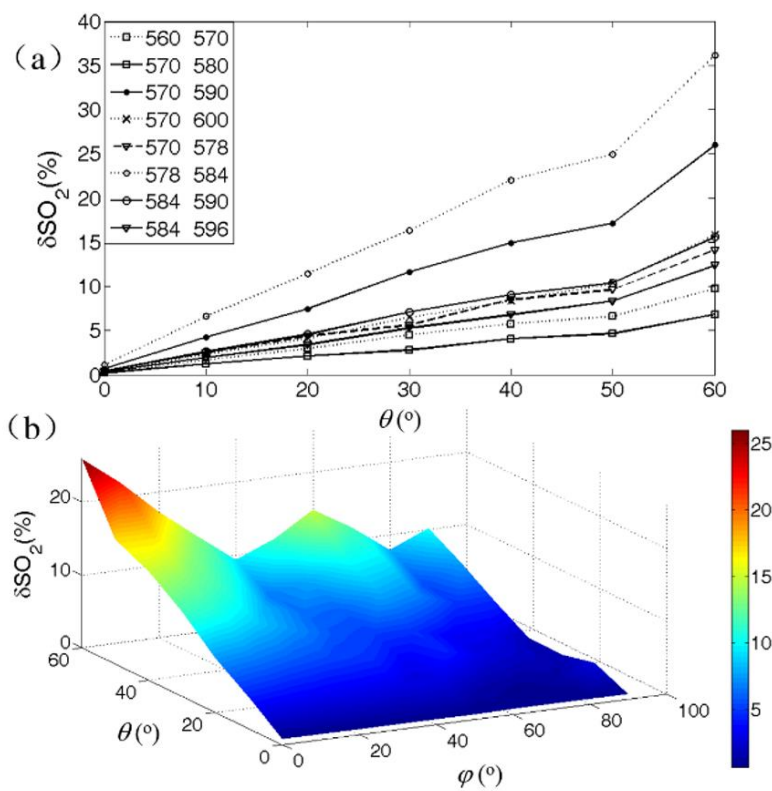
Figure 4-6 – Influence of detection angels on SO$_2$ deviation. (a) Calculate SO$_2$ deviation varies with θ under different wavelength groups (SO$_2$ = 80%, φ = 0). (b) Influence of both polar and azimuthal angles on SO$_2$ deviation under (570 nm, 590 nm) (SO$_2$ = 80%).[75]

Fig. 4-6 (a) shows the tendency of SO$_2$ deviation varies with θ under different wavelength groups at certain constant φ and SO$_2$ (φ = 0, SO$_2$ = 80%). For each wavelength group, SO$_2$ deviation increases with θ increases, but the amount is different.

The maximum deviation group is (578 nm, 584 nm), and the minimum is (570 nm, 580 nm).

Besides the influence of θ, both angular parameters were investigated for SO_2 deviation. At certain SO_2 (= 80%) and wavelength group (570 nm, 590 nm), SO_2 deviation tendency changes with (θ, φ) is shown in Fig. 4-6 (b). Compared with the polar angle, the azimuthal angle plays a less important role in the deviation of the SO_2.

4.3.2 SO_2 deviation varies with actual SO_2.
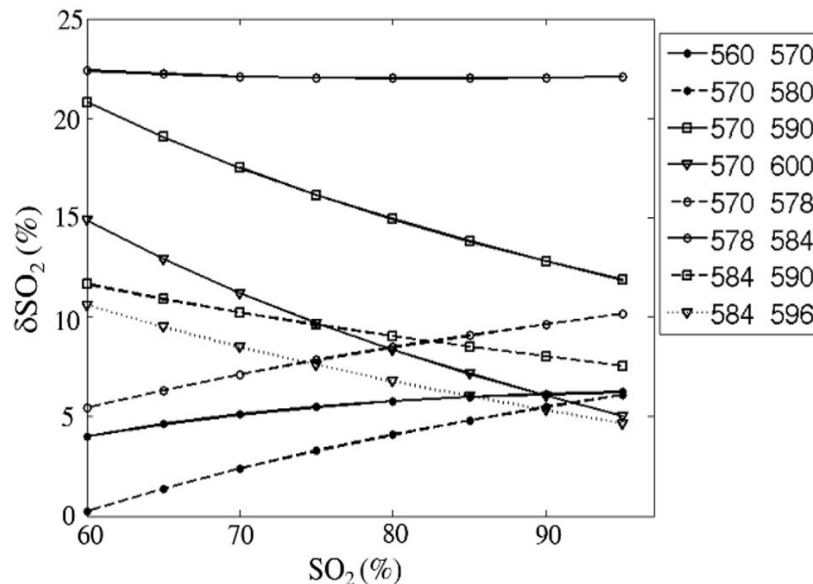
Figure 4-7 – Influence of SO_2 on SO_2 deviation under different wavelength group and certain detection angle ($\theta = 40°$, $\varphi = 0°$).[75]

The actual SO_2 values also has an effect on the measurement accuracy, which was investigated at a given tilted detection angle ($\theta = 40°$, $\varphi = 0°$). According to real oxygen saturation of vein and artery, we varied SO_2 values from 60% to 95%, and the corresponding deviation values are shown in Fig. 4-7. The trend can be totally divided into three patterns. One is remaining constant as SO_2 changes, which is (578 nm, 584

78

nm) and this group always has highest SO_2 deviation. The second pattern is SO_2 deviations has negative relationship with SO_2, which are (570 nm, 590 nm), (570 nm, 600 nm), (584 nm, 590 nm) and (584 nm, 596 nm). The last pattern shows positive relationship between SO_2 deviation and actual SO_2 values, like (570 nm, 578 nm), (560 nm, 570 nm) and (570 nm, 580 nm). Thus, we can derive some recommendations. To image vein, (570 nm, 580 nm) is the best choice among the 8 wavelength groups, which owns lowest SO_2 deviation (less than 5%). To image the artery dominant area (SO_2 is around 95%), (584 nm, 596 nm) is preferred, because at this condition, the SO_2 deviation is about 5%, which is acceptable.

4.3.3 SO_2 deviation varies with transducer frequency.
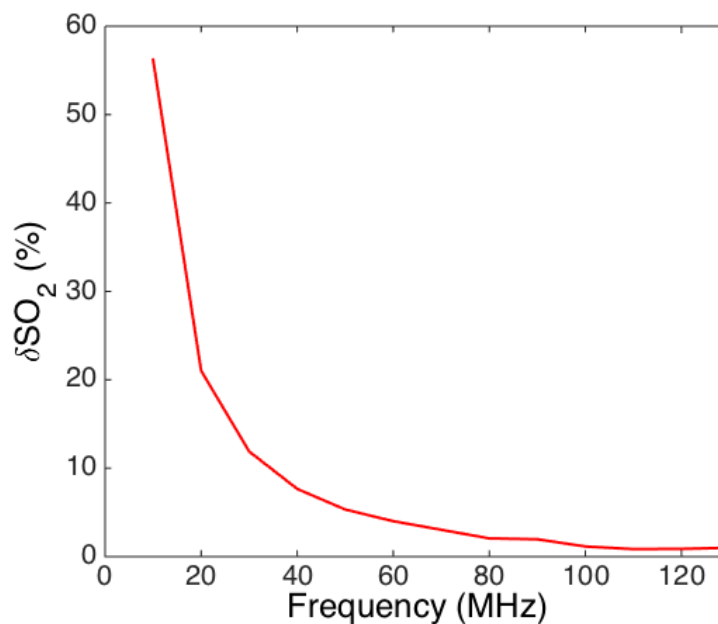
Figure 4-8 – Influence of central frequency of ultrasonic transducer to SO_2 measurement ((578nm, 584nm), SO_2=0.95, θ=30º, φ=0º).

In our model, the diameter of blood vessel is greater than the penetration depth, under which circumstance, difference of local fluence in the vessel can't be ignored. However, in PAM the accurate quantitation of SO_2 can be achieved by using suitable ultrasonic transducer, the central wavelength of which should be shorter than the light penetration depth in the blood[76]. Fig. 4-8 demonstrated SO_2 deviation decreases as the central wavelength of ultrasonic transducer increases within 10-130MHz central frequency range at (578nm, 584nm) and $SO_2 = 0.95$. Here, the maximum absolute value of Hilbert transform of bandwidth-responsive PA signal is used to calculate SO_2 deviation, because Hilbert transform can select the edge of signal which is preferred after ultrasonic transducer's convolution[78]. Because the central wavelength of original PA signal is about 50MHz, effect of transducer, central wavelength of which is above 130MHz, disappears.

4.4 Phantom Experiment and Results

4.4.1 Phantom Experiment
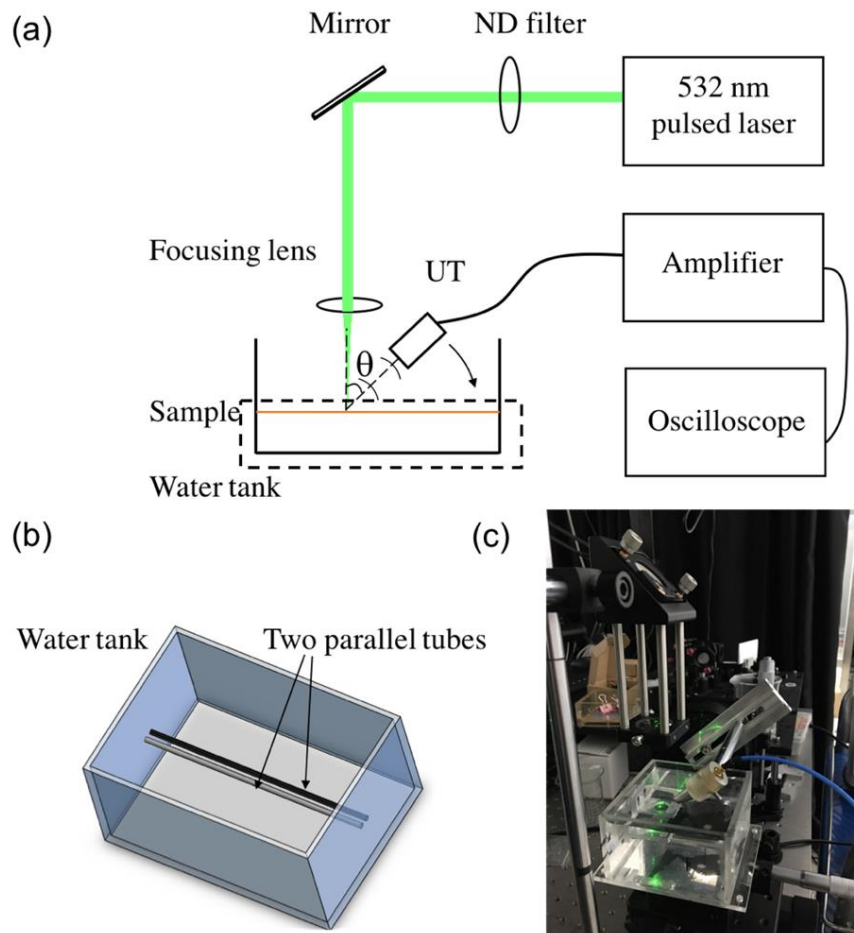
Figure 4-9 – Setup of phantom experiment. (a) Schematic diagram. (b) Detailed position of dashed box in (a). (c) Photo of setup. θ **is the angle between centerline of UT and light.**[75]

To validate our simulation results, phantom experiment was done at wavelength group (570 nm, 590 nm) to mimic the actual SO_2 measurement. The schema of our experimental setup is shown in Fig. 4-9 (a), in which the 532 nm laser source and Olympus preamplifier are the same as in Chapter 2. The pulsed 532 nm irradiation is vertically focused on a small plastic tube (CTPC167-200-5, Paradigm Optics) with inner diameter of 167 μm. The focused spot is around 20 μm, which is comparable with simulation. An unfocused water-immersed transducer (Olympus V317-SU; nominal element size 6mm, center frequency 20MHz) was fixed on a rotating stage,

guaranteeing the transducer rotates around the intersection of light focused area and sample. The signal was amplified 58 dB and recorded by Oscilloscope (Tektronix DPO3034) at the sampling rate 250 MS/s and 256 times average.

Instead of two wavelengths illumination, two diluted Indian ink solutions were used as sample whose absorption coefficients at 532 nm are the same as blood ($SO_2 =$ 80%) optical absorption coefficients at 570 nm and 590 nm, respectively, which was injected into two polycarbonate tubes with 200 μm outer diameter and 167 μm inner diameter. As Fig. 4-9 (b) shows, two tubes were parallelly and closely aligned in the water tank. Three θ values, 30, 40, 50 degrees and $\varphi = 0$, were used in our experiment, at each of which, the averaged PA signal was collected at multiple times, to do statistical analysis later.

4.4.2   Phantom Results
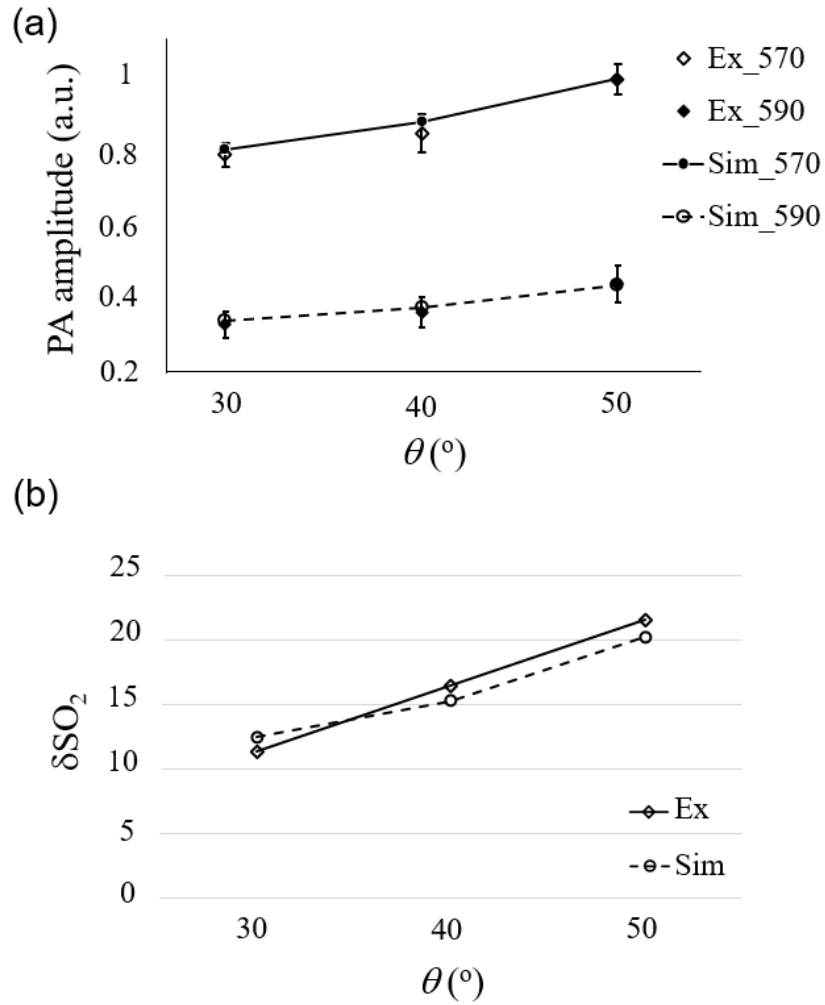
Figure 4-10 – PA signal (a) and SO$_2$ deviation (b) comparison of statistical analysis of experimental and simulation results under (570 nm, 590 nm) with θ=30º, 40º, 50º. Ex, experiment; Sim, simulation.[75]

Table 4-1 – PA data acquired at 570 nm and 590 nm.

	Angle	Sample Size	Before_normalization	After_nomalization
	30	15	0.0222±0.00081	0.7929±0.02908
Ex_570	40	10	0.0238±0.00141	0.8506±0.05044
	50	18	0.0280±0.00096	1.0000±0.03422
	30	16	0.0092±0.001	0.3275±0.03602
Ex_590	40	21	0.0101±0.00116	0.3619±0.04174
	50	16	0.0123±0.00136	0.4380±0.04859

Fig. 4-10 (a) shows the PA signal comparison of statistical analysis of experimental and simulation results under (570 nm, 590 nm) with θ=30º, 40º, 50º, in

which rhombus represent mean value and error bar stands for standard deviation. To be comparable, data was normalized on basis of highest mean value (under 50°) of simulation and experimental group, respectively. And the raw data before and after the normalization are listed in Table 4-1. Meanwhile, one sample t test was used to demonstrate there is no significant difference (P>0.05) between these two group, suggesting our simulation is in consistence with the experimental results. Then SO_2 deviation of experimental results can be calculated, the comparison of which with simulation result is shown in Fig. 4-10 (b). Since the transducer used in phantom experiment has a limited bandwidth centered at 20 MHz, we also applied a convolution of the simulated PA signal with an impulse response function [16]. From the comparison, the error in SO_2 measurement (δSO_2) increases with the polar angle, which is in good consistence with the simulated results.

4.5 Conclusion and Discussion

In conclusion, by looking into the SO_2 measurement inaccuracy of off-axial PAM setup with simulation and phantom experiment, some valuable results have been acquired to guide the measurement and setup design of functional off-axial OR-PAM. Our results find that detection angle has a great impact on the quantitative measurement of hemoglobin oxygen saturation in off-axial OR-PAM, especially when the deflection angle gets larger. SO_2 deviation increases with θ increases. The chosen wavelength groups are also factors, which should be payed attention to. From theoretical analysis, large differences of heat deposition pattern at different wavelengths is the main reason

to cause SO_2 deviation, which couldn't be neglected when the vessel diameter is larger than the $1/\mu_a$. However, our study only provides simulation analysis, further analytical analysis should be done in the future.

Substituting Eq. 35 into Eq. 36, δSO_2 can be further derived:

$$\delta SO_2(\theta, \lambda_{i1}, \lambda_{i2}) = \frac{S - \dfrac{p(\theta, \lambda_{i1})}{p(\theta, \lambda_{i2})}}{S - T}, \tag{38}$$

where i is the group number of wavelengths, $S = \mu_a(\lambda_{i1})/\mu_a(\lambda_{i2})$ and $T = \varepsilon_{Hb}(\lambda_{i1})/\varepsilon_{Hb}(\lambda_{i2})$. Under certain wavelength group and SO_2, parameters S and T are constants. Thus, inaccuracy in oxygen saturation measurements is caused by the deviation in the ratio of PA values. Fig. 4-11 gives the tendency of PA amplitude ratio (p (θ, 590 nm)/ p (θ, 570 nm)) with θ variations, at Here, the wavelength combination (570 nm, 590 nm). And the ratio shows positive correlation curves, changing 0.385 to 0.45 as the polar angle increases from 0 to 60 degrees, while $S - T = -0.24$. With increasing deflection of PA amplitude ratio to 0 degree, the SO_2 deviation error occurs.
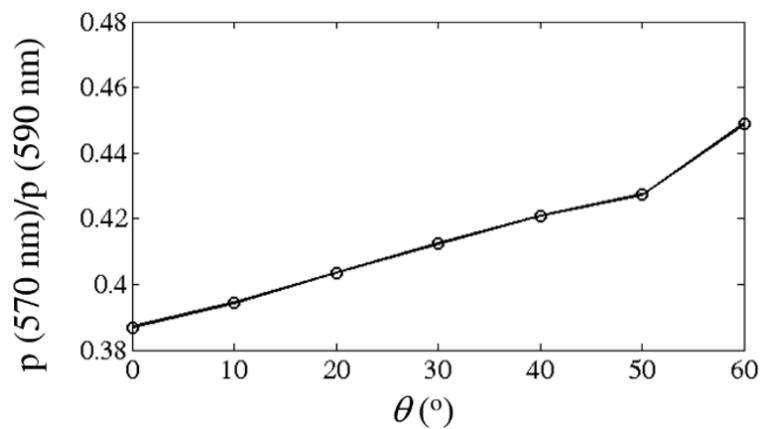
Figure 4-11 – Ratio of amplitude of PA signal at two wavelength combinations (p (590 nm) /p (570 nm)).

Different with multiple wavelength PAM, a single-wavelength OR-PAM was developed to measure SO_2 based on the non-linear optical absorption characteristic of hemoglobin[79]. Depending on different absorption coefficients, this method couldn't avoid the difference heat deposition pattern generated under diverse wavelengths, which will also exist measurement deviations for off-axial single-wavelength PAM.

CHAPTER 5.   OTHER WORKS

This chapter talks about the work I did in Georgia Institute of Technology. Application and functional simulation of PAM introduced in the former two chapters are based on absorption of hemoglobin which is endogenous absorber. However, the development of exogenous contrast agents extends the application range of PAM to weak absorbers or even non-absorbers with improved image sensitivity and targeting ability. Section 5.1 introduces a new photoacoustic contrast agent – DNA- templated silver cluster under the guidance of Prof. Robert M. Dickson, which shows strong PA signal compared with organic dyes, biocompatibility and nontoxicity. Section 5.2 broadens my research area into fluorescence imaging on life science, which talks about the two-dimensional receptor-ligand binding kinetics measurement by fluorescence correlation spectroscopy (FCS), which I did in Prof. Cheng Zhu's lab.

5.1   Study on New Photoacoustic Contrast Agent – DNA-templated Silver Nanocluster

In this section, a DNA-templated silver nanocluster as a new PA contrast agent is introduced, including the its structure, synthesis, and PA signal comparison with other organic dyes.

5.1.1   Introduction

Due to the complex compositions of living tissue, just based on endogenous absorbers in targeted tissues, the specificity and sensitivity of PA signal are sometimes

not high enough to do biomedical imaging. Thus, some exogenous absorbers like organic dyes, quantum dots and other nanoparticles are used as imaging contrast agents in PA[80]. ICG has already been proved by FDA. Due to the small size of organic dyes, they can penetrate the blood-brain barrier. However, there are also some drawbacks like organic dyes moving fast in the circulatory system which limits the imaging time and they easily seeping out of the blood vessel which causes a high background. The organic dyes can be encapsulated within nanoparticles to enhance optical absorption[81]. Besides the dye-containing nanoparticles, there is one category based on surface plasmon resonance (SPR). The nanoparticles like gold nanocages, carbon nanotubes and others have been used in the PA imaging[33, 34, 82]. The nanoparticles have some valuable attributes, like stability, non-photobleaching, long circulating time and strong optical absorption. However, due to the toxicity, a remaining question is whether the nanoparticles are safe to use for the human being, which blocks its way on the clinical trial.

Thus smaller size, biocompatible nanomaterials have emerged a promising class contrast agent in biomedical imaging. Due to the relative inertness and highly electronic transitions, molecular-scale noble metals, like gold and silver have been widely encapsulated by the coordinating ligands[83, 84]. The feature of metal encapsulated nanomaterials is related with the stoichiometry, geometry, charge, interaction with ligands and the buffer used. A higher concentration buffer will lead the immediate aggregation to form large Ag nanoparticles, thereby reducing the optical transitions. Thus, a compromise between ligand-Ag cluster interaction and optical transition should

be considered for the application. One of suggesting scaffold is oligonucleotide, whose electron-rich binding sites can be programmed by the changing the sequence of encapsulating biopolymer.

DNA-templated Ag nanocluster was firstly developed for fluorescence imaging[85-87]. With naturally genetic process, the single stranded deoxyribonucleic acid (ssDNA) or double stranded deoxyribonucleic acid (dsDNA) scaffolds are biocompatible and functional. Different sequence and length of DNA will cause different property of the synthesized nanoclusters, like the light absorption range covering from visible to near infrared (NIR) and the size of fluorophores. Due to the negative charge of DNA, it can bind to Ag ions effectively, to form a naturally encapsulated scaffold.

5.1.2   Synthesis

SsDNA was used as scaffolds in the synthesis of nanoclusters. The sequence and length, which determine the absorption spectrum, should be chosen carefully. Due to the experimental condition, we used the sequence CCCCCACTCC, whose absorption peak is around 570 nm. The ssDNA (Integrated DNA Technologies, IDT) was purchased in 1 μmole quantities in solid form, which was dissolved by deionized water to form a concentration of 50 μM in 1 mL of the solution. Then $AgNO_3$ (Sigma-Aldrich, 99.9999%) and $NaBH_4$ (Aldrich 98%) were added into the solution one by one. Depending on the target cluster, the ratio of $AgNO_3$ was ranged from 4:1 to 7:1 to the ssDNA, which was 4.8 in our case. As a strong reducing agent, ratio of $NaBH_4$ to Ag ions was 2:1, which could be slightly changed to get a single and pure absorption peak.

Then the tubing was put on a shaker to fully mix the solution and avoid the bulk aggregation. A few minutes later, the solution turned to be bright yellow. After sitting in the room temperature for 2 hours, the nanoclusters were readily made. The solution was kept in the 4 °C refrigerator to prolong the stability.
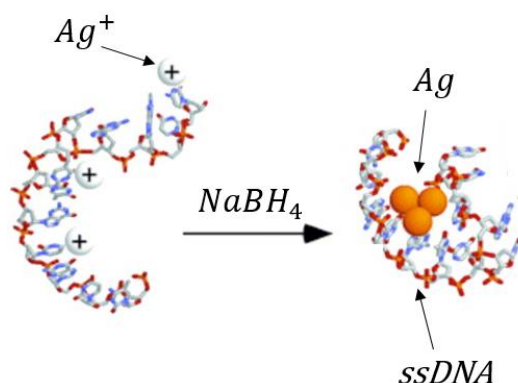
Figure 5-1 – Schema of DNA-templated Ag cluster creation[87].

Fig. 5-1 shows the schematic process of nanocluster creation. Due to the opposite charge of DNA strand and Ag ions, the oligonucleotide binds to the Ag^+ naturally. By adding the $NaBH_4$, Ag ions are reduced, then Ag atoms and agglomerates form. The size of Ag nanocluster is 2.76 nm by fluorescence correlation spectroscopy (FCS) detection, which is slightly larger than the organic dyes but at least an order of magnitude smaller than quantum dots [80, 83, 88]. Due to the DNA scaffold, the Ag nanocluster is non-toxicity.

5.1.3   Evaluation of optical specificity

Molar extinction coefficient is a significant parameter to evaluate the optical specificity of the fluorophores, which can be derived by the combination of absorption

value provided by Ultraviolet-visible spectroscopy (UV-Vis, Thermo Fisher Scientific) and solution's concentration calculated from FCS.

FCS exploits fluorescence fluctuations induced by low numbers of diffusing labeled particles in a confocal setup to analyze their concentrations and mobility. It can be used as an excellent way to detect the solution concentration. By detecting a known diffusion coefficient dye, the lateral and axial radii (ω_0, z_0) of detection area can be derived from the fitted curves. The effective focal volume V_{eff} then can be calculated by

$$V_{eff} = \pi^{3/2} \times \omega_0 \times z_0. \tag{39}$$
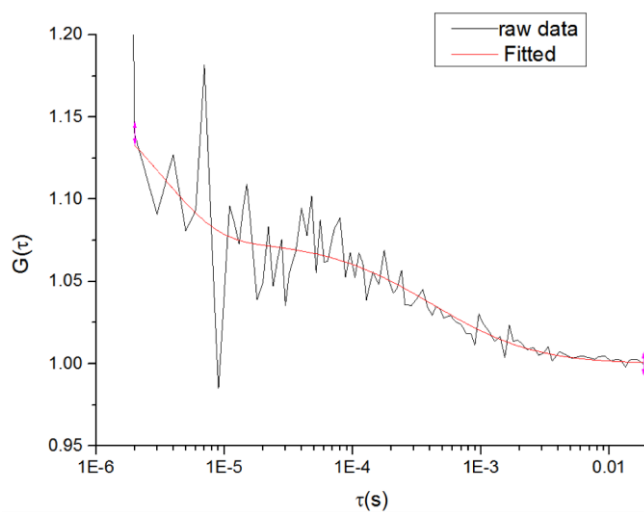
	$\omega_0 \,(\mu m)$	$z_0 \,(\mu m)$
1	0.61911	1.02632
2	0.50435	2.28358
3	0.64577	1.78522

Figure 5-2 – Autocorrelation curve of Cy3 and fitted parameters by 3 times.

We used Cy3 as tested dye, whose diffusion coefficient is 2.8 x 10^{-10} m^2 s^{-1}. Fig. 5-2 shows one of the Cy3 autocorrelation curve, and fitted parameters. By measuring three times, the average lateral and axial radii of focal volume are 0.590 μm and 1.698 μm, respectively, leading the V_{eff} = 3.3 fl.

Under the same condition, synthesized Ag nanocluster was measured by the FCS setup. To fit the suitable concentration for FCS, the sample was diluted 1,000 times. In order to get a reliable result, the experiment was done by 4 times. Fig. 5-3 is the statistical result, whose standard deviation is in the acceptable range. Considering the dilution, the averaged concentration of our synthesized Ag nanocluster is about 5 μM.
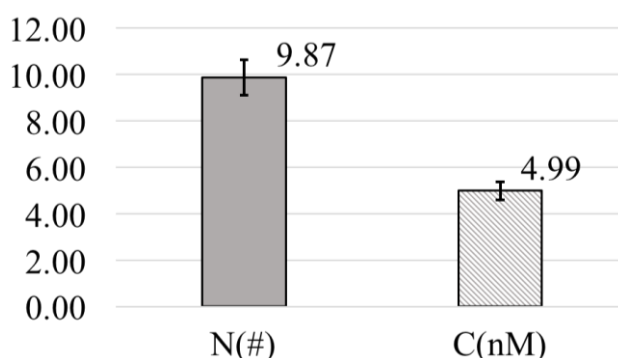
Figure 5-3 – Statistical result of Ag nanoclusters.

UV-Vis provides absolute value of absorption (A) along 1 cm optical length, which is defined as

$$A = \varepsilon \times l \times c, \tag{40}$$

where l is optical length 1mm, and c is the concentration of detected solution. Thus, by knowing the concentration, molar extinction coefficient can be calculated.

To fit the sensitive range of UV-Vis, the sample is diluted 10 times before measurement. Absorption spectrum of diluted Ag nanocluster is shown in Fig. 5-4. There are two peaks of the spectrum, the latter of which is the pure Ag nanocluster, and the former is contributed by the background, like DNA. Thus the absorption peak of synthesized Ag nanocluster is around 570 nm. In order to get the actual pure absorption value of Ag nanocluster, the contributed background should be subtracted, which is indicated by dark dashed line. Since concentration of Ag nanocluster in FCS is measured at 561 nm, the molar extinction coefficient should be calculated at same
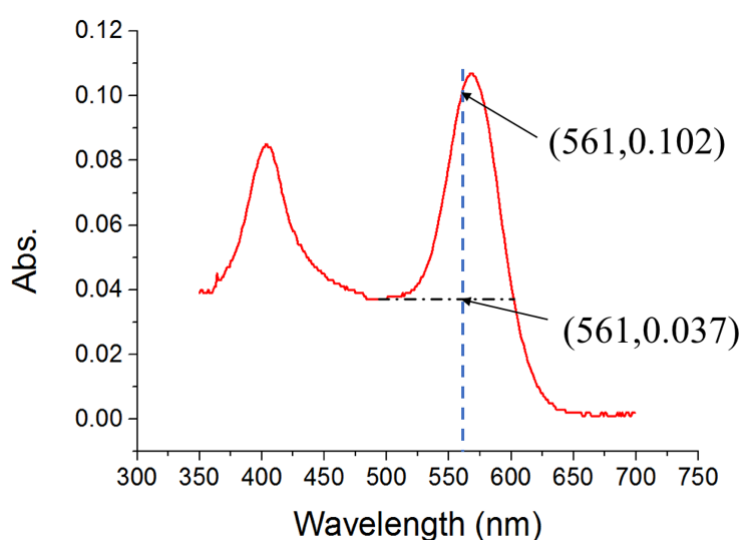
Figure 5-4 – Absolute absorption value of 10 times diluted Ag nanocluster. Dark dashed line represents background signal contributed to the absorption range of pure Ag nanocluster. Blue dashed line represents wavelength used in the FCS.

wavelength. From Fig. 5-4, the background and composed Ag nanocluster at 561 nm are 0.037 and 0.102, respectively, leading absorption value of pure Ag nanocluster is 0.065. Taking the acquired data into Eq. (40), the molar extinction coefficient of synthesized Ag nanocluster is 1.3×10^5 M^{-1} cm^{-1}.

Two organic dyes Rose Bengal (RB) and Eosin Y (EY), whose absorption spectrum covering 500 – 600 nm, were used as comparison group in our experiment. Fig. 5-5 shows the molar extinction coefficient of EY and RB in basic ethanol, whose absorption peaks are 111,854 M^{-1} cm^{-1} at 525 nm, and 90,108 M^{-1} cm^{-1} at 560 nm, respectively.
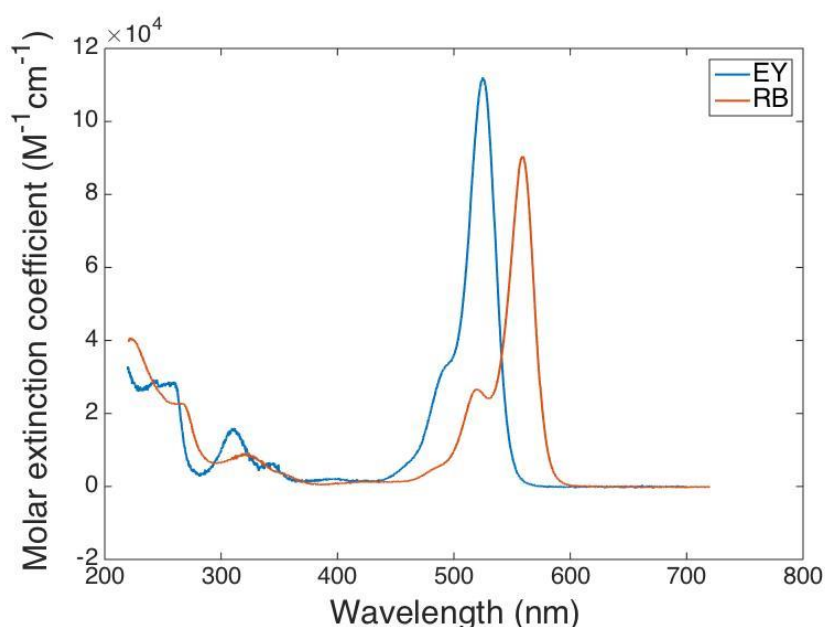
Figure 5-5 – Molar extinction coefficient of EY and RB.

Considering the quantity of the sample, we used poly (vinyl alcohol) (PVA) film to stabilize the solution, getting a thin layer. First, PVA solution was made by adding the PVA powder into ionized water until the solution was viscous, and the concentration was about 20% (20 g/100 mL). Then Ag nanocluster was uniformly diluted by the PVA solution to get a 500 μM concentration of nanocluster solution. The mixed solution was then spin coated onto a coverslip rotating at 1000 revolutions per minute, to make the

surface of film as even as possible. After by adding 3 to 4 times, the suitable thickness of film was formed. Because high frequency US has a very large attenuation when passing in the air, for PA experiment, the PVA film should be immersed under the water holder. To avoid dissolving in the water, PVA film was covered by a layer of polymethyl methacrylate (PMMA) solution. After the surface of final film was totally dried, it could be used in the PA experiment. Ultimate PVA film concentration of RB, EY and Ag cluster was 500 μM, 500 μM and 20 μM, respectively.
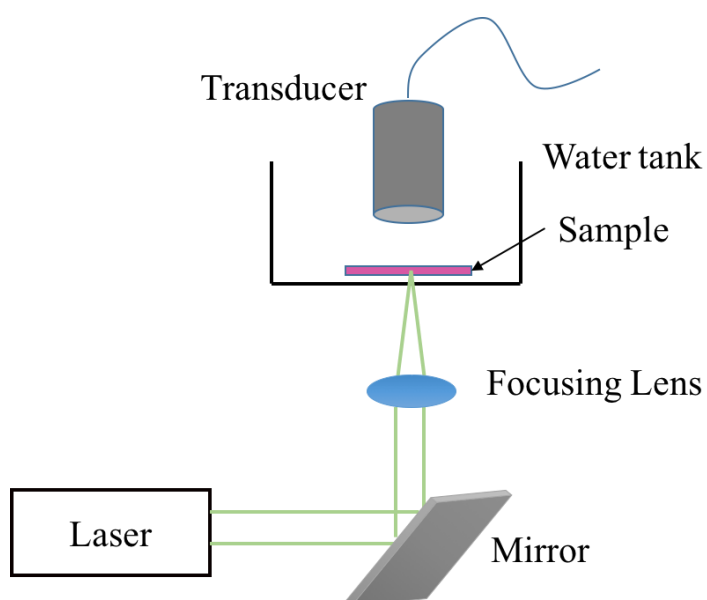
Figure 5-6 – Schema of PA detection.

Fig. 5-6 illustrated the schema of PA detection, with 10 MHz water-immersed focused transducer (Olympus A311S-SU), and 532 nm pulsed laser. Emitting laser was 532 nm, the repetition rate was 10 KHz with 2.5 mW energy. Then laser was focused onto the sample by the focusing lens, whose spot size was around 15 μm^2. Thus the energy per area illuminated on the sample was around 16.7 kw cm^{-2}. We used this setup to measure the EY, RB and Ag nanoclusters in sequence. Fig. 5-7 shows one pulse PA

signal of each sample. To be reliable, each signal was averaged by five randomly acquired signal. The peak to peak amplitudes of Ag nanocluster, EY and RB are about 32 mV, 13 mV and 10 mV, respectively. If the amplitudes are transferred under the same concentration, PA signal of Ag nanocluster is 61.5 folds higher than EY and 80 folds higher than RB, which demonstrates Ag nanocluster is a promising contrast agent for PA imaging.
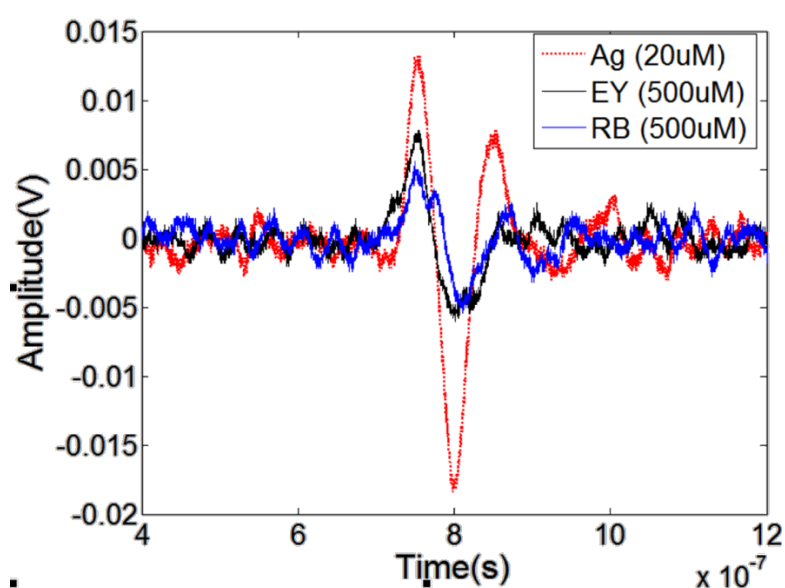
Figure 5-7 – PA signal of Ag nanocluster, Eosin Y and Rose Bengal.

5.1.5   Conclusion and Discussion

In this section, we have studied on a new photoacoustic contrast agent, which is DNA-templated Ag nanocluster. Due to the high optical absorption and quantum yield, this Ag nanocluster has emerged as a promising contrast agent for fluorescence detection. Like ICG, which is firstly used in fluorescence imaging, is demonstrated an excellent PA contrast agent later. The aim of our experiment is to study whether Ag

nanocluster a good PA agent, because it has other some invaluable properties such as photophysical stability and biocompatibility, which are significant for living imaging.

By self-synthesizing, measuring its optical specificity and comparing PA signal with other common dyes, we have demonstrated the DNA-templated Ag nanocluster a promising PA contrast agent. Moreover, Ag nanocluster has been identified an excellent dark-state fluorescence enhancement property, induced by a secondary longer wavelength laser[87]. Ag nanocluster has a ~30 μs dark state which is longer than nanosecond fluorescence lifetime. After absorbed the energy from primary laser, electrons existed on the ground state will be pumped into the excited state, some of which will drop back the ground state by emitting fluorescence and others will go to the dark state. Thus by illuminating a secondary laser whose wavelength is during the absorption range of dark state, the electrons sitting in the dark state will be pumped into another higher energy level and emit enhanced fluorescence during its way back to ground state. Based on the same energy model, PA signal can also be modulated[89-91]. Thus the future work is to study on the PA modulation of Ag nanocluster, which will do great help to exclude the background signal, and contribute to the development of innovative PA contrast agents.

5.2   Two-dimensional Receptor-ligand Binding Kinetics Measurement by FCS

FCS is a correlation analysis of fluctuation of the fluorescence intensity, which detects the movement of fluorophores in the focal volume. Even though, fluorescent and mechanical methods have been used to measure the receptor-ligand binding

kinetics, their different measurement mechanics lead to large imparity. Combined with the tiny interested volume and spontaneous interaction between receptors and ligands, FCS can provide more specific kinetics information. The aim of this section is to explore the capability of FCS on measurement of two-dimensional (2D) receptor-ligand binding kinetics. The preparation of 2D biological model is also introduced.

5.2.1   Introduction

5.2.1.1   Significance of 2D Kinetics Measurement

Receptor-ligand interactions mediate many important processes in cell adhesion and communication at the membrane interfaces. By the morphological change, concentrated and organized adhesion and signaling molecules, information and substance transfer between the cells, which includes neural synapses and immunological responses[92, 93]. The adhesion receptors acting as the signaling passengers, diffuse in and out of the membrane interface, contact their ligands via extracellular domain, and link to cytoskeletal or adaptor molecules via cytoplasmic domain. Quantitating the adhesion is required for understanding the reaction mechanism of the immunological synapses. Kinetic rate is one of the important parameters to quantify the signaling effect[94]. Three-dimensional (3D) parameters of molecular interactions have proved significant insight, in which at least one of the molecules is in the solution. Compared with 3D parameters, 2D binding is more closely to the *in vivo* interaction of immunological system, giving us a better understanding of how the ligands and receptors aggregate and adhere on the opposing membranes.

5.2.1.2 <u>Fluorescence Correlation Spectroscopy</u>

As a well-established technique, FCS allows the measurement of diffusion coefficient and concentration for fluorescing constructs by recording the fluorescent fluctuation induced by movement of fluorophores across the detection volume. Fig. 5-8 illustrates the schema of inverted FCS setup, in which the excitation laser is focused on the sample in a tiny focal volume by the objective. The effective focal volume V_{eff} is described as

$$V_{eff} = \pi^{3/2}\omega_0{}^2 z_0, \tag{41}$$

where ω_0 and z_0 are lateral and axial dimensional radii of focal volume.The emissive fluorescence is accepted by a high sensitive camera or avalanche photo diode (APD), and time-correlated signal is then calculated by the correlator.
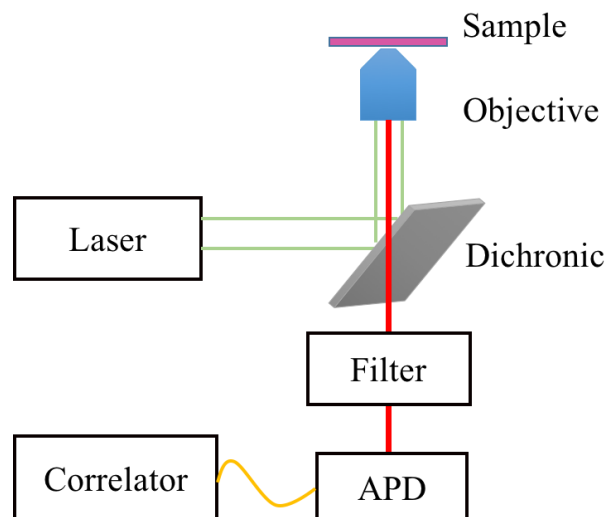
Figure 5-8 – Schema of FCS setup.

When the individual molecules diffuse through the detection volume, fluorescent intensity fluctuates along the time which is recorded by the detector. Autocorrelation analysis of the fluctuation signal can provide the information about the concentration, diffusion, and binding characteristics of the molecules. The fluorescent autocorrelation function is defined as

$$G(\tau) = \frac{\langle \delta F(t) \delta F(t+\tau) \rangle}{\langle F \rangle^2},$$

(42)

Where brackets $\langle ... \rangle$ denotes the time average and fluorescence fluctuation $\delta F(t) = F(t) - \langle F \rangle$ is the difference between the instantaneous and average intensity. τ is lag time and $G(\tau)$ decreases with correlation time to zero at $\tau = \infty$, which represents the self-similarity in the signal, as the fluctuations at time $t + \tau$ are caused by different particles at time t. A theoretical expression describing the autocorrelation data is established to extract the parameters such as the concentration C, dissociation rate constant k_d, and the diffusion coefficient D. The expression is described as

$$G(\tau) = N_{eff}^{-1} \frac{1 - F_{trip} + F_{trip}\exp(-\tau/\tau_{trip})}{1 - F_{trip}}$$

(43)

$$\times \frac{1}{1 + \tau/\tau_{diff}} \left(\frac{1}{1 + \tau/(S^2\tau_{diff})} \right)^{1/2} + \begin{cases} 0' \\ 1 \end{cases}$$

where N_{eff} is the effective number of molecules in the effective detection volume, F_{trip} is average fraction of particles in triplet state, τ_{trip} is triplet relaxation time, S is structure parameter ($S = z_0/\omega_0$) and τ_{diff} is diffusion time which is related with diffusion coefficient D, by

$$\omega_0^2 = 4D\tau_{diff}. \tag{44}$$

5.2.1.3 FRAP, CLSM and IRM

By detecting the recovery fluorescence intensity after bleached by high power laser within a defined area, FRAP provides a powerful way to measure the kinetics of 2D model. Thus, it is used to test the mobility of self-made lipid bilayer by fitting the corrected fluorescence intensity recovery curve[95, 96].

With adding a spatial pinhole at the focal plane of lens, CLSM eliminate the out of focus light, providing higher resolution than the common microscopy. In our experiment, the IgG is expressed on the outer membrane of the cell. Thus it is necessary to use high axial resolution microscopy to investigate the morphological change of ligand and receptor on the contact area caused by binding interaction.

IRM is widely used to study the cellular behaviors, including cell adhesion, motility, exocytosis and endocytosis. By detecting the interference of reflected polarized light by glass slide - medium interface and medium – cell membrane interface, intensity of IRM is the distance function of cell surface between glass slide. The darker intensity, the farther distance. Thus, IRM is an excellent technique to assess whether cell and lipid forms a contact area, which can be achieved based on the commercial CLSM.

5.2.2 Methods

<u>2D Biological Model</u>

Relying on the Fc portion, antibodies make interaction with effector systems, who express the receptor for the Fc portion (FcR). FcR plays an important role on many antibody dependent disease and antibody based immunotherapy[97]. Different FcR is associated with the certain antibody. As a receptor for monomeric immunoglobulin G (IgG), FcγRIIA (CD32) is expressed on macrophages, neutrophils, eosinophils, platelets and langerhans cells. The interaction between CD32 and IgG is what we study in this section.
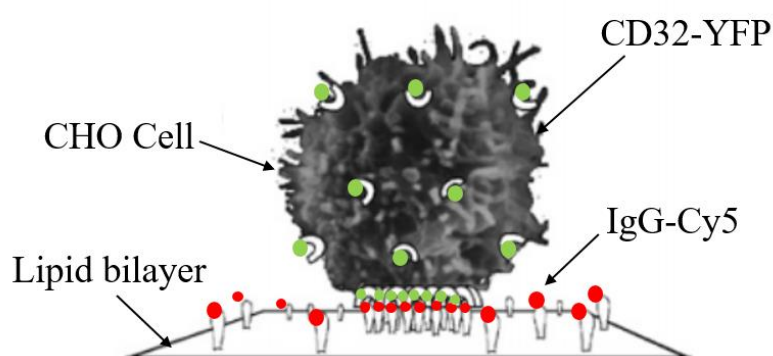
Figure 5-9 – 2D biological model.

Fig. 5-9 illustrates the 2D biological model. In order to investigate binding interaction between CD32 and IgG, fluorophores yellow fluorescence protein (YFP) and Cy5 are linked to them respectively. The two fluorophores are carefully chosen to avoid cross section of excitation and emission range and fluorescence resonance energy transfer (FRET). In this model, self-designed gene which links the and is uniformly transfected and expressed on the outer membrane of Chinese Hamster Ovary (CHO)

cell. IgG labeled with Cy5 is linked on the lipid bilayer. The aggregation of ligand and receptor indicates the binding interaction occurs. Kinetics can be measured on the contact area.

5.2.2.2   <u>Sample Preparation</u>

Making a plain, good mobility lipid bilayer is a challenging and fundamental step for this experiment. Some factors, like size and uniformity of liposome, flatness and aggression of the lipid, ion concentration and temperature and others, decide the quality of the ultimate lipid bilayer[98-100]. Rabbit monoclonal anti-dinitrophenyl (DNP) IgG (Cell Signaling Technology) was labeled by Cy5 (N-HydroxySuccinimide) NHS ester (Lumiprobe), according to the protocol –NHS ester labeling of amino biomolecules– provided by the Lumiprobe. Liposomes of 1,2-dioleoyl-sn-glycero-3-phosphocholine (DOPC) and 1,2-dipalmitoyl-sn-glycero-3-phosphoethanolamine-N-(2,4-dinitrophenyl) (DNP-PE) were purchased via Avantic Polar Lipids, Inc. in chloroform. DOPC and DNP-PE solution were first dried in vacuum for 1h, and then dissolved in TSA (25 mM Tris, 150 mM NaCl, 0.02% NaN$_3$) containing 1.5% OG (*n*-octyl *β*-D-glucopy-ranoside) to a concentration of 0.4 mM. After sitting a while to be transparent, two lipid mixture solutions were injected into respective dialysis cassette. The cassette suspended in 1.5 L dialysis solution for 36 h and TSA was replaced every 12 h. Then liposomes of DNP-PE and DOPC were formed, and DNP-PE was diluted with DOPC at different concentration ratio during the experiment.
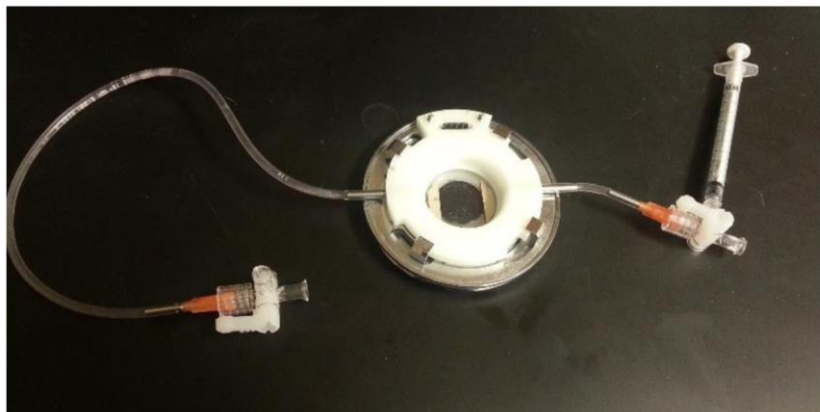
Figure 5-10 – Photo of FCS2.

Lipid was formed on the coverslip of Focht Chamber System 2 flow chamber (FCS2, Bioptechs), which is a closed system. With optical surface and electronically conductive coating, its microaqueduct slide provides perfusion and uniform temperature control for the coverslip at 37 $^{\circ}$C. Singular rectangle gasket between microaqueduct slide and coverslip separate them from each other at 0.25mm, leaving space for one-layer cell. Previously, Coverslip was cleaned by the boiling in piranha solution (70% reagent grade sulfuric acid, 30% of 30% hydrogen peroxide) for 1h, cleaned by ionized water and then air-dried by nitrogen. A 2 μl drop of mixed liposomes was tiled on the coverslip, forming a continuous bilayer. There were two valves on each side of FCS2, to be responsible for the solution in and out while preventing the air bubbles showing in the window of flow chamber. One valve was connected with a syringe to inject the buffer and cells. The basis solution was HEPES – buffered saline (HBS), in which every 200 mL distilled water dissolving NaCl 1.6 g, KCl 0.074 g, Na_2HPO_4 ·$2H_2O$ 0.027g, dextrose 0.2 g and HEPES 1g. Three solutions were used in the experiment, with adding different chemicals: 1% bovine serum albumin (BSA)

(HBS+BSA); 0.08% of 1M $MgCl_2$, 0.15% of 0.1 M $CaCl_2$ and 5% of FBS (Imaging buffer); 4% human albumin (HBS+HA). After 15 min incubation, the excess liposome solution was washed off by injecting HBS+BSA through the chamber. After another 15 min, 200 μL anti-DNP IgG-Cy5 was injected into chamber and linked on the lipid, whose DNP ratio decided the ultimate concentration of linked IgG. After 30 min incubation, HBS+HA was used to remove the unbound IgG. Then CHO-CD32-YFP cells suspended in imaging buffer were injected at least 20 min before imaging. The chamber was covered by a piece of foil after injection of IgG to avoid photobleaching.

5.2.2.3 <u>Sample Test</u>

Two tests have been done to verify whether the prepared samples work. One is the demonstration of successful cell transfection by flow cytometry and another one is to test the mobility of lipid bilayer by FRAP.

In the cell transfection test, commercial dye linked IgG, allophycocyanin (APC) - Vio 770 conjugated anti-CD32 antibody (IgG-APC-Vio770, MACS Miltenyl Biotec) was used as ligand. Cells of control group was plain CHO cell without CD32 expression. Both control and experimental group were incubated with IgG-APC-Vio 770, and rinsed to get rid of the non-interactive IgG. Two channels were set in flow cytometry to investigate the fluorescence photon counts of YFP and APC-Vio 770. Control group (plain CHO + IgG-APC-Vio 770) was first measured under two channels to identify and get rid of the background signal. Keeping the same condition, the experimental

group (transfected CHO + IgG-APC-Vio 770) was then detected. In order to acquire high expression cells, the cultured cells can be sorted every 2 months.

CLSM (Zeiss 780) was used to test the mobility of lipid bilayer. Two same area circular regions of lipid were selected, one of which was defined as experimental region and another one was the background. Only the experimental region was bleached by the high power laser. The accumulated fluorescent intensity recordation of two regions started 3 frames before the photobleaching to acquire pre-bleach value, and lasted long enough until intensity of experimental region was stable. FRAP data was corrected by subtracting the background intensity, then normalized by the pre-bleach value. Then the diffusion coefficient can be derived by nonlinear least-squares fitting of the corrected recovery curve[96].

5.2.2.4 FCS Measurement

A series concentration gradient of lipid sample was prepared which varies from 0.2 to 2000 per μm^2 at 10 times step. Suitable lipid concentration and touched layer between cell and lipid were identified by the IRM and CLSM, and reconfirmed by z stack FCS of lipid at 1 μm step. Fluorescein and Cy5 were used to test the focal volume of FCS system before the measurement started. The fluorescence fluctuation and autocorrelation curve of cell and lipid were acquired and calculated by the Zeiss 780 microscopy with simultaneously at 37 °C. Laser was set at 488nm (YFP) and 633nm (Cy5), and the dichronic mirror was chosen 488/633 which reflected the excitation laser wavelengths. Emission fluorescence photons from YFP and Cy5 were filtered by the

corresponding filters and received by different APDs. For each cell, 3 positions on the contact area and one position out of the cell were chosen as experimental and control group, respectively. At least 4 cells in good condition were measured at the suitable concentration.

A lot of trials have been done to get the good fitting curves, like changing objectives, choosing a suitable fitting function, adjusting laser intensity and finding good conditions. For our model, the fitting function is defined as,

$$G(\tau) = 1 + \frac{1}{N} \times \left[1 + \frac{F_{trip}}{1 - F_{trip}} \times e^{-\frac{\tau}{T_{trip}}} \right] \times \sum_{i=1}^{r} f_i \times \left(1 + \frac{4D_i\tau}{w_0^2} \right)^{-1}, \quad (45)$$

where r is varied with sample categories: r is 2, when the lipid out of cell is imaged, because only free ligand exists in this area; r is 3, when contact area is imaged, because both ligand-receptor complex and free ligand/receptor are in this field. Photobleaching effect is also considered into both of conditions. From high to low value, the diffusion coefficients are named D1, D2 and D3, respectively.

5.2.3 Experimental Results

Fig. 5-11 is the flow cytometry results, two columns of which are control and experimental group, respectively. Because no CD32 expression, there is no effective fluorescence of YFP and APC-Vio 770 showed in the control group. In the experimental group, both detection channels give a high effective photon counts and linear relationship between them, demonstrating the complex is combination of CD32-YFP and IgG-APC-Vio 770. Thus this experiment can illustrate CD32-YFP is

successfully transfected on the outer membrane of CHO cell. Fig. 5-12 shows FRAP image taken at 0s, 10s and 22s respectively after bleaching and fluorescence recovery curve. By fitting the curve, diffusion coefficient of the lipid bilayer is 1.3 μm^2 s^{-1}.
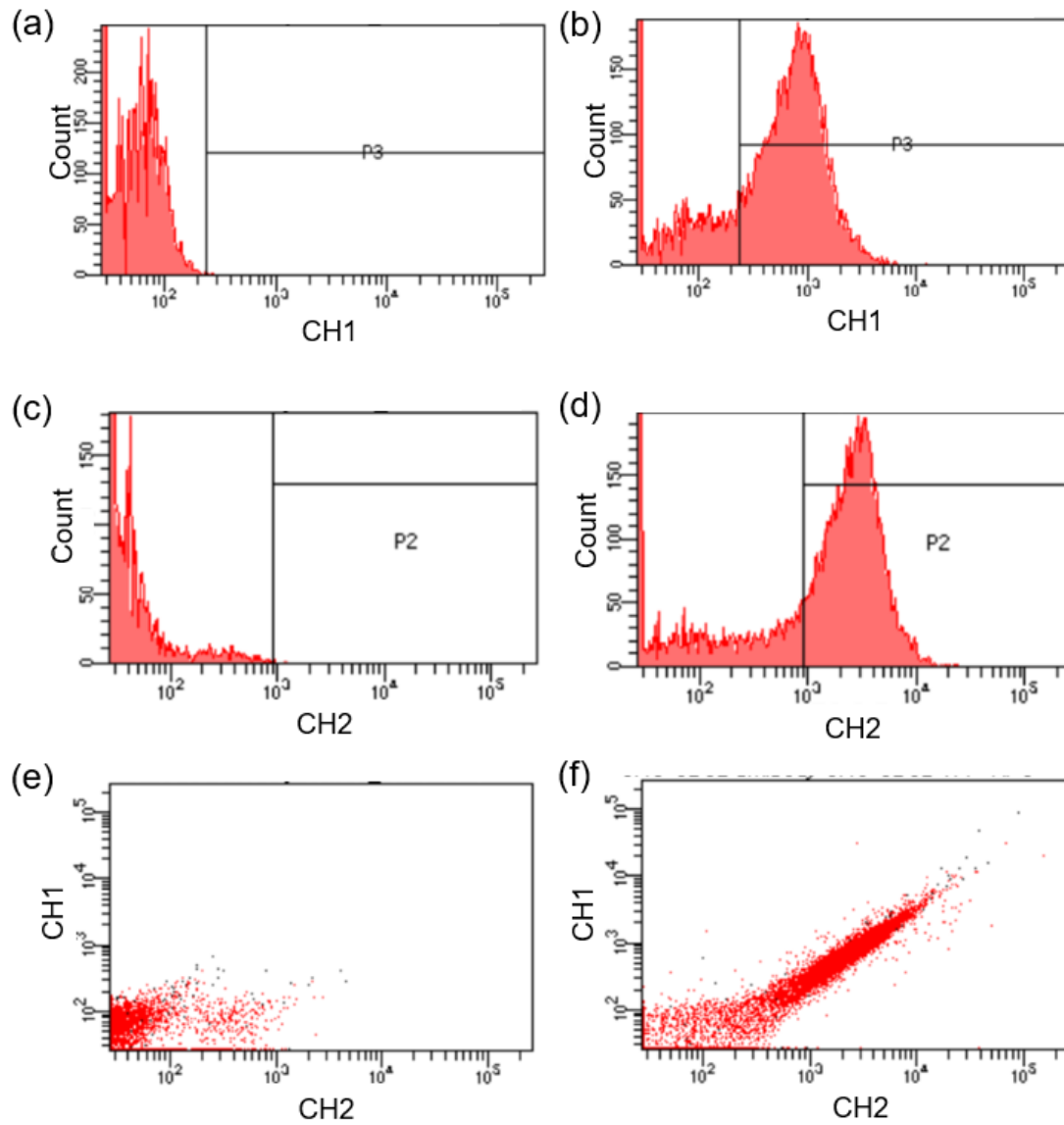
Figure 5-11 – Flow cytometry results of transfected cell (b, d, f) vs. plain cell (a, c, e). CH1, YFP emission channel. CH2, APC-Vio 770 emission channel.
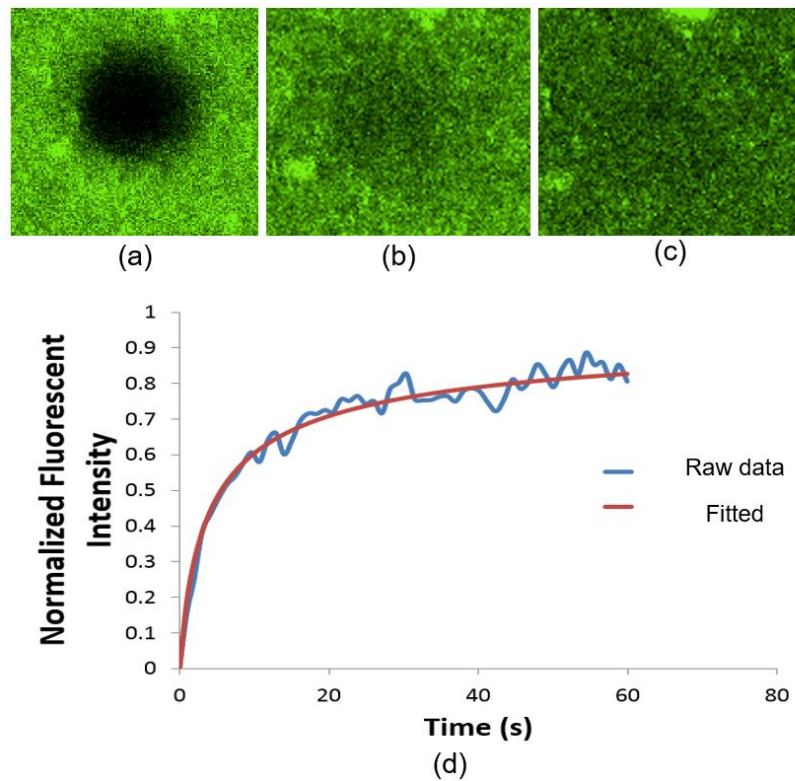
Figure 5-12 – Diffusion coefficient measurement of lipid bilayer by FRAP. (a) (b) and (c) are FRAP image taken at 0s, 10s and 22s respectively after bleaching. (d) is raw fluorescent intensity and fitting curve.

On the touched layer of cell and lipid bilayer, IRM and corresponding wide field image are shown in Fig. 5-13. When the cell attaches the lipid, approximate half wavelength shift occurs between the reflected light from glass slide surface and membrane surface. And the interference leads to the darker intensity of the image, representing the contact area. However, when the cell apart from the lipid or no cell exists, phase shift between two reflected interface becomes smaller, resulting in a bright pixel in the image, which is the surrounding area of the dark circle in Fig. 5-13 (a).

(a)   (b)
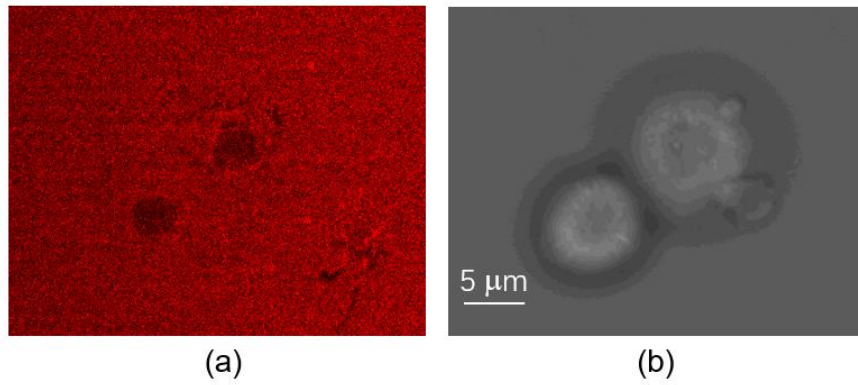
Figure 5-13 – IRM (a) and wide field (b) image on contact layer.

Fig. 5-14 shows fluorescent image of cell and lipid and wide field image on the contact layer. Aggregation of YFP and Cy5 also demonstrates the contact formed between the cell and lipid, which is accordance with the IRM result.

(a)   (b)   (c)
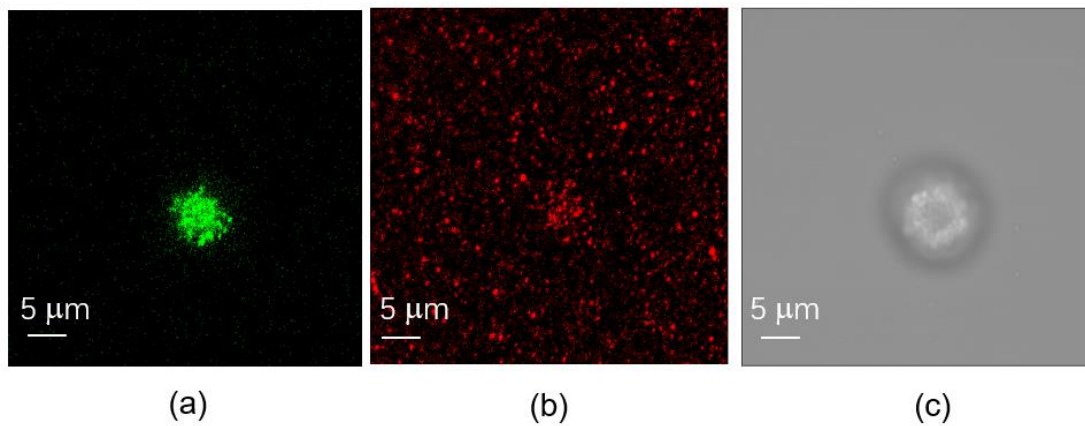
Figure 5-14 – Fluorescent image of cell (a) and lipid (b), and wide field image (c) on contact layer.
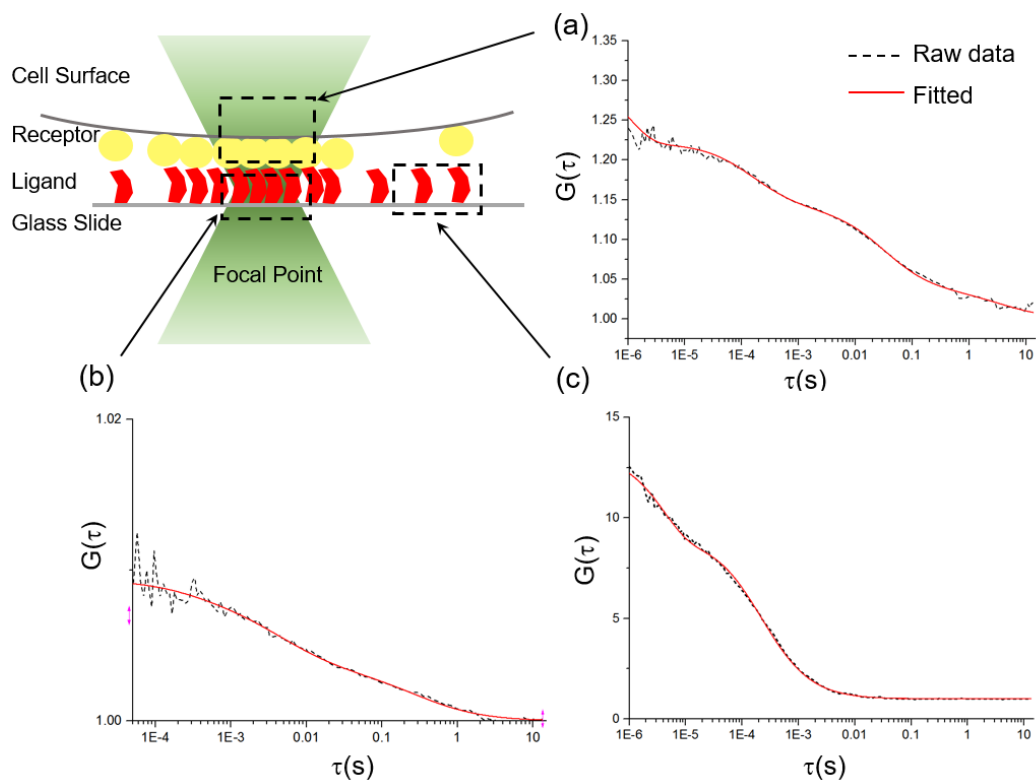
Figure 5-15 – Autocorrelation curve of receptors (a) at 488 nm excitation and ligands (b) at 633 nm excitation of focal point and ligands out of contact area (c) at 633 nm excitation. The black dashed line is raw data and red solid line is fitted curve.

Some interesting results have been acquired from FCS measurements after doing statistical analysis of at least 10 points. On the same focal point of contact area, the autocorrelation curves of receptor and ligand are shown in Fig. 5-15 (a) and (b). D1 value stands for the diffusion coefficient of free molecules, which is 2.5 $\mu m^2\,s^{-1}$ for receptor and 2.34 $\mu m^2\,s^{-1}$ for ligand. D2 value is the diffusion coefficient of receptor-ligand complex, which is 0.6 $\mu m^2\,s^{-1}$. Comparing Fig. 5-15 (b) and (c), lipid on contact area diffuses much slower than out of it. The diffusion coefficient of free ligand is about 2.4 $\mu m^2\,s^{-1}$, which is comparable to the D1 value on contact area.

5.2.4   Conclusion and Discussion

In this section, we have used FCS to measure 2D kinetics, which is more closely to the real living circumstance than 3D kinetics. A 2D model was developed to study the receptor-ligand interaction of CD32-YFP on CHO cell and IgG-Cy5 on lipid bilayer. A lot of efforts have been made on the sample preparation, like cell transfection, lipid bilayer formation, and the self-developed protocol for FCS measurement. Cell and lipid bilayer was verified successfully by Flow cytometry and FRAP. Before FCS measurement, IRM and CSLM aided to specify the contact area and choose the suitable concentration. By detecting fluorescence fluctuation of small amount of molecules, FCS can provide more detail information than FRAP and micropipette. Fitting autocorrelation curve with multi-fraction function, diffusion coefficient of free ligand/receptor and the complex can be differentiated, even on the same imaging point. From FCS curve and fitting results of our model, diffusion coefficients of ligand with receptor is much slower than without receptor, and on the point of contact area, D1 and D2 values of ligand and receptor are comparable.

Affinity of receptor and ligand is also a significant parameter to study the pathology, which can be further measured by fluorescence cross-correlation spectroscopy (FCCS). We used double strand DNA (dsDNA) with rhodamine green and Cy5 linked on each end to test the overlap of 488 nm and 633 nm focusing point[101]. However, our setup is not ideal and need further adjustment. Temperature influence on lipid mobility was considered in our preparation. To give a clear demonstration, a comparison experiment was done by two conditions, one of which was heated from preparation and another was only heated during imaging. Under each condition,

recovery rate of three different positions were measured, shown in Fig. 5-16. Average

recovery rate of condition 1 is higher than condition 2, which is coincidence with the

recommendation by Marie-Paule *et al.* (2008)[100].
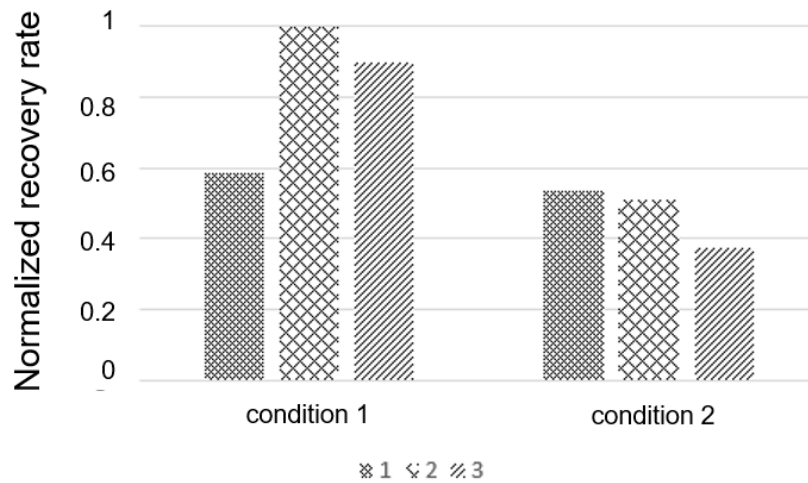
Figure 5-16 – Temperature influence on lipid mobility. Condition 1 is heated from preparation. Condition 2 is heated only during imaging.

CHAPTER 6.   CONCLUSION

Development of biomedical microscopy provides the possibility to explain bio-mechanism at molecular level. Different from pure optical microscopies, PAM is based on the light absorption of intrinsic chromophores of living tissue, which has a 100% sensitivity to the change in optical absorption coefficient and background-free contrast[18]. Meanwhile, with multiple wavelengths, spectroscopic PA can provide functional information, such as SO_2, which represents the local metabolic level. As one of most common imaging method, US is widely used to provide deep tissue structural information, due to low scattering. Combined with US modality, PA/US microscopy can not only provide high resolution and contrast image but also long penetration depth structure information, which will be a position guidance for the PAM.

Based on our research, the representative OR-PAM systems have some limitation making them hard to implement US modality, like using flat transducer or acoustic multi-times reflection by prism before transducer. Meanwhile relying on acoustic focusing, the resolution of current PA/US integrated system is limited. Thus, it's necessary to develop a PA/US system at optical resolution level to investigate tinier structure.

In this thesis, we have developed three novel PA/US dual-modality microscopies, each of which is the improved version of the previous one. First one is mechanical scanning based PA/US microscopy, in which a glass slide is used to transmit light and reflected acoustic wave, detected by a 25 MHz focused transducer. This system can reach a capillary-scale resolution,

which was demonstrated by imaging the microcirculation system of mouse ear. Also by this system, we acquired the high resolution small animal whole eye PA/US dual-modality imaging, which demonstrates our system is a promising method to diagnose ocular diseases.

To improve the scanning speed, we used a water-immersible MEMS scanning mirror, and developed two other systems. One is combined with PR, which is light transparent and US focused, another one is PM which focuses light and US simultaneously. MEMS-PR has some defects, like hardly corrected light aberration and long optical focusing length, which is overcame by the advanced MEMS-PM PA/US microscopy. By using flat transducer, the MEMS scanning based microscopies are convenient to vary the NA. of US and change transducer with different central frequency, which is always a problem for using focused transducer. Thus, even though our system uses 20 MHz transducer, this can be changed for different imaging purposes.

In PAM systems, besides previously developed optics and ultrasound coaxial systems, the off-axial design can reach a higher scanning speed by using galvanometer out of water. Thus the third part of my work is to investigate the effect of oblique detection on SO_2 measurement accuracy by simulating calculation and phantom experiment. We have reached the conclusion that inaccuracy increases with the transducer deflection angle increase, and other factors like optical wavelengths, actual SO_2 value or transducer bandwidth also influences the measurement. Also a brief theoretical analysis was approached.

Besides the application of PA on living tissues, we have studied a new PA contrast agent – DNA-templated silver nanocluster. With small size and DNA encapsulated, this nanocluster

115

has nontoxicity and high bio-compatibility. The last work is to measure 2D kinetics by FCS,

providing a new method to investigate the 2D molecular mechanics of immunology.

APPDENDIX A. COPYRIGHT INFORMATION

Chapter 1; Figures 1-2:

Reprinted (adapted) with permission from Ref. 4 Copyright 2006 Nature publishing group.

Chapter 1; Figures 1-3:

Reprinted (adapted) with permission from Ref. 12 Copyright 2000 Elsevier.

Chapter 1; Figures 1-4:

Reprinted (adapted) with permission from Ref. 18 Copyright 2012 American Association for the Advancement of Science.

Chapter 1; Figures 1-7 (b) and (c):

Reprinted (adapted) with permission from Ref. 24 Copyright 2006 Nature Publishing Group.

Chapter 1; Figures 1-8:

Reprinted (adapted) with permission from Ref. 26 and Ref. 27 Copyright 2011 Optical Society of America.

Chapter 1; Figures 1-11 (a) and (b):

Reprinted (adapted) with permission from Ref. 39 Copyright 2016 Nature Publishing Group.

Chapter 1; Figures 1-11 (c) and (d):

Reprinted (adapted) with permission from Ref. 40 Copyright 2013 WILEY-VCH Verlag GmbH & Co.

Chapter 1; Figures 1-12 (a) and (b):

Reprinted (adapted) with permission from Ref. 41 Copyright 2009 Optical Society of America.

Chapter 1; Figures 1-12 (c) and (d):

Reprinted (adapted) with permission from Ref. 42 Copyright 2010 Optical Society of America.

Chapter 1; Figures 1-13:

Reprinted (adapted) with permission from Ref. 43 Copyright 2015 Optical Society of America.

Chapter 2; Figures 2-1 (a):

Reprinted (adapted) with permission from Ref. 50 Copyright 2014 Optical Society of America.

Chapter 3; Figures 3-11, 3-12, 3-13, 3-14:

Reprinted (adapted) with permission from Ref. 50 Copyright 2014 Optical Society of America.

Chapter 4; Figures 4-1, 4-3, 4-4, 4-6, 4-7, 4-9, 4-10:

Reprinted (adapted) with permission from Ref. 75 Copyright 2016 IOP publishing.

Chapter 5; Figures 5-1:

Reprinted (adapted) with permission from Ref. 87 Copyright 2013 American Chemical Society.

REFERENCES

[1] Davidson, M.W. and M. Abramowitz, *Optical microscopy*. Encyclopedia of imaging science and technology, 2002.

[2] Murphy, D.B. and M.W. Davidson, *Confocal Laser Scanning Microscopy*, in *Fundamentals of Light Microscopy and Electronic Imaging*. 2012, John Wiley & Sons, Inc. p. 265-305.

[3] Paddock, S.W., *Confocal laser scanning microscopy*. Biotechniques, 1999. **27**: p. 992-1007.

[4] Willig, K.I., S.O. Rizzoli, V. Westphal, et al., *STED microscopy reveals that synaptotagmin remains clustered after synaptic vesicle exocytosis*. Nature, 2006. **440**(7086): p. 935-939.

[5] Huang, B., M. Bates and X. Zhuang, *Super resolution fluorescence microscopy*. Annual review of biochemistry, 2009. **78**: p. 993.

[6] Farahani, J.N., M.J. Schibler and L.A. Bentolila, *Stimulated emission depletion (STED) microscopy: from theory to practice*. Microscopy: science, technology, applications and education, 2010. **2**: p. 1539.

[7] Rust, M.J., M. Bates and X.W. Zhuang, *Sub-diffraction-limit imaging by stochastic optical reconstruction microscopy (STORM)*. Nature Methods, 2006. **3**(10): p. 793-795.

[8] Testoni, P.A., *Optical coherence tomography*. The Scientific World Journal, 2007. **7**: p. 87-108.

[9] Kim, J., W. Brown, J.R. Maher, et al., *Functional optical coherence tomography: principles and progress*. Physics in medicine and biology, 2015. **60**(10): p. R211.

[10] Huang, D., E.A. Swanson, C.P. Lin, et al., *Optical coherence tomography*. Science (New York, NY), 1991. **254**(5035): p. 1178.

[11] Hee, M.R., J.A. Izatt, E.A. Swanson, et al., *Optical coherence tomography of the human retina*. Archives of ophthalmology, 1995. **113**(3): p. 325-332.

[12] Fujimoto, J.G., C. Pitris, S.A. Boppart, et al., *Optical coherence tomography: an emerging technology for biomedical imaging and optical biopsy.* Neoplasia, 2000. **2**(1): p. 9-25.

[13] Bell, A.G., *On the Production of Sound by Light.* American Journal of Science, 1880. **20**: p. 305-324.

[14] Li, C. and L.V. Wang, *Photoacoustic tomography and sensing in biomedicine.* Physics in Medicine and Biology, 2009. **54**(19): p. R59-R97.

[15] Oraevsky, A.A., S.L. Jacques and R.O. Esenaliev, *Optoacoustic imaging for medical diagnosis* 1996: USA.

[16] Oraevsky, A.A., R.O. Esenaliev and A. Karabutov, *Laser optoacoustic tomography of layered tissues: Signal processing.* Optical Tomography and Spectroscopy of Tissue: Theory, Instrumentation, Model, and Human Studies Ii, Proceedings Of, 1997. **2979**: p. 59-70.

[17] Wang, L.H.V., X.M. Zhao, H.T. Sun, et al., *Microwave-induced acoustic imaging of biological tissues.* Review of Scientific Instruments, 1999. **70**(9): p. 3744-3748.

[18] Wang, L.V. and S. Hu, *Photoacoustic tomography: in vivo imaging from organelles to organs.* Science, 2012. **335**(6075): p. 1458-1462.

[19] Morse, P.M. and K.U. Ingard, *Theoretical Acoustics*. 1986, Princeton, New Jersey: Princeton University Press. 927.

[20] Diebold, G., T. Sun and M. Khan, *Photoacoustic monopole radiation in one, two, and three dimensions.* Physical review letters, 1991. **67**(24): p. 3384.

[21] Gusev, V. and A. Karabutov, *Laser optoacoustics. ch. 2, 3 AlP, N*. 1993, Y.

[22] Maslov, K., G. Stoica and L.V. Wang, *In vivo dark-field reflection-mode photoacoustic microscopy.* Optics letters, 2005. **30**(6): p. 625-627.

[23] Xie, Z., L.V. Wang and H.F. Zhang, *Optical fluence distribution study in tissue in dark-field confocal photoacoustic microscopy using a modified Monte Carlo convolution method.* Applied optics, 2009. **48**(17): p. 3204-3211.

[24] Zhang, H.F., K. Maslov, G. Stoica, et al., *Functional photoacoustic microscopy for high-resolution and noninvasive in vivo imaging.* Nat Biotech, 2006. **24**(7): p. 848-851.

[25] Song, K.H. and L.V. Wang, *Deep reflection-mode photoacoustic imaging of biological tissue.* Journal of biomedical optics, 2007. **12**(6): p. 060503-060503-3.

[26] Hu, S., K. Maslov and L.V. Wang, *Second-generation optical-resolution photoacoustic microscopy with improved sensitivity and speed.* Optics letters, 2011. **36**(7): p. 1134-1136.

[27] Wang, L., K. Maslov, J. Yao, et al., *Fast voice-coil scanning optical-resolution photoacoustic microscopy.* Optics letters, 2011. **36**(2): p. 139.

[28] Chen, Z., S. Yang and D. Xing, *In vivo detection of hemoglobin oxygen saturation and carboxyhemoglobin saturation with multiwavelength photoacoustic microscopy.* Optics letters, 2012. **37**(16): p. 3414-3416.

[29] Ning, B., N. Sun, R. Cao, et al., *Ultrasound-aided multi-parametric photoacoustic microscopy of the mouse brain.* Scientific reports, 2015. **5**: p. 18775.

[30] Rowland, K.J., J. Yao, L. Wang, et al., *Immediate alterations in intestinal oxygen saturation and blood flow after massive small bowel resection as measured by photoacoustic microscopy.* Journal of pediatric surgery, 2012. **47**(6): p. 1143-1149.

[31] Wang, X., G. Ku, M.A. Wegiel, et al., *Noninvasive photoacoustic angiography of animal brains in vivo with near-infrared light and an optical contrast agent.* Optics letters, 2004. **29**(7): p. 730-732.

[32] Song, K.H., E.W. Stein, J.A. Margenthaler, et al., *Noninvasive photoacoustic identification of sentinel lymph nodes containing methylene blue in vivo in a rat model.* Journal of biomedical optics, 2008. **13**(5): p. 054033-054033-6.

[33] Kim, C., E.C. Cho, J. Chen, et al., *In vivo molecular photoacoustic tomography of melanomas targeted by bioconjugated gold nanocages.* ACS nano, 2010. **4**(8): p. 4559-4564.

[34] De La Zerda, A., C. Zavaleta, S. Keren, et al., *Carbon nanotubes as photoacoustic molecular imaging agents in living mice.* Nature nanotechnology, 2008. **3**(9): p. 557-562.

[35] Li, K. and B. Liu, *Polymer-encapsulated organic nanoparticles for fluorescence and photoacoustic imaging.* Chemical Society Reviews, 2014. **43**(18): p. 6570-6597.

[36] 李长辉, 叶硕奇 and 任秋实, *光声分子影像 Photoacoustic Molecular Imaging.*

[37] Jokerst, J.V., A.J. Cole, D. Van de Sompel, et al., *Gold nanorods for ovarian cancer detection with photoacoustic imaging and resection guidance via Raman imaging in living mice.* ACS nano, 2012. **6**(11): p. 10366.

[38] Kircher, M.F., A. de la Zerda, J.V. Jokerst, et al., *A brain tumor molecular imaging strategy using a new triple-modality MRI-photoacoustic-Raman nanoparticle.* Nat Med, 2012. **18**(5): p. 829-834.

[39] Song, W., Q. Xu, Y. Zhang, et al., *Fully integrated reflection-mode photoacoustic, two-photon, and second harmonic generation microscopy in vivo.* Scientific Reports, 2016. **6**.

[40] Song, W., Q. Wei, L. Feng, et al., *Multimodal photoacoustic ophthalmoscopy in mouse.* Journal of biophotonics, 2013. **6**(6‐7): p. 505-512.

[41] Harrison, T., J.C. Ranasinghesagara, H. Lu, et al., *Combined photoacoustic and ultrasound biomicroscopy.* Optics express, 2009. **17**(24): p. 22041-22046.

[42] de La Zerda, A., Y.M. Paulus, R. Teed, et al., *Photoacoustic ocular imaging.* Optics letters, 2010. **35**(3): p. 270-272.

[43] Dai, X., L. Xi, C. Duan, et al., *Miniature probe integrating optical-resolution photoacoustic microscopy, optical coherence tomography, and ultrasound imaging: proof-of-concept.* Optics letters, 2015. **40**(12): p. 2921-2924.

[44] Hu, S., K. Maslov and L.V. Wang, *Noninvasive label-free imaging of microhemodynamics by optical-resolution photoacoustic microscopy.* Optics express, 2009. **17**(9): p. 7688-7693.

[45] Wang, X., Y. Pang, G. Ku, et al., *Noninvasive laser-induced photoacoustic tomography for structural and functional in vivo imaging of the brain.* Nature biotechnology, 2003. **21**(7): p. 803-806.

[46] Li, X., C. Heldermon, J. Marshall, et al. *Functional photoacoustic tomography of breast cancer: Pilot clinical results.* in *Biomedical Optics.* 2014. Optical Society of America.

[47] Menon, C. and D.L. Fraker, *Tumor oxygenation status as a prognostic marker.* Cancer Letters, 2005. **221**(2): p. 225-235.

[48] Tandara, A.A. and T.A. Mustoe, *Oxygen in Wound Healing—More than a Nutrient.* World Journal of Surgery, 2004. **28**(3): p. 294-300.

[49] Foo, S.S., D.F. Abbott, N. Lawrentschuk, et al., *Functional imaging of intratumoral hypoxia.* Molecular Imaging & Biology, 2004. **6**(5): p. 291-305.

[50] Wu, N., S. Ye, Q. Ren, et al., *High-resolution dual-modality photoacoustic ocular imaging.* Optics Letters, 2014. **39**(8): p. 2451-2454.

[51] Yao, J., C.-H. Huang, L. Wang, et al., *Wide-field fast-scanning photoacoustic microscopy based on a water-immersible MEMS scanning mirror.* Journal of biomedical optics, 2012. **17**(8): p. 0805051-0805053.

[52] Li, L., C. Yeh, S. Hu, et al. *Combined optical and mechanical scanning in optical-resolution photoacoustic microscopy.* 2014.

[53] Liu, T., Q. Wei, J. Wang, et al., *Combined photoacoustic microscopy and optical coherence tomography can measure metabolic rate of oxygen.* Biomedical optics express, 2011. **2**(5): p. 1359-1365.

[54] WHO, *Global data for visual impairment.* 2010.

[55] Gramatikov, B.I., *Modern technologies for retinal scanning and imaging: an introduction for the biomedical engineer.* Biomedical engineering online, 2014. **13**(1): p. 52.

[56] Silverman, R.H., *High‐resolution ultrasound imaging of the eye‐a review.* Clinical & experimental ophthalmology, 2009. **37**(1): p. 54-67.

[57] Jiao, S., M. Jiang, J. Hu, et al., *Photoacoustic ophthalmoscopy for in vivo retinal imaging.* Optics express, 2010. **18**(4): p. 3967.

[58] Silverman, R.H., F. Kong, H.O. Lloyd, et al. *Fine-resolution photoacoustic imaging of the eye.* in *BiOS.* 2010. International Society for Optics and Photonics.

[59] Institute, A.N.S., *American National Standard for Safe Use of Lasers*. 2007: Laser Institute of America.

[60] De Korte, C., A. Van Der Steen and J. Thijssen, *Acoustic velocity and attenuation of eye tissues at 20 MHz*. Ultrasound in medicine & biology, 1994. **20**(5): p. 471-480.

[61] Tang, J., *Ultrasonic Characterization of Corneal and Scleral Biomechanics*. 2012, The Ohio State University.

[62] Rao, B., S. Hu, L. Li, et al. *In vivo label-free photoacoustic microscopy of the anterior segment of the mouse eye*. in *BiOS*. 2010. International Society for Optics and Photonics.

[63] Hu, S. and L.V. Wang, *Photoacoustic imaging and characterization of the microvasculature*. Journal of biomedical optics, 2010. **15**(1): p. 011101-011101-15.

[64] Song, W., Q. Wei, T. Liu, et al., *Integrating photoacoustic ophthalmoscopy with scanning laser ophthalmoscopy, optical coherence tomography, and fluorescein angiography for a multimodal retinal imaging platform*. Journal of biomedical optics, 2012. **17**(6): p. 0612061-0612067.

[65] Liu, W., K.M. Schultz, K. Zhang, et al., *In vivo corneal neovascularization imaging by optical-resolution photoacoustic microscopy*. Photoacoustics, 2014. **2**(2): p. 81-86.

[66] Yao, J., L. Wang, J.-M. Yang, et al., *High-speed label-free functional photoacoustic microscopy of mouse brain in action*. Nature methods, 2015. **12**(5): p. 407-410.

[67] Lin, R., J. Chen, H. Wang, et al., *Longitudinal label-free optical-resolution photoacoustic microscopy of tumor angiogenesis in vivo*. Quantitative imaging in medicine and surgery, 2015. **5**(1): p. 23.

[68] Liu, X., T. Liu, R. Wen, et al., *Optical coherence photoacoustic microscopy for in vivo multimodal retinal imaging*. Optics letters, 2015. **40**(7): p. 1370-1373.

[69] Song, W., Q. Wei, W. Liu, et al., *A combined method to quantify the retinal metabolic rate of oxygen using photoacoustic ophthalmoscopy and optical coherence tomography*. Scientific reports, 2014. **4**: p. 6525.

[70] Hu, S., K. Maslov and L.V. Wang, *In vivo functional chronic imaging of a small animal model using optical-resolution photoacoustic microscopy*. Medical Physics, 2009. **36**(6): p. 2320-2323.

[71] Hu, S., J. Yao, K. Maslov, et al. *Optical-resolution photoacoustic microscopy of angiogenesis in a transgenic mouse model*. in *Proc. SPIE*. 2010.

[72] Yang, L.G., G. Randolph, J. Zou, et al. *Water-Immersible MEMS scanning mirror designed for wide-field fast-scanning photoacoustic microscopy*. in *Proc. of SPIE Vol*. 2013.

[73] Zhang, C., K. Maslov, S. Hu, et al., *Reflection-mode submicron-resolution in vivo photoacoustic microscopy*. Journal of Biomedical Optics, 2012. **17**(2): p. 0205011-0205014.

[74] Song, W., W. Liu and H.F. Zhang, *Laser-scanning Doppler photoacoustic microscopy based on temporal correlation*. Applied Physics Letters, 2013. **102**(20): p. -.

[75] Ning, W. and L. Changhui, *The impact of the detection angle on the quantitative measurement of hemoglobin oxygen saturation in optical-resolution photoacoustic microscopy*. Journal of Optics, 2016. **18**(10): p. 104002.

[76] Sivaramakrishnan, M., K. Maslov, H.F. Zhang, et al., *Limitations of quantitative photoacoustic measurements of blood oxygenation in small vessels*. Physics in medicine and biology, 2007. **52**(5): p. 1349.

[77] Laufer, J., D. Delpy, C. Elwell, et al., *Quantitative spatially resolved measurement of tissue chromophore concentrations using photoacoustic spectroscopy: application to the measurement of blood oxygenation and haemoglobin concentration*. Physics in medicine and biology, 2007. **52**(1): p. 141.

[78] Davis, J.A., D.E. McNamara, D.M. Cottrell, et al., *Image processing with the radial Hilbert transform: theory and experiments*. Optics Letters, 2000. **25**(2): p. 99-101.

[79] Yao, J., L. Wang, C. Li, et al., *Photoimprint Photoacoustic Microscopy for Three-Dimensional Label-Free Subdiffraction Imaging*. Physical Review Letters, 2014. **112**(1): p. 014302.

[80] Shashkov, E.V., M. Everts, E.I. Galanzha, et al., *Quantum dots as multimodal photoacoustic and photothermal contrast agents*. Nano letters, 2008. **8**(11): p. 3953-3958.

[81] Yang, X., S. Skrabalak, E. Stein, et al. *Photoacoustic tomography with novel optical contrast agents based on gold nanocages or nanoparticles containing near-infrared dyes*. in *Biomedical Optics (BiOS) 2008*. 2008. International Society for Optics and Photonics.

[82] Yang, X., E.W. Stein, S. Ashkenazi, et al., *Nanoparticles for photoacoustic imaging.* Wiley interdisciplinary reviews: nanomedicine and nanobiotechnology, 2009. **1**(4): p. 360-368.

[83] Qian, H., M. Zhu, Z. Wu, et al., *Quantum sized gold nanoclusters with atomic precision.* Accounts of chemical research, 2012. **45**(9): p. 1470-1479.

[84] Aikens, C.M., S. Li and G.C. Schatz, *From discrete electronic states to plasmons: TDDFT optical absorption properties of Ag n (n= 10, 20, 35, 56, 84, 120) tetrahedral clusters.* The Journal of Physical Chemistry C, 2008. **112**(30): p. 11272-11279.

[85] Richards, C.I., S. Choi, J.-C. Hsiang, et al., *Oligonucleotide-stabilized Ag nanocluster fluorophores.* Journal of the American Chemical Society, 2008. **130**(15): p. 5038-5039.

[86] Petty, J.T., J. Zheng, N.V. Hud, et al., *DNA-templated Ag nanocluster formation.* Journal of the American Chemical Society, 2004. **126**(16): p. 5207-5212.

[87] Petty, J.T., S.P. Story, J.-C. Hsiang, et al., *DNA-templated molecular silver fluorophores.* The journal of physical chemistry letters, 2013. **4**(7): p. 1148-1155.

[88] Lim, Y.T., S. Kim, A. Nakayama, et al., *Selection of quantum dot wavelengths for biomedical assays and imaging.* Molecular imaging, 2003. **2**(1): p. 15353500200302163.

[89] Shelton, R.L. and B.E. Applegate, *Ultrahigh resolution photoacoustic microscopy via transient absorption.* Biomedical optics express, 2010. **1**(2): p. 676-686.

[90] Danielli, A., C.P. Favazza, K. Maslov, et al., *Picosecond absorption relaxation measured with nanosecond laser photoacoustics.* Applied physics letters, 2010. **97**(16): p. 163701.

[91] Ashkenazi, S., S.-W. Huang, T. Horvath, et al., *Photoacoustic probing of fluorophore excited state lifetime with application to oxygen sensing.* Journal of biomedical optics, 2008. **13**(3): p. 034023-034023-4.

[92] Vasioukhin, V., C. Bauer, M. Yin, et al., *Directed actin polymerization is the driving force for epithelial cell–cell adhesion.* Cell, 2000. **100**(2): p. 209-219.

[93] Dustin, M.L. and D.R. Colman, *Neural and immunological synaptic relations.* Science, 2002. **298**(5594): p. 785-789.

[94] Dustin, M.L., *What counts in the immunological synapse?* Molecular cell, 2014. **54**(2): p. 255-262.

[95] Kaufman, E.N. and R.K. Jain, *Quantification of transport and binding parameters using fluorescence recovery after photobleaching. Potential for in vivo applications.* Biophysical journal, 1990. **58**(4): p. 873.

[96] Kang, M., C.A. Day, A.K. Kenworthy, et al., *Simplified equation to extract diffusion coefficients from confocal FRAP data.* Traffic, 2012. **13**(12): p. 1589-1600.

[97] Dijstelbloem, H.M., C.G. Kallenberg and J.G. van de Winkel, *Inflammation in autoimmunity: receptors for IgG revisited.* Trends in immunology, 2001. **22**(9): p. 510-516.

[98] Vardhana, S. and M. Dustin, *Supported planar bilayers for the formation of study of immunological synapses and kinapse.* Journal of visualized experiments: JoVE, 2008(19).

[99] Nguyen, T.T., K.L. Sly and J.C. Conboy, *Comparison of the energetics of avidin, streptavidin, neutrAvidin, and anti-biotin antibody binding to biotinylated lipid bilayer examined by second-harmonic generation.* Analytical chemistry, 2011. **84**(1): p. 201-208.

[100] Mingeot-Leclercq, M.-P., M. Deleu, R. Brasseur, et al., *Atomic force microscopy of supported lipid bilayers.* Nature protocols, 2008. **3**(10): p. 1654-1659.

[101] Bacia, K. and P. Schwille, *Practical guidelines for dual-color fluorescence cross-correlation spectroscopy.* Nature protocols, 2007. **2**(11): p. 2842-2856.

VITA

NING WU

Wu was born in Weinan city, Shaanxi province in China. She received her B.E. in Biomedical Engineering from College of Electronic Engineering of Xidian University in 2012. She then pursued her PhD. degree in Biomedical Engineering in the joint PhD. Program by Georgia Institute of Technology, Emory University, and Peking University under the supervision of Profs. Changhui Li and Cheng Zhu. Her research interests in the development of novel high-resolution photoacoustic/ultrasound systems, and clinical application for ocular diseases. During one year in Georgia Tech, she focused on the development of new photoacoustic contrast agent – DNA-templated silver nanocluster, and measuring 2D kinetics of ligand-receptor by fluorescence correlation spectroscopy.